Università degli Studi di Cagliari

Facoltà di Scienze MM. FF. NN.

Dipartimento di Scienze Chimiche e Geologiche

Dottorato di Ricerca in Science e Tecnologie Chimiche

XXIV Ciclo

SYNTHESIS, PHYSICAL PROPERTIES AND PROCESSING OF MULTIFUNCTIONAL MOLECULAR MATERIALS

Settore scientifico disciplinare

CHIM 03 / Chimica General ed Inorganica

PhD Thesis of:
Elisa Sessini

Supervisors	Coordinators
Prof. Maria Laura Mercuri	Prof. Mariano Casu
Prof. Eugenio Coronado	Prof. Anna Corrias

Esame finale anno accademico 2010 - 2011

ABSTRACT

New multifunctional materials (MMMs) where conductivity and magnetism coexist or, in some cases, interact, have been prepared and fully characterized as quality crystals or thin films. $[(BDH-TTP)_6]$ $[Fe(croc)_3]$ $\cdot CH_2Cl_2$ **(1)**, where paramagnetism is due to isolated Fe(III) metal ions with S = 5/2 ground state of the anionic $[Fe(croc)_3]^{3-}$ complexes and conductivity originates from BDH-TTP organic donor in k-type packing, has been obtained. When applying a pressure higher than 7 kbar, **(1)** behaves as a metal down to low temperature (2 K). The isostructural $[(BDH-TTP)_6]$ $[Ga(croc)_3]$ $\cdot CH_2Cl_2$ **(2)** behaves as a metal down to ~ 100 K. $[Mn(5-MeOsaltmen)(acetone)]_2[Ni(dmit)_2]_6$ **(3)**, where single molecule magnet (SMM) behavior of the Mn(III) dimers coexists with the semiconducting behavior due to the d^8 square planar complexes of $[Ni(dmit)_2]^{n-}$ (n = 0 or 1), has been obtained. Deviations of the magnetic properties from that of isolated $[Mn_2]^{2+}$ SMMs based, have been found, may be due to interactions such as $[Ni(dmit)_2]^{n-}$ ··· $[Ni(dmit)_2]^{n-}$, $[Mn_2]^{2+}$ ··· $[Mn_2]^{2+}$, $[Ni(dmit)_2]^{n-}$ ··· $[Mn_2]^{2+}$, demonstrating the tunability of the SMM behavior by changing the combination of both SMMs and conducting building blocks.

Processing of these materials has been performed by embedding different magnetic carriers into the poly(3,4-ethylenedioxythiophene) (PEDOT), conducting polymer. By potentiostatic and potentiodynamic electropolymerization, PEDOT films doped with magnetic polyoxometalate (POM) $[Co_4(H_2O)_2(PW_9O_{34})_2]^{10-}$ have been obtained; the film obtained by using the potentiodynamic method is more stable than the analogous material obtained by applying a constant potential, when subjected to potential cycles in acetonitrile solutions of $LiClO_4$ and $TBAClO_4$. *In situ* chemically oxidized PEDOT thin films, doped with $[Fe^{II}Cr^{III}(ox)_3]^-$ anions, have been obtained. These materials show ferromagnetic coupling due to Fe(II)-Cr(III) ions and the presence of some disorder and a superparamagnetic behavior, while the conductivity depends of the EDOT : anion ratio. The PEDOT:PSS (PSS = polystyrenesulfonic acid) aqueous dispersion, has been used for coating negatively charged, $Cs_{0.46}Ni[Fe(CN)_6]_{0.94}$, nanoparticles (NPs) and a high conducting thin film showing superparamagnetic properties due to the NPs has been obtained. Magnetoresistance measurements at low temperature reveal the existence of an interplay between the magnetic and conducting lattices.

TABLE OF CONTENTS

I: MAGNETIC MOLECULAR CONDUCTORS

Chapter 3 MULTIFUNCTIONAL MATERIAL BASED ON SINGLE MOLECULE MAGNET (MN-SALEN TYPE) AND NI-DITHIOLENE COMPLEXES

II: PROCESSING OF MULTIFUNCTIONAL MATERIALS

Chapter 4 CONDUCTING POLYMERS (PEDOT)

Chapter 5 PEDOT THIN FILMS DOPED WITH POLYOXOMETALATE (POM) ANION [Co$_4$(H$_2$O)$_2$(PW$_9$O$_{34}$)$_2$]$^{10-}$ ANIONS

Chapter 6 PEDOT THIN FILMS DOPED WITH MAGNETIC NANOSTRUCTURES
           ([FE^{II}CR^{III}(OX)$_3$]$^-$ ANIONS)

ACN CH_3CN acetonitrile

BDH-TTP 2,5-bis(1,3-dithiolan-2-ylidene)-1,3,4,6-tetrathiapentalene

BEDT-TTF bis(ethylenedithio)tetrathiafulvalene

croc croconate $(C_5O_5)^{2-}$ **(**4,5-dihydroxycyclopent-4-ene-1,2,3-trione)

COPs Conducting Organic Polymers

DMSO Dimethyl sulfoxide

DLS Dynamic Light Scattering

EDOT 3,4-ethylenedioxythiophene

EDX Energy-dispersive X-rays

EQCM Electrochemical Quartz Crystal Microbalance

ESR Electron Spin Resonance

ET see BEDT-TTF

HR-TEM High Resolution Transmission Electron Microscopy

IR infrared spectroscopy

MMMs Multifunctional Molecular Materials

nButOH $CH_3(CH_2)_3OH$ normal butanol

NPs nanoparticles

PEDOT poly(3,4-ethylenedioxythiophene)

PhCN benzonitrile

PSS polystyrenesulfonic acid

PPy polypyrrole

r.t. room temperature

σ conductivity (S/cm)

ρ resistivity (Ω)

S/cm Siemens/centimeter

SEM Scanning Electron Microscopy

TBABr $[(C_4H_9)_4N]Br$ tetra-*n*-butylammonium bromide

TCE 1,1,2 – trichloroethane

TTF tetrathiafulvalene

UV-Vis Ultra Violet – Visible

VRH variable-range hopping

XRD X-ray diffraction

CHAPTER 1

Introduction

1.1 MULTIFUNCTIONAL MATERIALS

As the physical limits of conventional silicon-based electronics are approached, the search for new types of materials that can deliver smaller devices grows up. Molecular electronics that uses assemblies of individual molecules to reproduce conventional structures such as switches or semiconductors represents the new frontier. In this context molecule-based materials, namely materials built from pre-designed molecular building blocks, play a key role since they are known to exhibit many technologically important properties (e.g., magnetic ordering, conductivity, superconductivity…) traditionally considered to be solely available for classic atom-based inorganic solids such as metals, alloys or oxides. Their relevance in Material Science is mainly due to the tunability of their physical properties by conventional synthetic methods; molecular materials in fact are obtained through soft routes, traditionally from organic chemistry, coordination chemistry and supramolecular chemistry and this opens unprecedented possibilities to the design of molecules with the desired size, shape, charge, polarity, and electronic properties, in response to the changing demands of technology. The area of molecular materials with interesting technological properties started almost 75 years ago with the discovery of the first complexes showing spin crossover transitions [Fe(S$_2$NCR$_2$)$_3$]. [1] Since then molecular materials have given rise to complexes with spin crossover transitions, [2] semiconductors, metals and superconductors, [3] ferrimagnets, ferromagnets and weak ferromagnets, [4] chromophores [5] including those for non linear optics (NLO) and Vis.-NIR emitters based on lanthanide complexes with polyconjugated ligands. [6] Because of their versatility and their peculiar optical, magnetic and conducting properties, molecule-based materials are appealing candidates for practical applications in post-silicon molecular electronics and spintronics (a new paradigm of electronics based on the spin degree of freedom of the electron). [7] In fact, their technological applications in electronic, magnetic and photonic devices range from data storage to telecommunication/information technology

(switches, sensors, ….) [8]

In addition to mono-functional materials a more recent and appealing goal in the field of molecule-based materials is the search for multifunctionality in these systems: the proper selection of the molecular building blocks yield to the combination (or even the interplay) in the same crystal lattice of two or more physical properties such as magnetism and conductivity or optical properties, which are difficult or impossible to achieve in conventional inorganic solids. In this aspect the possibilities offered by the molecular bottom-up approach are unprecedented and many interesting and challenging combinations of physical properties can be envisaged. The complexity of these materials make the design of the molecular building blocks, the control of the intermolecular interactions and the crystallization techniques crucial for obtaining functional materials exhibiting technologically useful physical properties. These materials offer the intriguing opportunity to modulate one (or more) physical property by tuning the other one.

Particularly, three main classes of multifunctional materials can be identified: i) optically active magnets, [9] [10] ii) optically active conductors, [11] [12] iii) magnetic conductors. [13]

In this work, systems showing conducting and magnetic properties are investigated as crystals or processed as magnetic carriers into conducting polymers. Particular attention has been given to the investigation of the interactions between magnetism and conductivity in systems where the two networks are not electronically independent.

1.2. MAGNETIC MOLECULAR CONDUCTORS

From a physical point of view molecular materials that combine two networks, each one furnishing conducting (delocalized π-electrons) and magnetic (localized d electrons) properties, have attracted major interest since they can exhibit a coexistence or novel and improved properties with respect to those of the two networks, due to the interactions established between them. The development of these π-d multifunctional materials represents one of the main targets in current Materials Science for their potential applications for future molecular electronics. [14]

The first reported example of organic molecular metal, showing a metallic state down to 55 K, is [TTF] [TCNQ] [15] (TTF = tetrathiafulvalene; TCNQ = 7,7,8,8-tetracyano-*p*-quinodimethane). (Figure 1.1)

This compound can be classified as charge transfer salt with a general formula:

$$m\text{D}^0 + n\text{A}^0 \rightarrow \text{D}_m^{\rho+} \text{A}_n^{\rho-}$$
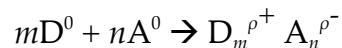
where D (TTF) is the donor and A (TCNQ) is the acceptor of electrons. ρ is the charge transfer ratio that can assume values in the range $0 < \rho < 1$.

This charge-transfer salt consists of segregated stacks of partially charged, aromatic organic donor and acceptor molecules along which π electrons move giving rise to conductivity (Figure i.1). Moreover, the planarity of the TTF moiety allows efficient close packing, maximizing $\pi - \pi$ orbital overlap between adjacent molecules that interact each other also through S $\cdots$ S contacts between the four polarizable S atoms.

TTF   **TCNQ**
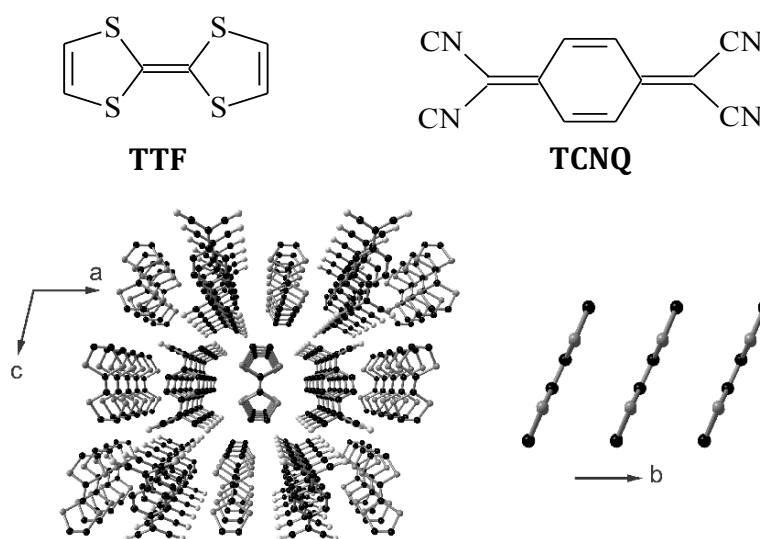
Figure 1.1: TTF and TCNQ molecules (up) and the segregated stacks of charge-transfer salt based on them (down).

A large number of molecular conductors and superconductors have also been synthesized in which the radical ion of the organic donor or acceptor (resulting from oxidation or reduction processes, respectively) co-crystallizes with an inorganic counterion. To incorporate localized magnetic moments into the material, a breakthrough strategy is to use a magnetic ion as charge-compensating counterion. Numerous inorganic complexes are suitable for this purpose ranging from simple mononuclear complexes $[\text{MX}_4]^{n-}$ (M = Fe$^{\text{III}}$, Cu$^{\text{II}}$; X

= Cl, Br) and $[M(ox)_3]^{3-}$ (ox = oxalate = $C_2O_4^{2-}$) with tetrahedral and octahedral geometry respectively, to cluster complexes as polyoxometalates to layered structures such as bimetallic oxalato complexes $[M^{II}M^{III}(ox)_3]^-$ (M^{II} = Mn, Co, Ni, Fe, Cu; M^{III} = Fe, Cr). (Figure 1.2) [13]
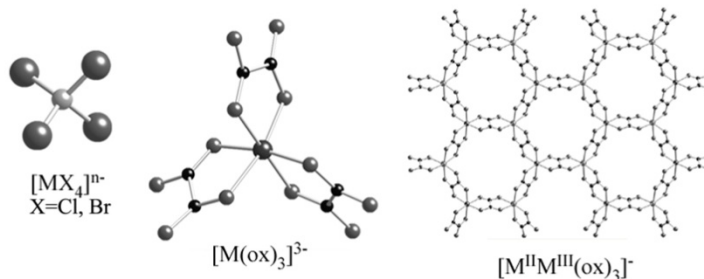
Figure 1.2: scheme of the principal magnetic carriers used as building blocks of organic/inorganic magnetic molecular conductors

Geometry, shape, size and nature of the acceptor influence the packing arrangement and then the conductivity of the material. In fact, it has been observed that square-planar complexes such as d^8 metal dithiolenes favor a "face-to-face" packing of alternate stacks [D-A-D-A-D-A…], generally leading to a semiconducting or insulating state, while tris-chelated metal complexes with octahedral geometry lead to donors and acceptors organization as segregated stacks [D-D-D-D…][A-A-A-A…], favoring the metallic state. For this reason octahedral metal complexes are the most successful counterions for obtaining the metallic behavior. In addition Λ and Δ chirality may also play a role in the packing of molecular materials, inducing a specific assembly order of donor molecules and likely leading to improve conducting properties.

1.2.1 Multifunctional Molecular Materials based on TTF-derivatives

Since the discovery of [TTF][TCNQ] conductivity, extensive efforts have been devoted to prepare new types of molecular metals or superconductors based on the TTF moiety. In fact, it is possible to finely tune the electronic properties of the material thanks to a rational design of the molecular component. In order to increase the conductivity, some strategies related to molecule engineering, have been proposed: extension of π-conjugation for increasing charge delocalization and decreasing the on-site coulombic repulsion; introduction of highly polarizable atoms as S or Se for increasing orbital overlap, intermolecular

interactions and system dimensionality.

For example, $(TMTSF)_2PF_6$ (TMTSF = tetramethyltetraselenofulvalene, [16] is a superconductor in which a 2-D network is formed by short Se···Se contacts between the TMTSF stacks. Some examples of TTF-based building blocks for molecular conductors are reported in Figure 1.3.

$R^1 = R^2 = H, X = S; TTF$
$R^1 = R^2 = Me, X = Se; TMTSF$
$R^1 = H, R^2 = -S(CH_2)_2S-, X = S; EDT-TTF$

X = S; BEDT-TTF (ET)
X = Se; BETS
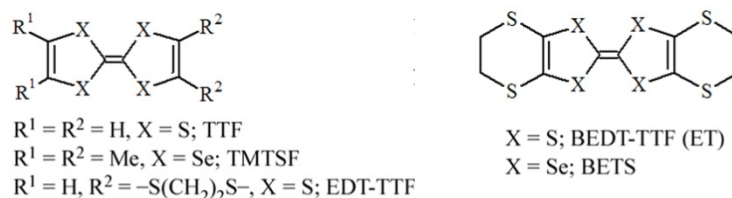
Figure 1.3: some examples of TTF-derivatives.

Among the large number of TTF-derivatives, a special place is reserved to bis(ethylenedithio)tetrathiafulvalene (BEDT-TTF or ET), which has produced the majority of organic metals and superconductors reported in literature.

Different spatial arrangements of BEDT-TTF molecules are reported and each of them leads to different electronic properties. (Figure 1.4) [17] Among them, the κ-type, in which interacting dimers of the donors are approximately orthogonal each other, forming a conductive two-dimensional network due to S ··· S interactions, is particularly interesting. This arrangement has been found in many superconducting molecular materials and, in particular, is found in κ-[BEDT-TTF]$_2$[CuN(CN)$_2$Br], showing the highest transition temperature (T_C = 11.6 K) from metallic to superconducting state that has been reported so far. [18]
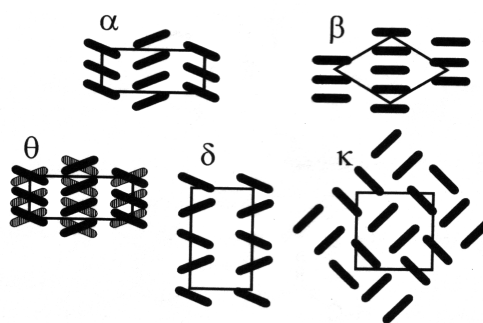
Figure 1.4: scheme of the most common packing phases of TTF and TTF derivatives.

Important milestones in the area of molecular magnetic conductors showing a combination of properties are based on BEDT-TTF or its selenium derivatives

with charge-compensating anions furnishing the magnetic properties, and among them, three can be recognized as the most significant.

The first one is the antiferromagnetic/superconductor κ-(BETS)$_2$[FeX$_4$] (X = Br, Cl) [19] (BETS = bis(ethylenedithio)tetraselenafulvalene), in which the magnetism is due to the zero-dimensional [FeX$_4$]$^-$ anion and the superconductivity originates from the segregated stacks of BETS molecules. By replacing the tetrahalometalato anion with tri-oxalato metal complexes, the first paramagnetic/superconductor (BEDT-TTF)$_4$[H$_3$OM(III)(C$_2$O$_4$)$_3$](PhX) (M(III) = Cr, Fe, Ga; X = CN, NO$_2$, F, Br, …) [20] has been obtained. A rational strategy to introduce ferromagnetism in the material is to use, as inorganic anion, an extended magnetic layer, such as bimetallic oxalato complexes (M^{II} = Mn, Co, Ni, Fe, Cu; M^{III} = Fe, Cr). Following this strategy the ferromagnetic/metal, (BEDT-TTF)$_3$[MnCr(ox)$_3$], the most significant advance in this field has been synthesized. [21] In this material, bimetallic layer anions behave as ferro- or ferrimagnets with T$_c$'s in the range 5.5 – 43 K.

All of these examples point out the crucial role of intermolecular interactions such as van der Waals contacts (S$\cdots$S, S$\cdots$Se, shorter than the Wan der Waals radii), π-π and π-d interactions, H-bonding *etc.* in the self-assembly of pre-designed molecular units. These interactions may provide a powerful way to afford layered mono/multifunctional molecular materials with new or unknown physical properties.

1.2.2 Multifunctional Molecular Materials based on dithiolene complexes

Although many molecular superconductors are formed by TTF-based organic π donor molecules, a unique position is occupied by the [M(dmit)$_2$]-based (M = Ni, Pd; dmit = 1,3-dithiole-2-thione-4,5-dithiolate) superconductors. (Figure 1.5) Metal dithiolene complexes have proved to be useful building blocks for multifunctional molecular materials (MMMs) since these complexes can be viewed as the inorganic analogues of TTF-type donors where the transition metal replaces the central C=C bond of TTF. The first synthesized molecular superconductors containing a metal–dithiolene complex are (TTF)[Ni(dmit)$_2$]$_2$ [22] (*T*c = 1.6 K at *P* = 7 kbar) and the α-(EDTTTF)[Ni(dmit)$_2$] (EDTTTF = ethylenedithiotetrathiafulvalene) [23] M(dmit)$_2$ (M = Ni, Pd) (*T*c = 1.3 K at ambient pressure).
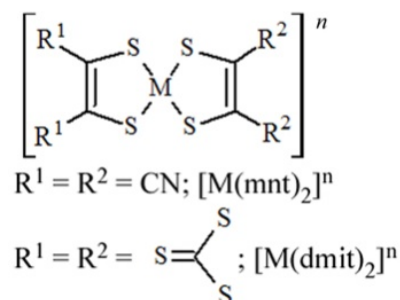
Figure 1.5: scheme of the principal dithiolene metal complexes used as building blocks of MMMs

With respect to TTF, bis(dithiolene)-based systems are more versatile since in some cases, depending on the nature of the metal, they can exhibit peculiar magnetic properties. Although in terms of molecular architecture, the $[M(dmit)_2]$ molecule, where the central electron-delocalized core is extended by the sulphur-containing heterocycles, is similar to the BEDT-TTF donor, the transverse interactions have been found to be weaker than expected and unable to realize a 2-D network. Therefore the superconductivity is stabilized only at very low temperatures. In fact, dithiolene complexes have shown insulating instability at low temperature due to MI transition caused by Peierls-type (see Appendix C) dimerization along the chains [24] (these compounds usually crystallize forming stacks of complexes that give rise to quasi-1-D, electronic systems) preventing the occurrence of either the metallic state or superconductivity. [25][26] The Peierls distortion may be suppressed by increasing the dimensionality of the systems through lateral interactions. This can be obtained either increasing the number of peripheral S atoms in the ligand framework, or changing from sulphur to selenium analogues.

Despite the Peierls distortion limitation, metal–dithiolene complexes can provide unique examples of novel low dimensional materials exhibiting interesting conducting and/or magnetic properties. Important milestones are: (i) two bulk ferromagnetic complexes: $(NH_4)[Ni(mnt)_2] \cdot H_2O$ [27] (mnt = maleonitriledithiolate), showing antiferromagnetic ordering at $T > 100$ K, ferromagnetic coupling below this temperature and ferromagnetic ordering at $T < 5$ K and $[Cp_2^*Mn][Ni(mnt)_2]$ [28] (Cp = cyclopentadienyl), a semiconductor with ferromagnetic ordering at $T < 2.5$ K; (ii) $(per)_2[M(mnt)_2]$ (M = Fe, Co, Ni, Pd, Pt, Cu, Au; per = perylene, family [29], the first examples of paramagnetic

molecular metals.

Recently, Yamashita and coworkers have addressed their interest to dithiolene metal complexes. In fact, a unique hybrid material based on Mn_4 single-molecule magnet (SMM) clusters in the $S_T = 9$ spin state and $[Pt(mnt)_2]^{z-}$ dithiolene complexes, $[\{(Mn^{II}_2Mn^{III}_2(hmp)_6(CH_3CN)_2\}\{Pt(mnt)_2\}_4][Pt(mnt)_2]_2$ [30] (hmp = (2-pyridyl)methanolate) (see Figure i.6), showing SMM/semiconducting behavior has been reported. In this material, the inter-SMMs interaction via conducting electrons, albeit small, has a mutual influence on both SMM properties and conductivity. [31] This class of SMMs offers the intermolecular interactions by a rational design of the ligands that chelate the quasi double-cuboidal $[Mn_4]$ core.

Other MMMs, reported in literature, have been synthesized following the same strategy [32]
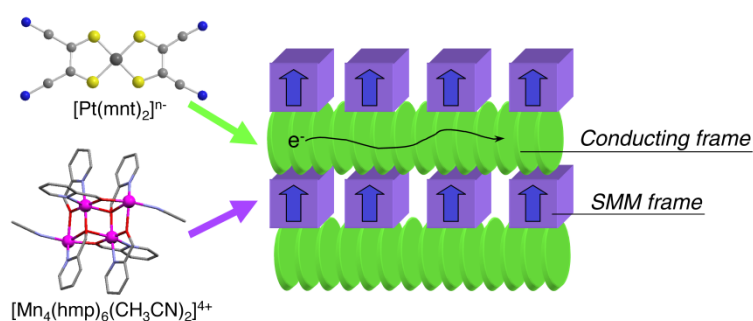
Figure 1.6: scheme of MMM based on SMM as and dithiolene platinum complexes as magnetism and conductivity carriers, respectively

1.3 MULTIFUNCTIONAL MATERIALS BASED ON CONDUCTING ORGANIC POLYMERS

In the field of Molecular Science, recent efforts have been addressed to the technological applications of multifunctional molecular materials (MMMs). In this context, processing plays a crucial role. The common processing techniques require the precursors in gas or solution phases. The most commonly used gas phase techniques are the chemical vapor deposition (CVD) and the thermal sublimation in high vacuum and for applying these techniques, the precursors should satisfy some requirements such as high volatility, easy transport in gas phase and thermal stability. Instead, for techniques that involve solution processes different criteria as solubility, stability in aqueous or non – aqueous

solutions are to be met by material precursors. However, solution methods are in general more versatile and low-cost. Langmuir – Blodgett (LB) and sol-gel are examples of the latter class. In this context, polymers offer the intriguing opportunity of a low-cost processing along with flexibility, transparency, … and of the appealing properties of obtained thin films. [33] In particular, organic conducting polymers (COPs) can be easily processed as thin films by casting from solution, since they are soluble in common solvents as water or alcohols. COPs. Some examples of COPs, reported in Figure 1.7, have found several applications in electronic devices, such as, for example, in Light Emitting Diodes (LEDs). [35]- [37]
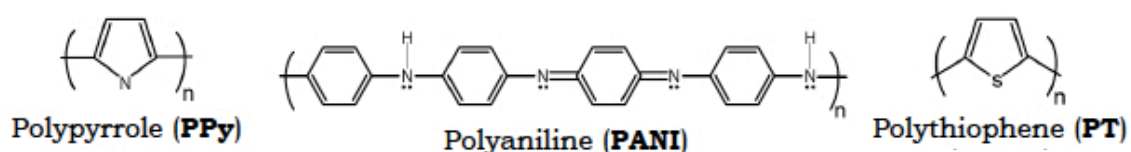
Figure 1.7: some example of (semi)transparent COPs

Moreover, they have the added value of being able to conduct electricity. [34] In order to conduct electricity, polymers must satisfy two requirements: 1) they must possess conjugated double bonds in which π electrons are relatively delocalized; 2) electrons have to be removed from (oxidation) or inserted into (reduction) the polymer by a dopant. As the dopant carries an additional physical property such as, for example, magnetism, the obtained material will show multifunctionality. (See Chapter 4) Multifunctional materials based on COPs doped with polyoxometalate (POMs) clusters [38] or nanostructures [39] are the main examples reported in the literature. Research on processed materials based on COPs has been for long hampered by difficulties in investigating their physical properties due to sample inhomogeneity arising from formation of defects that break structural or physical property coherence. However, advances in characterization techniques have recently allowed the development of these materials, even though more work is needed to improve the quality of the deposited films.

1.4 AIM OF THE WORK

The synthesis, characterization and study of the physical properties of new multifunctional materials are reported. In the present work, particular attention is addressed to the design and the selection of the building blocks, on the basis of the excellent results already obtained and reported in literature.

A strategy for investigating the structure/property relationship in molecular charge – transfer salts is to compare isostructural series. [13] Following this strategy, this work has been addressed to:

- the synthesis and characterization of MMMs based on 2,5-bis(1,3-dithiolan-2-ylidene)-1,3,4,6-tetrathiapentalene (BDH-TTP), an organic donor isostructural of bis(ethylenedithio)tetrathiafulvalene (BEDT-TTF), with the chiral anion $[M^{III}(croc)_3]^{3-}$ ($croc^{2-}$ = $C_5O_5^{2-}$ = dianion of 4,5-dihydroxycyclopent-4-ene-1,2,3-trione; M = Fe, Ga);

- the synthesis and characterization of MMMs based on $[Mn^{III}$ (5-MeOsaltmen)$(H_2O)]_2]^{2+}$ (5- MeOsaltmen^{2-} = N,N0-(1,1,2,2-tetramethylethylene)bis(5-methoxysalicylideneiminate)) showing Single Molecule Magnet (SMM) behavior and $[Ni(dmit)_2]^-$ ($dmit^{2-}$ = 2-thioxo-1,3-dithiole-4,5-dithiolate) as conductivity carrier;

- the processing as thin films of some interesting magnetic carriers as polyoxometallates (POMs) and nanostructures into [poly(3,4-ethylenedioxythiophene)] (PEDOT) as conducting polymer by using different methods as electrochemical or chemical polymerization;

For all the obtained materials, the study of the physical properties is addressed to investigate the coexistence or even the interplay of magnetism and conductivity.

REFERENCES

[1] Cambi, L. and Gagnasso, A. (**1931**) *Atti. Accad. Naz. Lincei,* **13**, pp. 809-.

[2] Gütlich, P., Ksenofontov, V. and Gaspar, A. B. , *Coord. Chem. Rev.*, **2005**, (249), 1811-1829.

[3] Williams, J. M. Ferraro, J. R Thorn, R. J. Carlson, K. D. Geiser, U. Wang, H. H. Kini, A. M. and Whangbo M. H. (**1992**). *Organic Superconductors*, Englewood Cliffs: Prentice Hall.

[4] Miller, J. S. and Drillon, M. (**2004**) *Magnetism: Molecules to Materials*, (Wiley-VCH, Weinheim) vol. 1-4.

[5] Prasad, P. N. and Williams, D. J. (**1991**) Introduction of Nonlinear Optical Effects in Molecules and Polymers, (J. Willey and Sons, New York); Chemla, D. S. and Zyss, J. (1987) Nonlinear Optical Properties of Organic Molecules and Crystals (Academic Press, New York) vol. 1, 2.

[6] (a) Curry, R. J. and Gillin, W. P., *Appl. Phys. Lett.*, **1999,** (75), 1380-1382; (b) Gillin, W. P. and Curry, R. J., 798-799; (b) Mitscke, U. and Bauerle, P., *J. Mater. Chem.*, **2000**, (10), 1471-1507; (c) Kelley, T. W., Baude, P.F., Gerlach, C., Ender, D. E., Muyres, D., Haase, M. A., Vogel, D. E. and Theiss, S. D., *Chem. Mater.*, **2004**, (16), 4413-4422.

[7] Wolf, S. A., Awschalom, D. D., Burham, R. A., Daughton, J. M., von Molnár, S., Roukes, M. L., Chtchelkanova, A. Y. and Treger, D. M, *Science*, . **2001** (294), 1488-1495 and references therein.

[8] Fraxedas, J.**,** *Adv. Mater.*, **2002**, (14), 1603-1614 and references therein.

[9] (a) Mito, M.; Iriguchi, K.; Deguchi, H.; Kishine, J., Kikuchi, K.; Ohsumi, H.; Yoshida, Y., Inoue, K. *Phys. ReV. B* **2009**, *79*, 012406. (b) Train, C.; Gheorghe, R.; Krstic, V.; Chamoreau, L. M.; Ovanesyan, N. S.; Rikken, G. L. J. A.; Gruselle, M.; Verdaguer, M. *Nat. Mater.* **2008**, *7*, 729

[10] M. Gruselle, C. Train, K. Boubekeur, P. Gredin, N. Ovanesyan, *coord. Chem. Rev.*, **2006**, (250) 2491

[11] Avarvari, N.; Wallis, J. D., *J. Mater. Chem.* **2009**, *19*, 4061

[12] E.Coronado, J.R. Galán-Mascarós, *J. Mater. Chem.*, **2005**, (15), 66

[13] E.Coronado, P. Day, *Chem. Rev.*, **2004**, (104), 5419

[14] "Multifuctional Materials of interest in Molecular Electronics", M. L. Mercuri, P. Deplano, A. Serpe, F. Artizzu, Chapter in *Handbook of Multifunctional Molecular Materials*, Pan Stanford Publishing, eds Lahcène Ouahab **2011**

[15] J. P. Ferraris, D. O. Cowan, V. Jr. Walatka and J. H. Perlstein, *J. Am. Chem. Soc.*, **1973** (95), 948

[16] D. Jérome, M. Mazaud, M. Ribault and K. Bechgaard, *J. Phys. Lett.*, **1980 (**41), L95

[17] (a) T. Mori, *Bull. Chem. Soc. Jpn.*, 71, **1998**, 2509-2526; (b) H. Seo, C. Hotta, H. Fukuyama, *Chem. Rev.,* **2004**, *104* (11), 5005–5036; (c) K. Miyagawa, A. Kawamoto and K. Kanoda, *Chem. Rev.*, **2004**, (104), 5635-5653

[18] A. M. Kini, U. Geiser, H. H. Wang, K. D. Carlson, J. M. Williams, W. K. Kwok, K. G. Vandervoort, J. E. Thompson, D. L. Stupka, D. Jung, M.-H. Whangbo, *Inorg. Chem.* **1990,** (29)**,** 2555-2557

[19] (a) E. Coronado, S. Curreli, C. Giménez-Saiz and C. J. Gómez-García, *J. Mater. Chem.,* **2005**, (15), 1429; (b) S. Uji, H. Shinagawa, T. Terashima, T. Yakabe, Y. Terai, M. Tokumoto, A. Kobayashi, H. Tanaka and H. Kobayashi, *Nature,* **2001**, (410), 908

[20] (a) H. Kobayashi, H. B. Cui, A. Kobayashi, *Chem. Rev.,* **2004**, (104), 5265 (b) M. Kurmoo, A. W. Graham, P. Day, S. J. Coles, M. B. Hursthouse, J. L. Caulfield, J. Singleton, F. L. Pratt, W. Hayes, L. Ducasse and P. Guionneau, *J. Am. Chem. Soc.,* **1995**, (117), 12209; (c) L. Martin, S. S. Turner, P. Day, F. E. Mabbs and E. J. L. McInnes, *J. Chem. Soc., Chem. Commun.,* **1997**, 1367; (d) S. Rashid, S. S. Turner, P. Day, J. A. K. Howard, P. Guionneau, E. J. L. McInnes, F. E. Mabbs, R. J. H. Clark, S. Firth, T. Biggs, *J. Mater. Chem.,* **2001**, (11), 2095

[21] E. Coronado, J. R. Galán-Mascarós, C. J. Gómez-García, V. N. Laukhin, *Nature,* **2000**, (408), 447

[22] L. Brossard, M. Ribault, M. Bousseau, L. Valade and P. Cassoux, *C. R. Acad. Sci., Ser. II*, **1986**, (302), 205

[23] H. Tajima, M. Inokuchi, A. Kobayashi, T. Ohta, R. Kato, H. Kobayashi and H. Kuroda, *Chem. Lett.*, **1993**,1235

[24] R. E. Peierls, *Quantum Theory of Solids*, Oxford Universiry Press, Oxford, **1955**, p. 108.

[25] (a) H. Kobayashi, H. Tomita, T. Naito, A. Kobayashi, F. Sakai, T. Watanabe and P. Cassoux, *J. Am. Chem. Soc.*, **1996**, (118), 368; (b) T. Courcet, I. Malfant, K. Pokhodnia and P. Cassoux, *New J. Chem.*, **1998**, 585; (c) H. Fujiwara, E. Ojima, H. Kobayashi, T. Courcet, I. Malfant and P. Cassoux, *Eur. J. Inorg. Chem.*, **1998**, 1631

[26] N. J. Harris and A. E. Underhill, *J. Chem. Soc., Dalton Trans.*, **1987**, 1683

[27] A. T. Coomber, D. Beljonne, R. H. Friend, J. L. Brédas, A. Charlton, N. Robertson, A. E. Underhill, M. Kurmoo and P. Day, *Nature*, **1996**, (**380**), 144

[28] C. Faulmann, E. Rivière, S. Dorbes, F. Senoca, E. Coronado and P. Cassoux, *Eur. J. Inorg. Chem.*, **2003**, 2880

[29] (a) R. T. Henriques, L. Alcácer, in *Inorganic and Organometallic Polymers with special properties* (Ed. R. Laine), **1992**, Kluwer Academic Publishers, Boston, pp. 163-177; (b) V. Gama, R. T. Henriques, G. Bonfait, L. C. Pereira, J. C.

Waerenborgh, I. C. Santos, M. T. Duarte, J. M. P. Cabral and M. Almeida, *Inorg. Chem.,* **1993**, (31), 2598; (c) V. Gama, R. T. Henriques, M. Almeida and L. Alcácer, *J. Phys. Chem.,* **1994**, (98), 997

[30] H. Hiraga, H. Miyasaka, K. Nakata, T. Kajiwara, S. Takaishi, Y. Oshima, H. Nojiri and M. Yamashita, *Inorg. Chem.,* **2007**, (46), 9661

[31] (a) H. Miyasaka, K. Nakata, L. Lecren, C. Coulon, Y. Nakazawa, T. Fujisaki, K. Sugiura, M. Yamashita and R. Clérac, *J. Am. Chem. Soc.,* **2006**, (128), 3770; (b) H. Miyasaka, K. Nakata, K. Sugiura, M. Yamashita and R. Clérac, *Angew. Chem. Int. Ed.,* **2004**, (43), 707

[32] (a) K. Kubo, T. Shiga, T. Yamamoto, A. Tajima, T. Moriwaki, Y. Ikemoto, M. Yamashita, E. Sessini, M. L. Mercuri, P. Deplano, Y. Nakazawa, R. Kato, *Inorganic Chemistry*, **2011**, 50 (19), 9337-9344 (b) H. Hiraga, H. Miyasaka, S. Takaishi, T. Kajiwara, M. Yamashita, *Inorg. Chim. Acta*, **2008**, (361), 3863-3872; (c) H. Hiraga, H. Miyasaka, R. Clérac, M. Fourmigué, M. Yamashita, *Inorg. Chem.,* **2009**, (48), 2887-2898

[33] A. MacDiarmid, *Angew. Chem. Int. Ed.,* **2001**, (40), 2581-2590

[34] A. J. Heeger, *Angew. Chem. Int. Ed.,* **2001**, (40), 2591-2611

[35] (a) Y. Cao, G. M. Treacy, P. Smith, A. J. Heeger, *Appl. Phys. Lett.* **1992**, (60), 2711; (b) G. Gustafsson, Y. Cao, G. M. Treacy, F. Klavetter, N. Colaneri A. J. Heeger, *Nature,* **1992**, (357), 477

[36] J. Gao, A. J. Heeger, J. Y. Lee, C. Y. Kim, Synth. Met. **1996**, (82), 221;

[37] Y. Cao, G. Yu, C. Zhang, R. Menon, A. J. Heeger, *Synth. Met.* **1997**, (87), 171

[38,] (a) P. Gómez-Romero, *Adv. Mater.,* **2001**, (13), 163-174 and references therein (b), J. Vaillant, M. Lira-Cantu, K. Cuentas-Gallegos, N. Casañ-Pastor, P. Gómez-Romero, *Progress in Solid State Chemistry*, **2006**, (34), 147-159

[39] (a) D. C. Sun, D. S. Sun, *Materials Chemistry and Physics*, **2009**, (118), 288–292; (b) V.C. Ferreiraa, A.I. Melato, A.F. Silva, L.M. Abrantes, *Electrochimica Acta*, **2011**, (56), 3567–3574; (c) P.V. Kamat, *J. Phys. Chem,. B*, **2002**, (106) 7729; (d) M.Wan, *Conducting Polymers with Micro or Nanometer Structure*, **2008**, Springer and references therein

I

Multifunctional Molecular Materials

CHAPTER 2[*]

Multifunctional Materials based on paramagnetic complexes of $M^{III}(croc)_3^{3-}$ (M = Fe, Ga)

2.1 INTRODUCTION

As widely described previously (see Introduction), multifunctional molecular materials (MMMs) have recently excited chemists, physicists and engineers because of their peculiar properties and potentially profitable technological applications. [1]

These materials consist of two different molecular networks, each one furnishing a distinct physical property such as magnetism and conductivity, which can coexist or even be in interplay in the same crystal lattice. [2]

Particularly, materials showing conducting and magnetic properties are discussed in this work. The most significant advances in this field are the milestones listed below:

- paramagnetic/superconductor $(BEDT-TTF)_4[H_3OM^{III}(ox)_3] \cdot S$ (BEDT-TTF = bis(ethylenedithio)tetrathiafulvalene; M^{III} = Cr, Fe and Ga; ox = dianion of oxalato = $C_2O_4^{2-}$; S = C_6H_5CN, $C_6H_5NO_2$, PhF, PhBr, etc.); [3] [4]

- antiferromagnetic/superconductor κ-$(BETS)_2[FeBr_4]$ (BETS = bis(ethylenedithio)tetraselenafulvalene); [4] [5]

- ferromagnetic/metal, $(BEDT-TTF)_3[MnCr(ox)_3]$; [4] [6]

As clearly demonstrated by Day et al. [7] [8] [9], small changes in the crystalline structure of these salts, could lead to a material showing different physical properties. For this reason, great attention has been given in the past to a well-thought-out design of the material building blocks. On the basis of the obtained results, efforts have been made by several research groups to synthesize new materials with improved properties by changing the conductivity and/or the magnetism carriers. In this chapter, the synthesis and characterization of two new hybrid materials based on $M^{III}(croc)_3^{3-}$ ($croc^{2-}$ = $C_5O_5^{2-}$ = dianion of 4,5-

---

[*] This work has been carried out at the Department of Chemistry, Tohoku University during my research stay in Sendai (Japan)

dihydroxycyclopent-4-ene-1,2,3-trione; M = Fe, Ga) and BDH-TTP (2,5-bis(1,3-dithiolan-2-ylidene)-1,3,4,6-tetrathiapentalene) are reported.

2.1.1 Croconato complexes

As listed in the previous paragraph, excellent results have been obtained with oxalato complexes. Recently, a class of organic ligands has attracted much

a)   b)   c)   d)

attention because of the coordination modes and bite parameters comparable to the oxalato: the cyclic carboxoanions, $C_nO_n^{2-}$ (where n is equal to 4 (squarato), 5 (croconato) or 6 (rhodizonato)). These ligands show π-electrons delocalization over the ring. (Figure 2.1) [10] [11]

Oxalato   **Squarato**   **Croconato**   **Rhodizonato**

bite p. ca. 1.23   bite p. ca. 1.70   bite p. ca. 1.32
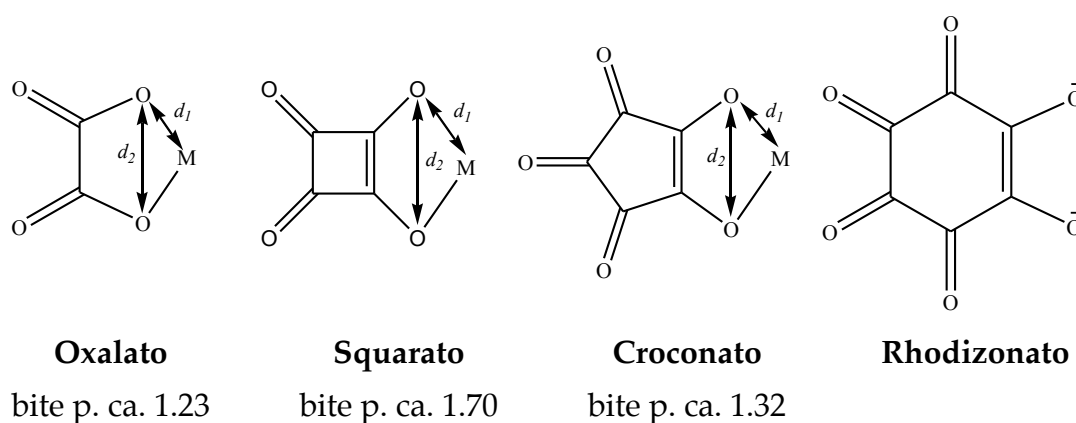
Figure 2.1: oxo ligands and their bite parameters: a) oxalato; b) squarato; c) croconato; d) rhodizonato.

In particular, the work described in this chapter focuses on croconato (croc^{2-} = $C_5O_5^{2-}$ = dianion of 4,5-dihydroxycyclopent-4-ene-1,2,3-trione) ligand whose coordination chemistry has shown to be particularly wide and rich, as observed by Julve et al. (see Scheme 2.1). [12] [13]

Recently, some complexes based on the croconato ligand have been obtained showing interesting magnetic properties [13] [14] [15] [16] and these results make these complexes promising building blocks for MMMs.
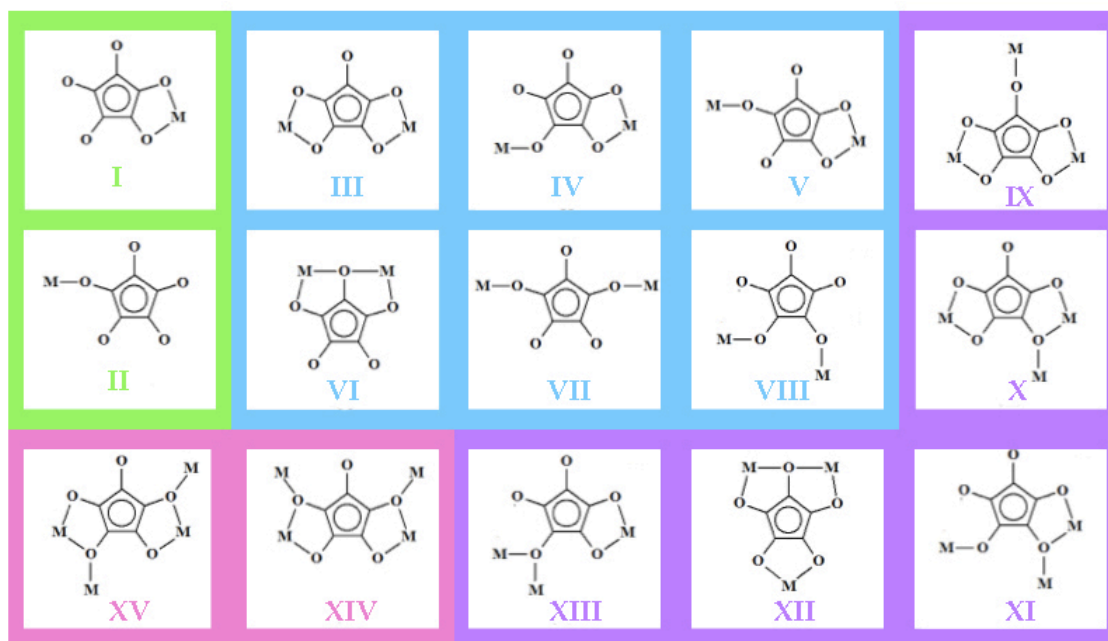
Scheme 2.1: croconato $(C_5O_5)^{2-}$ chelating modes (color code, green: mono-metallic [7] [17] [14]; pale blue: bi-metallic [18]; purple: tri-metallic [18f, h][19]; pink: tetra-metallic [17d] [19c] coordination)

Two interesting hybrid materials based on the paramagnetic $Fe(croc)_3^{3-}$ have been obtained: α - [(BEDT-TTF)$_5$] [Fe(croc)$_3$]·5H$_2$O, the first example of chirality-induced α-phase and the only known pentamerized (θ_{51}) phase) and β - [(BEDT-TTF)$_5$] [Fe(croc)$_3$]·C$_6$H$_5$CN, one of the very few examples of paramagnetic molecular metals. [7] [20] In these materials the croconato complexes play a crucial role for different aspects. Firstly, the octahedral geometry induces stack segregation in the crystal packing favoring the conductivity of BEDT-TTF layers. In fact, the tetrahedral and octahedral geometry favors the stacking of the conducting organic molecule as BEDT-TTF or BDH-TTP while square planar geometry favor alternating stacks leading to the semiconducting or even insulating state.

Moreover in the α – [(BEDT-TTF)$_5$] [Fe(croc)$_3$]·5H$_2$O, the chirality of croconato complexes influences the BEDT-TTF molecules packing through supramolecular contacts between the two networks. [20]

2.1.2 BDH-TTP

Among the wide class of organic donors, the BEDT-TTF has undoubtedly produced the highest number of 2D superconducting materials. This molecule belongs to the class of tetratiafulvalenes (TTFs) that are well-known π -electron donors. [1] [4] The planarity of the TTF moiety allows efficient close packing, maximizing $\pi - \pi$ orbital overlap between adjacent molecules that interact each other also through S $\cdots$ S contacts between the four polarizable S atoms.
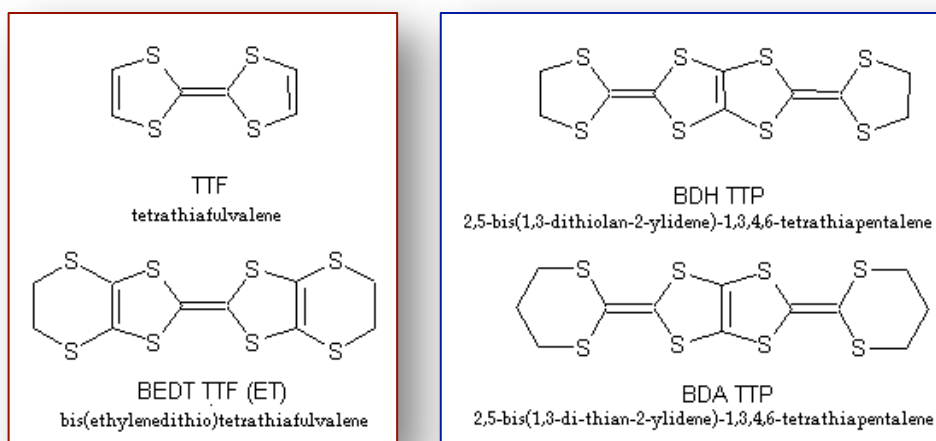

Figure 2.2: organic donors with (left) and without (right) TTF moiety

Recently, one BEDT-TTF structural isomer have been shown its potential as conducting carrier, although it contains no TTF moiety: the 2,5-bis(1,3-dithiolan-2-ylidene)-1,3,4,6-tetrathiapentalene, (BDH-TTP). [21]
BDH-TTP is shown in Figure 2.3.
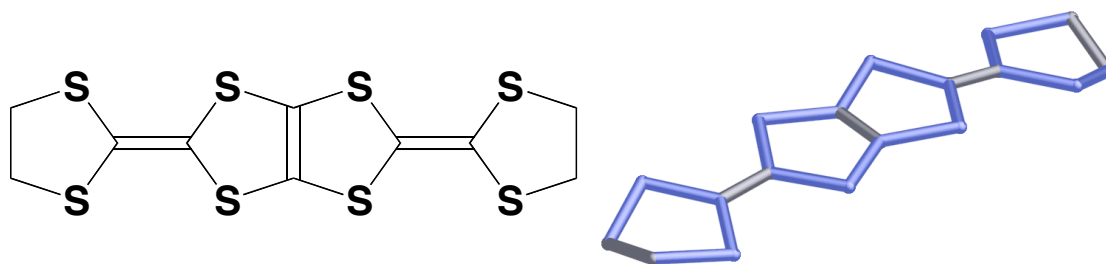
Figure 2.3: Scheme of the BDH-TTP

BDH-TTP has an almost planar configuration due to the rigidity of the two five-membered rings. [21] [22] Generally, in MMMs BDH-TTP adopts a κ-type packing in which face-to-face dimers are orientated orthogonal to each other, as reported in literature: κ- $(BDH\text{-}TTP)_2FeCl_4$ [23], κ- $(BDH\text{-}TTP)_2PF_6$ [21], κ-$(BDH\text{-}TTP)_4[FeNO(CN)_5]$ [24], κ- $(BDH\text{-}TTP)_4Hg_3Br_8$ [25], κ- $(BDH\text{-}TTP)_4Hg_3Cl_8$ [25] and κ- $(BDH\text{-}TTP)_4[Hg(SCN)_4] \cdot C_6H_5NO_2$. [26] Interestingly most of the superconductors reported in literature have shown κ-type packing of the organic donors.

The conducting properties of some examples of the hybrid materials based on this organic donor are reported in Table c.1, clearly showing how this molecule is a promising conductivity carrier. As it shown, the metallic state is stabilized down to low temperature. [27] [28] [22] Some examples are reported in Table 2.1.

Counterion	Solvent	$\sigma_{RT}(Scm^{-1})$
I_3^-	PhCl	230 (metallic T>2.0K) [21]
$FeCl_4^-$	EtOH/PhCl	39 (metallic T>1.5K) [23]
$(BDH\text{-}TTP)_4[FeNO(CN)_5]$	EtOH/PhNO$_2$	3.0-6.0 S/cm (M T>4.2K) [24]
PF_6^-	TCE	102 (metallic T>2.2K)[21]
$(BDH\text{-}TTP)_5[Cr(phen)(NCS)_4]$ $2CH_2Cl_2$	CH_2Cl_2	2.92 (metallic T>150 K, P >10 Kbar) [29]
$(BDH\text{-}TTP)_4Hg_3Br_8$	THF	40 (metallic T>4.2K) [25]

Table 2.1: examples of compounds based on BDH-TTP

Moreover, Cyclic Voltammetry (CV) in PhCN/CS$_2$ of BDH-TTP (and BEDT-TTF) shows two reversible oxidation peaks: E_1 = +0.56 (+0.61, BEDT-TTF); E_2 = +0.82 (+0.87, BEDT-TTF). This demonstrates that BDH-TTP can be oxidized easier than BEDT-TTF while the ΔE is unaltered. [21]

For these reasons, BDH-TTP has been selected in this work as conducting carrier for obtaining new magnetic/conducting MMMs.

The synthesis, X-ray structure and physical properties of two new materials based on Fe(croc)$_3^{3-}$ and Ga(croc)$_3^{3-}$ complexes with BDH-TTP are reported in this work. The electronic properties of [(BDH-TTP)$_6$] [Fe^{III}(croc)$_3$] have been also investigated using its nonmagnetic isostructural analog, [(BDH-TTP)$_6$] [Ga^{III}(croc)$_3$] as reference.

2.2 Results and discussion

2.2.1 Synthesis of [(BDH-TTP)$_6$] [Fe(croc)$_3$] ·CH$_2$Cl$_2$ (1) and [(BDH-TTP)$_6$] [Ga(croc)$_3$] ·CH$_2$Cl$_2$ (2)

As reported in the Experimental Section (see Section 2.4), **(1)** and **(2)** were obtained through electrocrystallization using CH$_2$Cl$_2$ as solvent, (donor : anion ratio (3:1), current density (0.2 μA cm^{-2}) and the crystallization time of ca. 20.

2.2.2 Crystal Structure of [(BDH-TTP)$_6$] [Fe(croc)$_3$] ·CH$_2$Cl$_2$ (1) and [(BDH-TTP)$_6$] [Ga(croc)$_3$] ·CH$_2$Cl$_2$ (2)

Both complexes crystallize in the monoclinic crystal system with the spatial group *C2/c*. Compounds **(1)** and **(2)** are crystallographically isostructural. Each unit cell includes four [M^{III}(croc)$_3$]$^{3-}$ (M = Fe, Ga) anions, 24 BDH-TTP molecules or cations, and four dichloromethane molecules as co-crystallized solvents, and 0.5 [M^{III}(croc)$_3$]$^{3-}$ anion, 3 BDH-TTP molecules or cations, and 0.5 CH$_2$Cl$_2$ are crystallographically independent. The anion is located on a two-fold axis passing parallel to the *b* axis (Figure c.4). Two croconato anions are structurally identical (Tables Z.1 and Z.2) and each ligand possesses 2- charges to form [M(croc)$_3$]$^{3-}$ with tri-valent Fe or Ga.

The labeling schemes for [Fe(croc)$_3$]$^{3-}$ anion and for BDH-TTP are shown in Figure 2.4, 2.5, respectively.
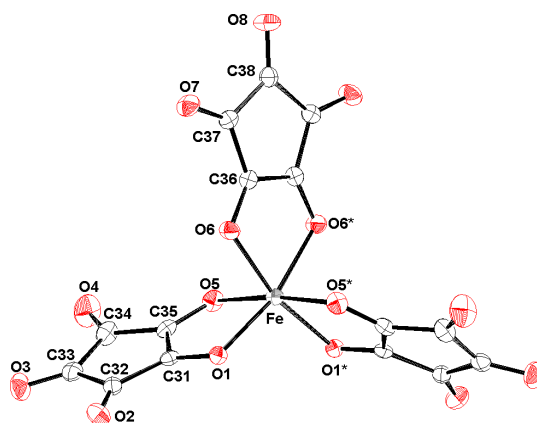
Figure 2.4: ORTEP drawing of $[Fe(C_5O_5)_3]^{3-}$ in complex **1** with the selected atom numbering scheme based on the unique atoms (50% probability ellipsoids). Symmetry operation (*):–x+2, y, –z+1/2
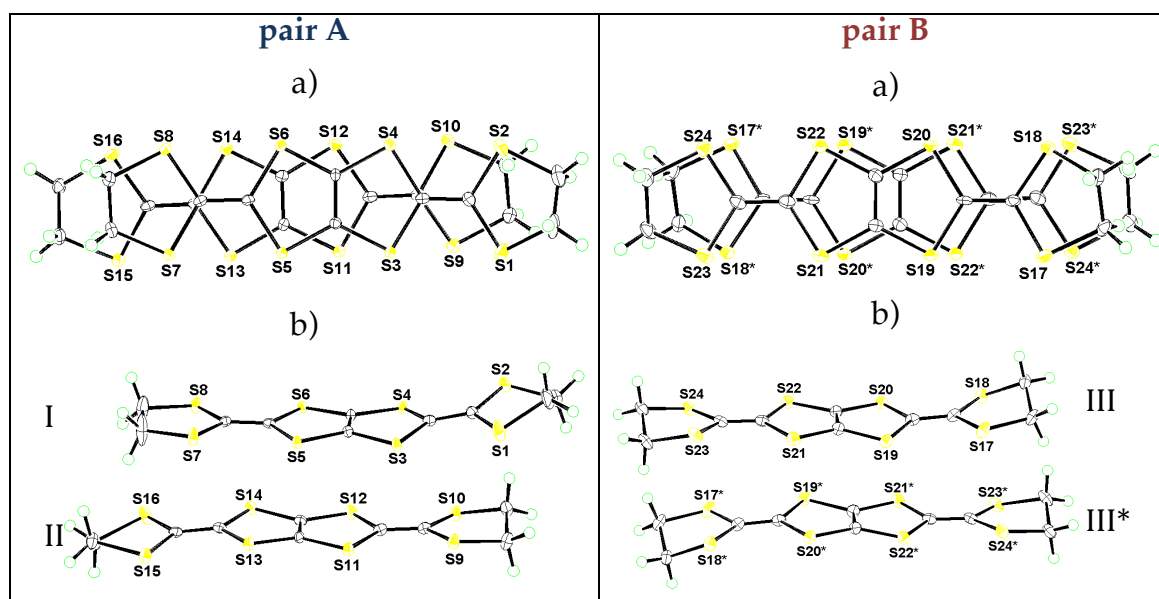
Figure 2.5: ORTEP drawing of $(BDH\text{-}TTP)_2^+$ (pair **A**, *left*) and of $(BDH\text{-}TTP)_2^+$ (pair **B**, *right*) in **(1)** with the selected atom numbering scheme (50% probability ellipsoids). (a) top view and (b) side view. Symmetry operation for pair **B** (*) : –x+3/2, –y–3/2, –z

The structures of **(1)** and **(2)** consist of alternating layers of BDH-TTP molecules separated by layers of $Fe(croc)_3^{3-}$ and $Ga(croc)_3^{3-}$ complexes. (Figure 2.6, left and right, respectively)
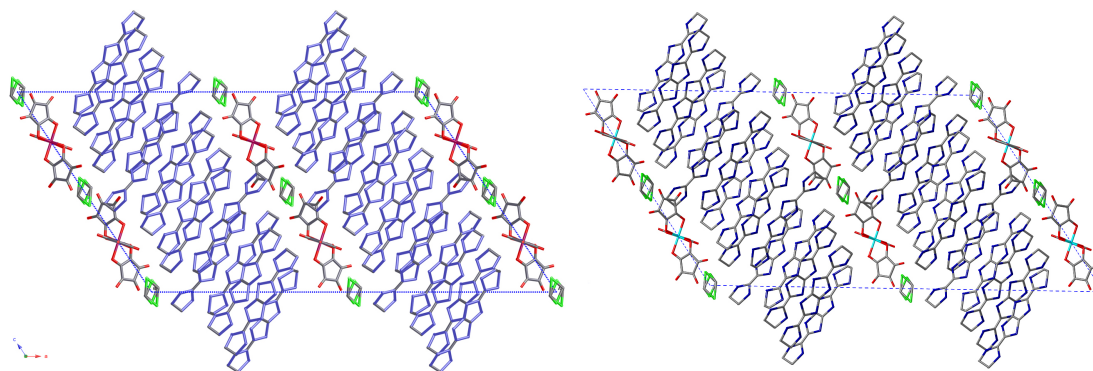
Figure 2.6: Molecular Packing of [(BDH-TTP)$_6$] [Fe(croc)$_3$] ·CH$_2$Cl$_2$ **(1)** (*left*) and of of [(BDH-TTP)$_6$] [Fe(croc)$_3$] · CH$_2$Cl$_2$ **(2)** (*right*) [H atoms have been omitted for clarity; color code: grey = C; red = O; blue = N; green = Cl]

The organic layer is formed by three independent BDH-TTP molecules, (I, II, III), are also identical, as estimated from bond distances and angles (Figures 2.5, Tables Z.1 and Z.2), and a formal charge of +0.5 is estimated for each molecule. Molecules I and II are dimerized to form the pair A with the shortest S…S contact of 3.6363(12) Å for **(1)** and 3.5992(18) Å for **(2)**, respectively (Table 2.2). Molecule III is also dimerized with molecule III* to form the pair B, the latter being related with the former by symmetry operation of (–x+3/2, –y–3/2, –z), with the shortest contact of 3.5910(13) Å for **(1)** and 3.5840(18) Å for **(2)**, respectively.
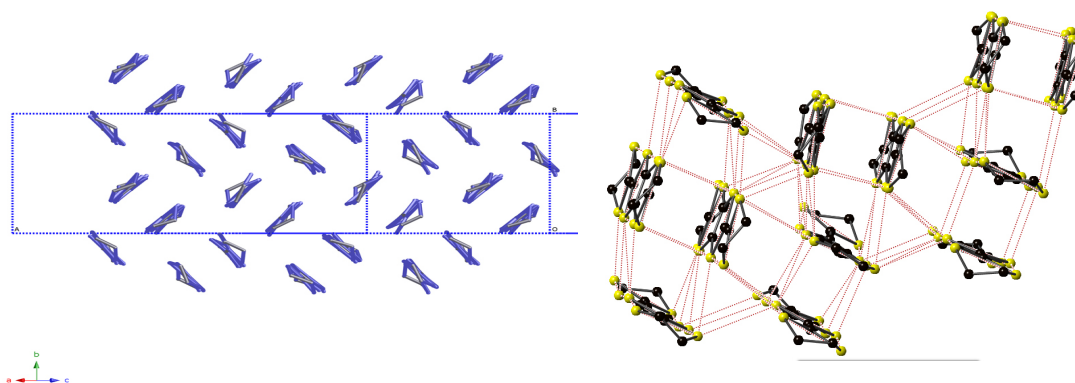
Figure 2.7: Molecular packing of BDH-TTP in the **(1)** (k-type). (*left*) Short S – S contacts are indicated by dashed lines. (*right*)

Therefore the BDH-TTP molecules are arranged in dimers almost orthogonal (ca. 33°), leading to a κ-type molecular packing for **(1)** and **(2)**, shown in Figure 2.7. The S – S interactions are shown in Figure 2.7 and are shorter than the sum of the Van der Waals radii.

	(1)	**(2)**
S16-S8	3.8810(14)	3.7607(19)
S8-S14	3.7011(13)	3.6286(18)
S14-S6	3.6411(12)	3.5992(18)
S6-S12	3.7202(13)	3.6936(18)
S12-S4	3.8051(12)	3.7544(18)
S4-S10	3.8218(13)	3.8182(18)
S10-S2	4.5881(14)	4.5360(20)
S15-S7	4.1137(14)	4.1747(19)
S7-S13	3.8346(14)	3.8867(18)
S13-S5	3.6363(12)	3.6184(18)
S5-S11	3.8103(12)	3.8028(18)
S11-S3	3.7552(12)	3.7277(18)
S3-S9	3.6274(13)	3.6275(18)
S9-S1	3.9726(15)	3.9600(20)
S24-S17*	3.8160(14)	3.7925(19)
S22-S17*	4.6677(14)	4.3168(19)
S22-S19*	3.5910(13)	3.5840(18)
S20-S19*	4.2468(13)	3.9571(18)
S20-S21*	3.6408(13)	3.6305(18)
S18-S21*	4.6648(14)	4.3542(19)
S18-S23*	4.0447(14)	3.9924(19)

Table 2.2: Selected atom-atom distances [Å] for complexes **(1)** and **(2)**. Symmetry transformations used to generate equivalent atoms: * –x+3/2, –y–3/2,–z

The anionic layer is formed by isolated $[M^{III}(croc)_3]^{3-}$ units and solvent molecules. M^{III} ion is surrounded by three croconato ligands. The packing of $M^{III}(croc)_3]^{3-}$ anions is organized in two rows, each formed only by Λ or Δ enantiomer, as clearly shown in Figure 2.8. The presence of both enantiomers in equal amounts leads to achiral compounds, as previously observed for similar compounds based on $[Fe^{III}(croc)_3]^{3-}$. [7]
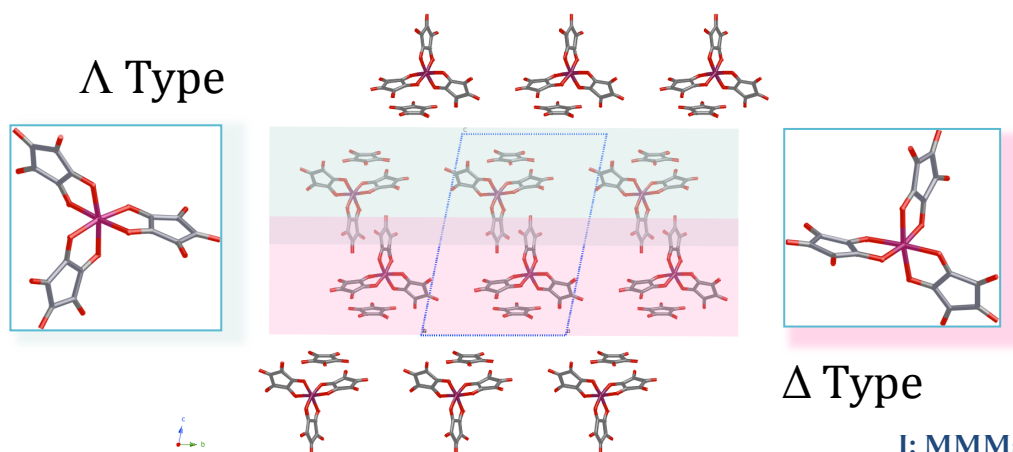
Figure 2.8: The Λ and Δ enantiomers rows in the packing of [Ga(croc)$_3$]^3 in the **(2)** compound.

2.2.3 Physical Properties[*]

2.2.3.1 *Electronic Structure*

In Figure 2.9, the k-type arrangement with dimerized molecules of BDH-TTP molecules in a conducting plane and the labeling of transfer integrals between them is shown. The valence of BDH-TTP seems to be uniform considering the length of the central-carbon double-bond. The overlap integrals between HOMOs are calculated on the basis on the extended Hückel model [30] and are tabulated in Table 2.3. The overlap integrals between dimerized molecules are twice as large as the other integrals. Values for **(2)** are almost the same as for **(1)**. Intermolecular contacts in the κ-type packing are shorter than the sum of the Van der Waals radii, as shown in Figure 2.7.
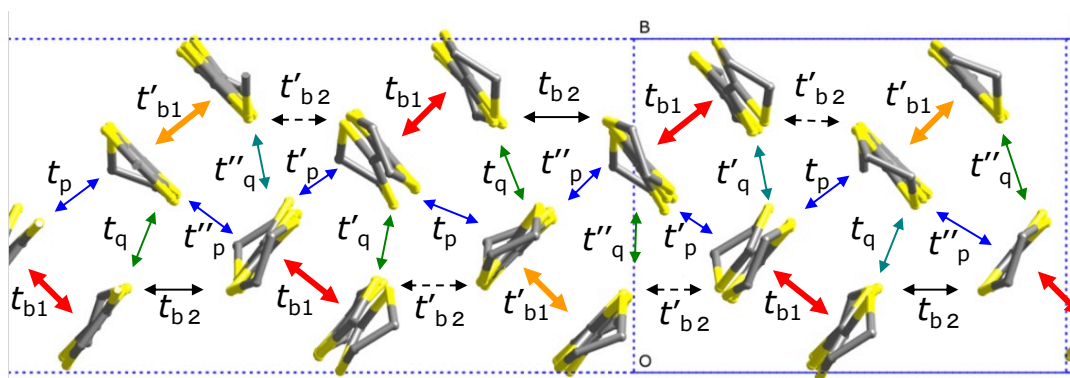
Figure 2.9: k-type donor arrangement in a conducting plane with overlap integrals between molecules.

	t_{b1}	t'_{b1}	t_{b2}	t'_{b2}	t_p	t'_p	t''_p	t_q	t'_q	t''_q
M = Fe	21.6	21.4	13.1	13.9	5.5	7.0	11.6	-0.91	-7.0	-5.0
M = Ga	22.8	20.7	12.9	14.5	5.5	7.4	9.3	-0.26	-7.3	-6.4

Table 2.3: Overlap integrals for M=Fe and M=Ga salts (in a unit of 10^{-3})

---

[*] Physical measurements were performed by the group of Prof. Hiroshi Ito, Nagoya University (Japan)

2.2.3.2 *Conductivity*

The r.t. conductivity, measured at 4 kbar, is about 10 S/cm for **(1)** and **(2)**.

The temperature dependence of resistivity under pressure up to 15 kbar for **(1)** and **(2)** is shown in (Figure 2.10, a) and (Figure 2.10, b), respectively. Both salts exhibit a metallic behavior from room temperature down to ca. 100 K; below this temperature the conductivity becomes thermally activated with typical activation energy of 1~2 meV. These behaviors are similar to the previously reported α - [(BEDT-TTF)$_5$] [Fe(croc)$_3$]·5H$_2$O and β - [(BEDT-TTF)$_5$] [Fe(croc)$_3$]·C$_6$H$_5$CN salts. [7] Under applied pressure, the non-metallic behavior is suppressed at 7 kbar, as shown in Figure 2.10 (a). For the M=Ga salt **(2)**, non-metallic phase remains even at applied pressure of 15 kbar. (Figure 2.10, b)

The non-metallic phase at ambient pressure, found for both salts, may be caused by the strong electron correlation of the dimerized half-filled Mott system. [31] The suppression of the non-metallic phase under applied pressure is due to the increase of the bandwidth with respect to the Coulomb energy. The difference in the resistivity behavior under pressure among samples may stem from the difference in the quality of the samples.
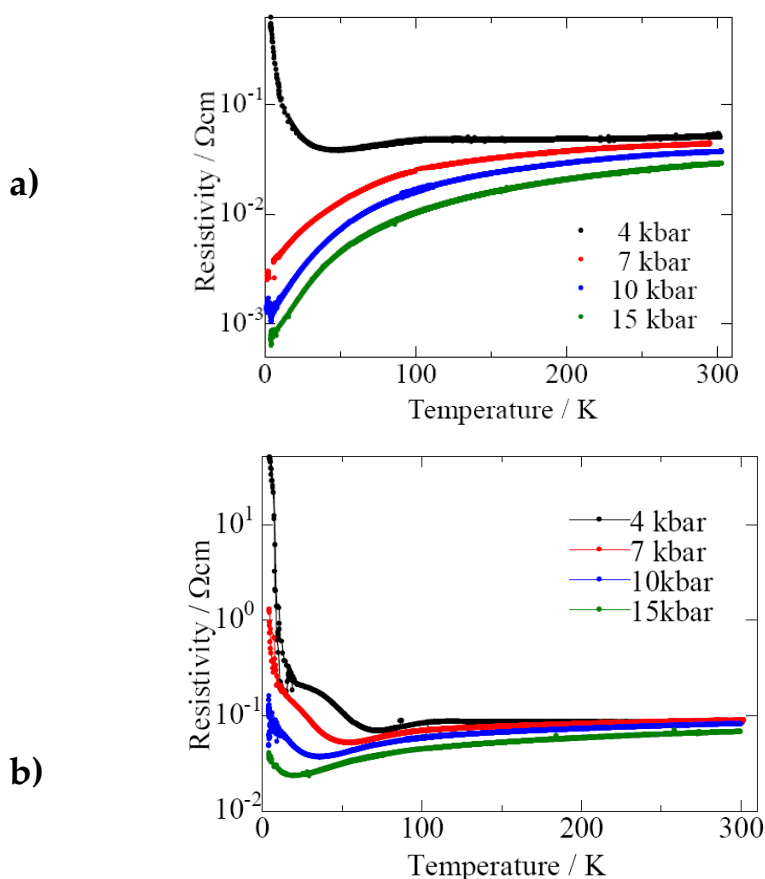
a)

b)

2.2.3.3 *ESR*

In Figure 2.11, first-derivative ESR spectra of the two salts at room temperature is shown. The conducting plane was aligned perpendicular to the external magnetic field. For **(1)**, Fe^{3+} signals of sharp one at g=3.76, and broad ones at g=12.4, g=1.50, g=0.94 were observed in addition to the p-electron signal at g~2.00. When the external field was rotated with respect to the conducting plane, g-value of the sharp Fe^{3+} signal changes in the range of g=3.7~4.6. The signal at g=3.7~4.6 is interpreted as caused by the high-spin (S=5/2) state of Fe^{3+} in the distorted octahedral crystal field from the ligands. [32] [33]

For the **(2)** compound, only p-electron signal was observed. When the external field was rotated with respect to the conducting plane, the g-value and linewidth changed in the range of 2.003~2.011 and 43~52 G, respectively.
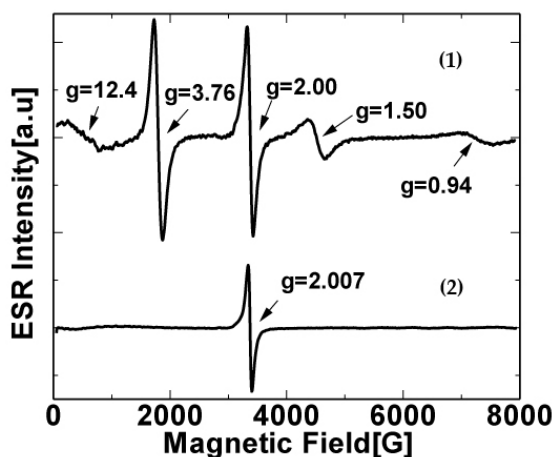
Figure 2.11: ESR signals of **(1)** and **(2)** salts under magnetic field applied perpendicular to the conducting plane.

In Figure 2.12(a), the temperature dependence of the spin susceptibility for the p-electron of **(1)** obtained by integrating twice the ESR signal at g~2.00 with magnetic field is shown. The susceptibility was Pauli-like above 50 K. With decreasing the temperature, the susceptibility once increased with a peak at 30 K, and was suppressed away below 20 K with decreasing g-value and

diverging linewidth as shown in Figure 2.12(b). These behaviors are consistent to the metallic state at high temperature and the insulating phase at low temperature. The suppression of the p-electron signal below 20 K may be caused by antiferromagnetic exchange interactions. On the other hand, the ESR intensity of the Fe^{3+} signals increased obeying the Curie law with decreasing the temperature.
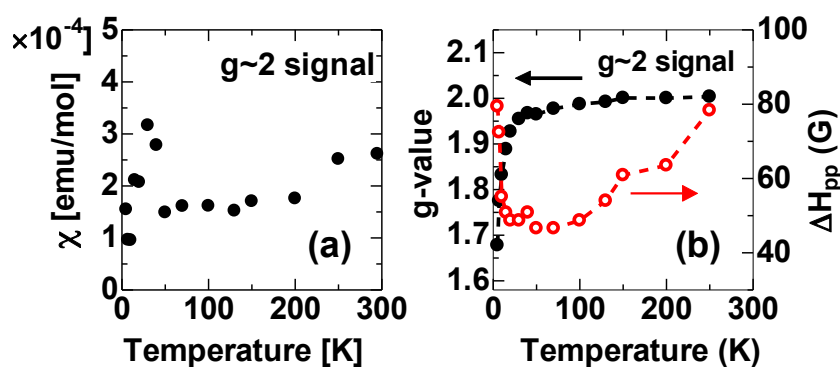
Figure 2.12: Temperature dependence of the spin susceptibility (a), g-value and linewidth (b) for the p-electron of the **(1)** salt under magnetic field applied parallel to the conducting plane.
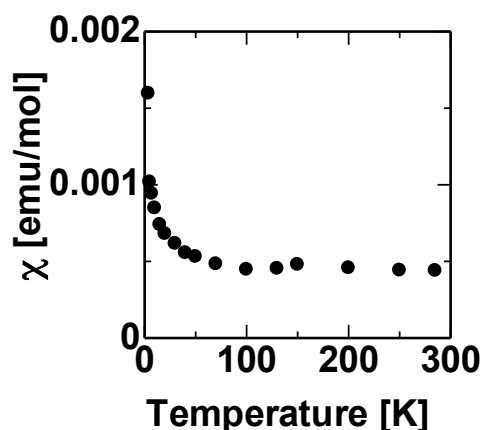
Figure 2.13: Temperature dependence of the spin susceptibility of the **(2)** salt under magnetic field applied perpendicular to the conducting plane.

In Figure 2.13, the temperature dependence of the spin susceptibility for the **(2)** salt is shown. Above 100 K, the susceptibility showed Pauli-like behavior with Lorentzian line shape, which is consistent with the metallic state. Below 100 K, it turned to show Curie-like behavior with Curie constant of $C=2.86\times10^{-3}$

emuK/mol, which originates from defect sites with concentration of 1 spin per 400 dimers. This is also confirmed from the fact that the ESR signal became asymmetric with Gaussian line shape below 50 K.

2.2.3.4 *Magnetic measurements for* **(1)**

Magnetic measurements for **(1)** are shown in Figure 2.14. The χ_mT value is ca 4.4 emu K mol^{-1}, close to that reported in literature for similar compounds (4.53 emu K mol^{-1} for [TBA$_3$] [Fe^{III}(croc)$_3$]; 4.5 emu K mol^{-1} for α - (BEDT-TTF)$_5$[Fe(croc)$_3$·5H$_2$O]). [7] [15] At ~ 15 K the χ_mT value decreases sharply up to ca 3.9 emu emu K mol^{-1} at 2K. The curve is well fitted with a simple monomer model in which there are no interactions among Fe^{3+} ions. The sharp decreasing could be due to a a zero field splitting (ZFS) of the S = 5/2 spin ground state for Fe^{III} ions. The ZFS parameter, |D| is 0.95 cm^{-1} and the g value is 2.0096. The isothermal magnetization at 2 K (see the inset in Figure c.14) has been done for confirming the ground state S = 5/2. In fact, the value close to 5 μ_B is consistent for isolated high spin Fe^{III} ions. Moreover, the Brillouin function for a S = 5/2 isolated ion fits well the experimental curve. In conclusion, the measurements suggest that **(1)** is a paramagnet with a ground state of S = 5/2.

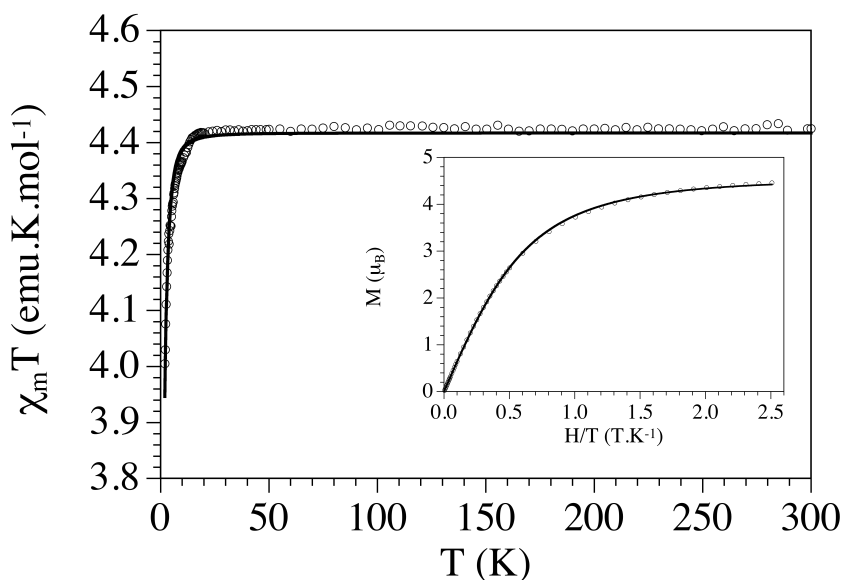**Figure 2.14:** magnetic susceptibility versus temperature for **(1)** and the isothermal magnetization for the same sample at 2 K (inset)

2.3 CONCLUSIONS

Two new molecular materials: $[(BDH\text{-}TTP)_6]$ $[Fe(croc)_3]$ $\cdot CH_2Cl_2$ **(1)** and $[(BDH\text{-}TTP)_6]$ $[Ga(croc)_3]$ $\cdot CH_2Cl_2$ **(2)** have been synthesized.

These two compounds are isostructural as demonstrated by X-ray structural characterization. By comparing the magnetic properties of these two compounds it has been possible to investigate magnetic contribution of both networks. In fact, in **(2)**, the $Ga^{III}(croc)_3^{3-}$ complex does not contribute to the magnetism of the material as demonstrated by the EPR measurements which show the only contribution of the organic donor.

Conductivity measurements show that these two materials behave as semiconductors with rather high conductivity values at r.t. and 20 kbar pressure, $\sim$ 10 S/cm for **(1)** and **(2)**. The conductivity increases as applied pressure is increased. In fact, at pressure values above 7 kbar a suppression of the M-I transition occurs for **(1)** that shows a metallic behavior down to low temperature. For **(2)** a suppression of Metal – Insulator transition is not observed, but a metallic behavior from r.t. down to 100 K when a 15 kbar pressure is applied, is found. The explanation of these different behaviors is under investigation.

Magnetic measurements demonstrate a paramagnetic behavior of **(1)**, as expected for magnetically isolated Fe(III) metal ions with S = 5/2 ground state.

(1) and **(2)** are achiral since Λ and Δ enantiomers of $M^{III}(croc)_3^{3-}$ are both present in equal ratio in the crystal lattice. It can be suggested that one of the possible perspectives for a future development of these materials, is to prepare enantiomeric-pure compounds in order to study the influence of chirality in the molecular packing pattern in MMMs.

2.4 EXPERIMENTAL SECTION

Single crystal X-ray data were collected at low temperature on a Bruker AXS SMART-APEX/CCD area detector using graphite monochromated Mo K*a* radiation (0.71079 Å). Since the crystal of complex 2 was very small, reflections in a 2q range of 3.74–46.00° were used for structure analysis. The structures were solved by direct methods using SIR97, [34] and structure refinements were carried out using Full-matrix least-squares calculations (SHELXL-97). [34] Non-hydrogen atoms except for solvent molecule were refined anisotropically, and the hydrogen atoms were treated using a riding model.

2.4.1 Synthesis of [TBA]$_3$[Fe^{III}(croc)$_3$]

The synthesis of the [TBA]$_3$[Fe^{III}(croc)$_3$] was performed as reported in literature and according to Scheme 2.2. [15] To 0.69 g (3.50 mmol) of H$_2$C$_5$O$_5$ · 3H$_2$O [22] in 50 mL of distilled water were added 0.28 g (7.00 mmol) of NaOH and 1.14 g (3.50 mmol) of (TBA)Br (molar ratio 1:2:1); then 0.19 g (1.17 mmol) of FeCl$_3$ (molar ratio H$_2$C$_5$O$_5$/FeCl$_3$, 3:1) was added drop-wise to the reaction mixture. A brown solid, partially soluble in water, precipitates immediately. It was extracted with CH$_2$Cl$_2$, and anhydrous Na$_2$SO$_4$ was added to the resulting violet solution; this solution was then filtered and roto-evaporated. A lacquer- like solid was obtained and it was recrystallized from a MeOH/Et$_2$O (1/1) mixture to give dark crystals.
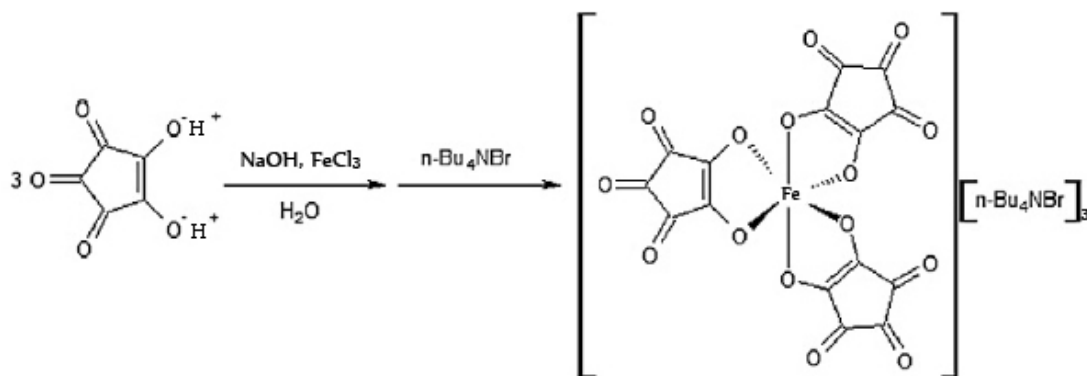
Scheme 2.2: Synthesis of [TBA]$_3$[Fe^{III}(croc)$_3$]

Although this salt is not chiral, there are present both of Δ and Λ enantiomers. The cyclic voltammetry made in ACN in the range 0.0 – 1.5 V shows no oxidation or reduction peaks: for this reason this complex was selected as BDH-TTP counterion, that shows a monoelectronic reversible oxidation peak at 0.46 V. [15] [21]

2.4.2 Synthesis of [TBA]$_3$[Ga^{III}(croc)$_3$]

The synthesis of [TBA]$_3$[Ga^{III}(croc)$_3$] was performed as reported in literature. [16] In dry box, 372 mg (1.71 mmol) of K$_2$C$_5$O$_5$ were added to an aqueous solution of 100 mg (0.57 mmol) of GaCl$_3$. After 1 hour stirring at r.t., 551 mg (1.71 mmol) of TBABr have been added. A yellow precipitate was obtained and it was collected by filtration, washed with distilled water, dried in oven at 80° C. The product was recrystallized by redissolving in acetone and adding Et$_2$O
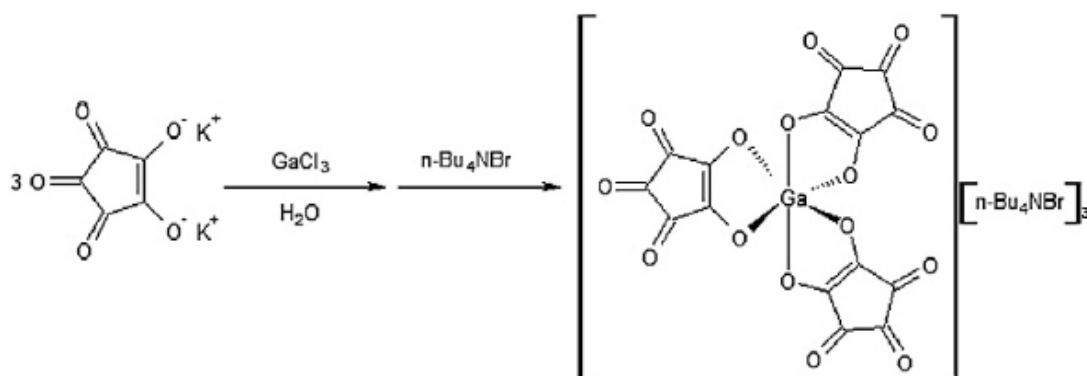
Scheme 2.3: Synthesis of [TBA]$_3$[Ga^{III}(croc)$_3$]

2.4.3 Synthesis of [(BDH-TTP)$_6$] [Fe(croc)$_3$] ·CH$_2$Cl$_2$ (1)*

Dark needle crystals of κ-[Fe(croc)$_3$][(BDH-TTP)$_6$]·CH$_2$Cl$_2$ **(1)** were grown by using the electrocrystallization method illustrated in Appendix B.

BDH-TTP (35.0 mg) was dissolved in 10 mL of CH$_2$Cl$_2$, and the solution was placed in the anodic chamber of the cell. [TBA]$_3$[Fe^{III}(croc)$_3$] (33.4 mg, donor : anion molar ratio 3:1) was dissolved in 15 mL of CH$_2$Cl$_2$, and this solution was divided into the anodic and cathodic compartments. A current density of 0.2 µA cm^{-2} was applied. Single crystals were grown at 25 °C on a platinum wire electrode for a period of 20 days.

Crystallographic data are reported below:

Crystal data for **(1)**: C$_{76}$H$_{50}$Cl$_2$FeO$_{15}$S$_{48}$, M_r = 2868.79, monoclinic, $C2/c$, a = 44.603(7) Å, b = 10.6036(16) Å, c = 25.964(4) Å, b = 123.738(3)°, V = 10211(3) Å^3, Z = 4, T = 100 K, $F(000)$ = 5816, m(Mo$_{K\alpha}$) = 1.379 mm^{-1}. Using 655 parameters, wR_2= 0. 1366 (14836 unique reflections), R_1= 0.0633 (11720 reflections with $I >$ 2s(I)).

---

* X-ray structural characterization was performed by the group of Prof. Masahiro Yamashita, Tohoku University, Sendai (Japan)

2.4.4 Synthesis of [(BDH-TTP)$_6$] [Ga(croc)$_3$] ·CH$_2$Cl$_2$ (2)

Brown crystals of κ-[Ga(croc)$_3$][(BDH-TTP)$_6$]·CH$_2$Cl$_2$ **(2)** were grown by using the electrocrystallization method illustrated in Appendix B.

BDH-TTP (32.0 mg) was dissolved in 10 mL of CH$_2$Cl$_2$, and the solution was placed in the anodic chamber of the cell. [TBA]$_3$[Ga^{III}(croc)$_3$] (31.0 mg, donor : anion molar ratio 3:1) was dissolved in 15 mL of CH$_2$Cl$_2$, and this solution was divided into the anodic and cathodic compartments. A current density of 0.2 μA cm^{-2} was applied. Single crystals were grown at 25 °C on a platinum wire electrode for a period of 20 days.

Crystallographic data are reported below:

Crystal data for **(2)**: C$_{76}$H$_{50}$Cl$_2$GaO$_{15}$S$_{48}$, M_r = 2882.66, monoclinic, $C2/c$, a = 44.006(7)Å, b = 10.5748(17) Å, c = 26.171(4) Å, b = 123.807(3)°, V = 10120(3) Å^3, Z = 4, T = 100 K, $F(000)$ = 5836, m(Mo$_{K\alpha}$) = 1.245 mm^{-1}. Using 655 parameters, wR_2= 0.0816 (7043 unique reflections), R_1= 0.0386 (4856 reflections with $I > 2s(I)$)

2.4.5 Physical Measurements

Conductivity

The electrical resistivity was measured using a four-terminal dc method with a measuring current of 0.1-0.01 mA. Four platinum wires were attached to a single crystal with carbon paste within the conducting plane. The measuring current was alternated in order to eliminate thermoelectric effects. Typical cooling rate was 1 K/min. The hydrostatic pressure was applied via Daphne 7373 oil with a BeCu pressure cell with an inner core of NiCrAl. The pressure was applied at room temperature and the cell was clamped with screws. The pressure decreased by ca. 2 kbar at low temperatures compared to that at room temperature. [15] The temperature was monitored with a calibrated Cernox thermometer.

ESR

The electron spin resonance measurements were performed using a Bruker EMX X-band spectrometer equipped with an OXFORD ESR900 gas flow cryostat for temperatures between room temperature and 5 K. A single crystal was fixed to a Teflon substrate with a small amount of Apiezon N grease. The absolute magnitude of the susceptibility and the g-value were calibrated using $CuSO_4 \cdot 5H_2O$ and diphenylpicrylhydrazyl (DPPH) as standards, respectively.

Magnetic measurements

The magnetic susceptibility measurements were carried out in the temperature range 2-300 K with an applied magnetic field of 0.1 T on a polycrystalline sample of **(1)** and **(2)** with a Quantum Design MPMS-XL-5 SQUID susceptometer. The susceptibility data were corrected for the sample holder previously measured using the same conditions and for the diamagnetic contributions of the salt as deduced by using Pascal´s constant tables (χ_{dia} = -378.8x10^{-6} emu mol^{-1}).

REFERENCES

[1] "Multifuctional Materials of interest in Molecular Electronics", M. L. Mercuri, P. Deplano, A. Serpe, F. Artizzu, Chapter in *Handbook of Multifunctional Molecular Materials*, Pan Stanford Publishing, eds Lahcène Ouahab **2011**

[2] M. Salidu, F. Artizzu, P. Deplano, M. L. Mercuri, L. Pilia, A. Serpe, L. Marchiò, G. Concas, F. Congiu, *Dalton Trans.*, **2009**, 557–563

[3] (a) A.W. Graham, M. Kurmoo, P. Day, *J. Chem. Soc., Chem. Commun.*, **1995**, 2061; (b) T. Enoki, A. Miyazaki, *Chem. Rev.* 104, **2004**, 5449; H. Kobayashi, H.B. Cui, A. Kobayashi, *Chem. Rev.* 104, **2004**, 5265; (c) M. Kurmoo, A.W. Graham, P. Day, S.J. Coles, M.B. Hursthouse, J.L. Caulfield, J. Singleton, F.L. Pratt, W. Hayes, L. Ducasse, P. Guionneau, *J. Am. Chem. Soc.*, 117, **1995**, 12209; (d) L. Martin, S.S. Turner, P. Day, F.E. Mabbs, E.J.L. McInnes, *J. Chem. Soc., Chem. Commun.*, **1997**, 1367; (e) S. Rashid, S.S. Turner, P. Day, J.A.K.

Howard, P. Guionneau, E.J.L. McInnes, F.E. Mabbs, R.J.H. Clark, S. Firth, T. Biggs, *J. Mater. Chem.* 11, **2001**, 2095

[4] M. L. Mercuri, P. Deplano, L. Pilia, A. Serpe, F. Artizzu, *Coordination Chemistry Reviews* 254, **2010**, 1419–1433

[5] H. Fujiwara, E. Fujiwara, Y. Nakazawa, B.Zh. Narymbetov, K. Kato, H. Kobayashi, A. Kobayashi, M. Tokumoto, P. Cassoux, *J. Am. Chem. Soc.* 123, **2001**, 306

[6] E. Coronado, J.R. Galán-Mascarós, C.J. Gómez-García, V.N. Laukhin, *Nature* 408, **2000**, 447

[7] E. Coronado, S. Curreli, C. Giménez-Saiz, C. Gómez-Garcia, P. Deplano, M. L. Mercuri, A. Serpe, L. Pilia, C. Faulmann, E. Canadell, *Inorganic Chemistry*, **2007**, Vol. 46, (*11*) 4446-4457

[8] E. Coronado, P. Day, *Chem. ReV.* **2004**, *104*, 5419

[9] (a) Kurmoo, M.; Graham, A. W.; Day, P.; Coles, S. J.; Hursthouse, M. B.; Caulfield, J. L.; Singleton, J.; Pratt, F. L.; Hayes, W.; Ducasse, L.; Guionneau, P. *J. Am. Chem. Soc.* **1995**, *117*, 12209. (b) Martin, L.; Turner, S. S.; Day, P.; Mabbs, F. E.; McInnes, E. J. L. *J. Chem. Soc. Chem. Commun.* **1997**, 1367. (c) Rashid, S.; Turner, S. S.; Day, P.; Howard, J. A. K.; Guionneau, P.; McInnes, E. J. L.; Mabbs, F. E.; Clark, R. J. H.; Firth, S.; Biggs, T. *J. Mater. Chem.* **2001**, *11*, 2095

[10] X. Solans, M. Aguilb, A. Gleizes, J. Faus, M. Julve, M. Verdaguer, *Inorganic Chemistry*, 29, **1990**, 775 - 784

[11] A. Ranganathan, G. U. Kulkarni, *J. Phys. Chem. A*, 106, **2002**, 7813 – 7819

[12] Calatayud, M. L.; Sletten, J.; Julve, M.; Castro, I. *J. Mol. Struct.* **2005**, *741*, 121 and references therein;

[13] M. Atzori, E. Sessini, F. Artizzu, L. Pilia, A. Serpe, C. J. Gómez-García, C. Giménez-Saiz, P. Deplano, M. L. Mercuri, *Inorganic Chemistry*, **2012**, submitted

[14] I. Castro, M. L. Calatayud, F. Lloret, J. Sletten, M. Julve, *J. Chem. Soc., Dalton Trans.*, 2002, 2397

[15] S. Curreli, P. Deplano, C. Faulmann, M. L. Mercuri, L. Pilia, A. Serpe, E. Coronado, C. J. Gómez-Garcia, *Inorganica Chimica Acta* 359, **2006**, 1177–1183

[16] F. Artizzu, P. Deplano, L. Pilia, A. Serpe, L. Marchiò, K. Bernot, M. L. Mercuri, *Inorganica Chimica Acta* 370, **2011**, 474–481

[17] (a) Castan, P.; Deguenon, D. *Acta Cryst. Sect. C* **1991**, *47*, 2656; (b) Carranza, J.; Sletten, J.; Brennn, C.; Lloret, F.; Cano, J.; Julve, M. *Dalton Trans.* **2004**, 3997; (c) Wang, C.-C.; Yang, C.-H.; Lee, G.-H. *Inorg. Chem.* **2002**, *41*, 1015; (d) Gavilan, E.; Audebrand, N. *Polyhedron* **2007**, *26*, 5533;

[18] (a) Castro, I.; Sletten, J.; Faus, J.; Julve, M.; Journaux, Y.; Lloret, F.; Alvarez, S. *Inorg. Chem.* **1992**, *31*, 1889; (b) Carranza, J.; Sletten, J.; Brennn, C.; Lloret, F.; Cano, J.; Julve, M. *Dalton Trans.* **2004**, 3997; (c) Speier, G.; Speier, E.; Noll, B.; Pierpont, C. G. *Inorg. Chem.* **1997**, *36*, 1520; (d) Plater, M. J.; Foreman, M. R. St.; Howie, R. A. *J. Chem. Crystal.* **1998**, *28*, 653; (e) Castro, I.; Calatayud, M. L.; Lloret, F.; Sletten, J.; Julve, M. *J. Chem. Soc., Dalton Trans.* **2002**, 2397; (f) Wang, C.-C.; Tseng, S.-M.; Lin, S.-Y.; Liu, F.-C.; Dai, S.-C.; Lee, G.-H.; Shih, W.-J.; Sheu, H.-H. *Cryst. Growth Des.* **2007**, *7*, 1783; (g) Abbati, G. L.; Cornia, A.; Babretti, A. C. *Acta Cryst. Sect. C* **1999**, *55*, 2043; (h) C.-C. Wang, C.-H. Yang, S.-M. Tseng, G.-H. Lee, Y.-P. Chiang, H.-S. Sheu, *Inorg. Chem.* 42 (2003) 8294; (i) Cornia, A.; Fabretti, A. C.; Giusti, A.; Ferraro, F.; Gatteschi, D. *Inorg. Chim. Acta* **1993**, *212*, 87; (l) Ghoshal, D.; Ghosh, A. K.; Ribas, J.; Mostafa, G.; Chaudhuri, N. R. *Cryst. Eng. Comm.* **2005**, *7*, 616; (m) Brouca-Cabarrecq, C.; Trombe J. C. *Inorg. Chim. Acta* **1992**, *191*, 227; (n) E. E. B. de Paula, L. C. Visentin, M. I. Yoshida, L. F. C. De Oliveira, F. C. Machado, Polyhedron 30 (2011) 213;

[19] (a) Wang, C.-C.; Kuo, C.-T.; Yang, J.-C.; Lee, G.-H.; Shih, W.-J.; Sheu, H.-S. *Cryst. Growth Des.* **2007**, *7*, 1476; (b) Gavilan, E.; Audebrand, N. *Polyhedron* **2007**, *26*, 5533; (c) Maji, T. K.; Konar, S.; Mostafa, G.; Zangrando, E.; Lu, T.-H.; Chaudhuri, N. R. *J. Chem. Soc., Dalton Trans*. **2003**, 171;

[20] C. J. Gómez-Garcia, E. Coronado, S. Curreli, C. Giménez-Saiz, P. Deplano, M. L. Mercuri, L. Pilia, A. Serpe, C. Faulmann, E. Canadell, *Chem. Comm.,* **2006**, 4931-4933

[21] J. Yamada, M. Watanabe, H. Anzai, H. Nishikawa, I. Ikemoto and K. Kikuchi *Angew. Chem. Int. Ed.,* **1999**, *38 (6)*, 810

[22] N. D. Kushch, A. V. Kazakova, L. I. Buravov, E. B. Yagubskii, S. V. Simonov, L. V. Zorina, S. S. Khasanov, R. P. Shibaeva, J. Yamada, M. Umemiyac, *Russian Chemical Bulletin, International Edition,* Vol. 59, **2010** 9, 1729—1734

[23] K. Kikuchi, H. Nishikawa, I. Ikemoto, T. Toita, H. Akutsu, S. Nakatsuji, J. Yamada, *Journal of Solid State Chemistry*, 2002, 168, 503–508

[24] I. Shevyakova, L. Buravov, V. Tkacheva, L. Zorina, S. Khasanov, S. Simonov, J. Yamada, E. Canadell, R. Shibaeva and E. Yagubskii, *Adv. Funct. Mat.,* **2004**, 14 (7), 660 – 668

[25] E.I. Zhilyaeva, A.M. Flakina, R.N. Lyubovskaya, I.V. Fedyanin, K.A. Lyssenko, M.Yu. Antipin, R.B. Lyubovskii, E.I. Yudanova , J. Yamadac, *Synthetic Metals* 156, **2006**, 991–998

[26] N.D. Kushch, A.V. Kazakova, L.I. Buravov, E.B. Yagubskii, S.V. Simonov, L.V. Zorina, S.S. Khasanov, R.P. Shibaeva, E. Canadell, H. Sond, J. Yamada, *Synthetic Metals*, 2005, 155, 588–594

[27] J. Yamada, H. Akutsu, *Chem. Rev.,* **2004,** 104, 5057-5083

[28] J. Yamada, *J Mater. Chem. ,* **2004**, 14 , 2951 – 2953

[29] F. Setifi, L. Ouahab, S. Golhen, O. Hernandez, A. Miyazaki, T. Enoki, T. Toita, J. Yamada, H. Nishikawa, A. Łapiński, R. Świetlik, *Inorg. Chem.,* **2002**, (41)*,* 3761-3768

[30] T. Mori, A. Kobayashi, Y. Sasaki, H. Kobayashi, G. Saito, and H. Inokuchi, *Bull. Chem. Soc. Jpn.* 1984, 57, 627.

[31] K. Kanoda, *J. Phys. Soc. Jpn.* 2006, *75*, 051007.

[32] E. Coronado, S. Curreli, C. Giménez-Saiz, C. J. Gómez-Garcia, and A. Alberola, *Inorg. Chem.* 2006, *45*, 10815.

[33] H. H. Wickman, M. P. Klein, and D. A. Shirley, *J. Chem. Phys.* 1965, *42*, 2113

[34] SHELXTL-PC Package. Bruker, AXS Inc., Madison, Wisconsin, USA, **1998**

CHAPTER 3

Multifunctional Material based on Single Molecule Magnet (Mn-salen Type) and Ni-Dithiolene Complexes

3.1 INTRODUCTION

In the field of molecular material science, the design of multifunctional materials, such as magnetic/conducting bifunctional materials, has been intensively studied. [1] A general method for designing such materials involves the hybridization of individual parts with magnetic and conducting frames via molecular self-assembly. Many compounds (paramagnet/superconductor, ferromagnet/superconductor, and ferromagnet/metal) have been prepared [2]-[4] (see Chapter 1) based on molecular conductors and classical magnets. Recent efforts have been addressed to investigate the correlation between relaxing local spins and conducting π electrons in superparamagnetic/conducting multifunctional materials from the viewpoint of developing quantum spintronics.
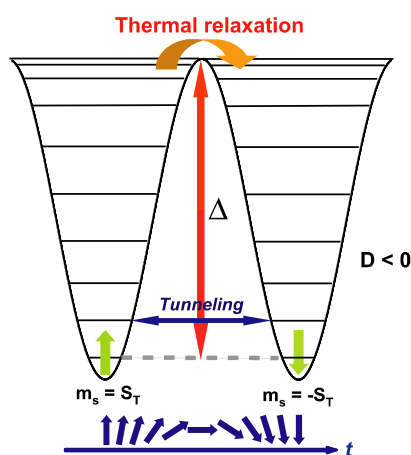
Figure 3.1: Schematic representation of SMM behavior

Single-molecule magnet (SMM) properties are attributed to intrinsic characteristics of the individual molecule, that is, high-spin ground state (S_T) and uniaxial anisotropy, which is indicated by a large negative D and a small E in relation to the following Hamiltonian anisotropy term: $H = DS_{Tz}^2 + E(S_{Tx}^{2-} - S_{Ty}^2)$. (Figure 3.1) The large D and small E values cause a finite energy barrier (Δ) between spin-up and spin-down m_s states ($m_s = \pm S_T$) expressed as $|D|S_T^2$

for integer values of S_T and $|D|(S_T^2 - 1/4)$ for half-integer values of S_T.

Therefore, SMMs exhibit slow relaxation of the magnetization and quantum phenomena, such as quantum tunneling of the magnetization (QTM) between quantum states of m_s, which can be tuned via Δ or decoherent energy levels of the quantum states. [5]-[11] Subjects of investigations are the correlations between relaxing local spins and conducting π electrons in superparamagnetic/conducting materials. [12]-[18]

Miyasaka et al. have suggested that SMMs can be used as magnetic building blocks to prepare molecular assemblies. [19] In developing their work on crystal engineering based on SMM or anisotropic molecule building blocks, their group has designed new classes of magnetic materials, including single-chain magnets (SCMs) and multidimensional SMM networks, which they call nanodot networks. [15] [16] [20] Recently, the first example of hybrid materials with both SMMs and molecular conducting layers has been reported. [21] This material involves a Coulomb pair of a cationic SMM, double-cuboidal mixed valence $[Mn_4]^{4+}$ clusters of $[Mn^{II}_2Mn^{III}_2(hmp)_6(ACN)_2(H_2O)_4](ClO_4)_4$ (hmp = 2-hydroxymetylpyridinate(-), ACN = acetonitrile), [22] and an anionic molecular conductor, (TBA)[Pt(mnt)$_2$] (mnt^{2-} = maleonitriledithiolate(2-)). (Chart 3.1) [23] Electrochemical oxidation of a solution containing both starting building blocks yielded a hybrid compound containing six [Pt(mnt)$_2$]$^{n-}$, where n = noninteger valence, per $[Mn_4]^{4+}$ SMM core, which behaves as an SMM/semiconductor. However, diffusion of the starting materials led simply to a counterion exchange reaction, affording an assembly with four [Pt(mnt)$_2$]$^-$ molecules per $[Mn_4]^{4+}$ SMM, which acts as a SMM/insulator.
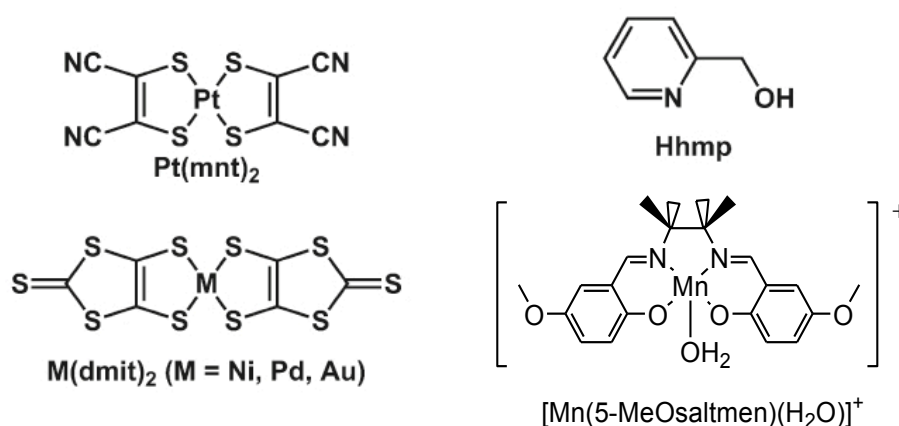

Chart 3.1

In order to improve the conduction properties [24] [25], another promising

strategy consists in preparing this kind of MMMs by using $[M(dmit)_2]^{n-}$ as conducting carrier because it has better electronic conductivity than $[Pt(mnt)_2]^{n-}$ due to a smaller HOMO-LUMO gap. [26] In fact, another class of SMM/semiconductor or insulator, $[Mn(5\text{-MeOsaltmen})(\text{solvent})]_2[Ni(dmit)_2]_7 \cdot$ 4(solvent) (solvent = acetone or ACN; $dmit^{2-}$ = 2-thioxo-1,3-dithiole-4,5-dithiolate) and $[Mn(5\text{-Rsaltmen})\{M(dmit)_2\}]_2$ (R=Me, MeO; M = Ni, Au), has been prepared. With the aim to tune the physical properties of these MMMs, a strategy is to change the ratio of the cation and anion. [27] A new MMMs, $[Mn(5\text{-MeOsaltmen})(\text{acetone})]_2[Ni(dmit)_2]_6$ **(3)**, has been synthesized and the crystal structure, electrical conductivity, magnetic susceptibility, infrared reflectance spectra and band calculations are here reported. [28] In addition, the peculiarity of the electronic state of **(1)** is discussed.

3.2 RESULTS AND DISCUSSION

3.2.1. Structural Features of $[Mn(5\text{-MeOsaltmen})(\text{acetone})]_2[Ni(dmit)_2]_6$ (3)

The structural features of **(3)** are reported in Figure 3.2. [28] The asymmetric unit includes one crystallographically independent $[Mn(5\text{-MeOsaltmen})(\text{acetone})]^+$ and three $[Ni(dmit)_2]$ molecules. There are inversion centers at the midpoint of the Mn $\cdots$ Mn vector of the cationic $[Mn(5\text{-MeOsaltmen}) - (\text{acetone})]_2^{2+}$ dimers. The dimer unit has a typical non-planar Mn(III) dimeric core and is structurally consistent with other reported $[Mn]_2$ SMMs. [34] The nickel ions in the anions have square planar coordination geometries similar to those of other d^8 metal ion complexes. Bond lengths and angles of $[Ni(dmit)_2]$ are in the same range found in other 1:3 radical anion salts of $[Ni(dmit)_2]$, reported in literature. [35]-[38] In this crystal, the cationic dimers and the anions form layers parallel to the *ab* plane. In the $[MnIII]_2^{2+}$ dimer layer, there is no significant interaction between the dimers through π-π contacts as observed in $[Mn(5\text{-MeOsaltmen})(\text{acetone})]_2[Ni(dmit)_2]_7 \cdot$ 4 acetone (Figure 3.2). [24] In the anionic layer, a one-dimensional columnar structure is formed by stacks of the three [Ni(dmit)2] molecules in the following arrangement, $\cdots$ [Ni(1)]-[Ni(2)]-[Ni(3)]-[Ni(3)]-[Ni(2)]-[Ni(1)] $\cdots$.
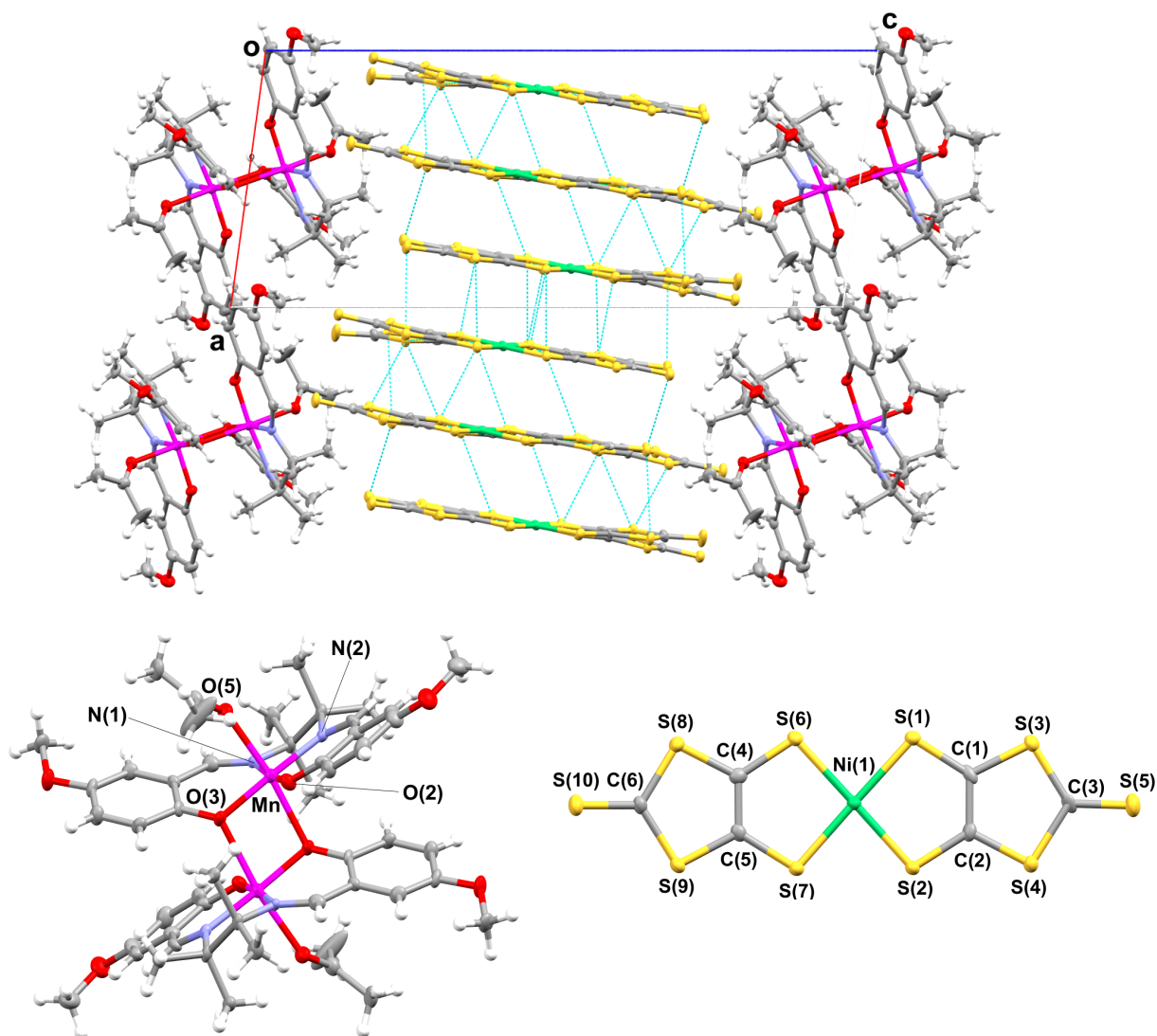
Figure 3.2: Structural features of **(3)**. Dashed lines indicate sulfur-sulfur contacts shorter than the sum of the van der Waals radii (3.7 Å) (*up*) and the labeling scheme for the two building blocks (*down*)

Intermolecular interactions through sulfur-sulfur contacts (3.546 - 3.679 Å) shorter than the sum of the van der Waals radii (3.7 Å) between the anionic molecules are present along the stacking direction and the *b* axis. In this salt, three [Ni(dmit)$_2$] asymmetric molecules have a total valence of -1. The electronic state of the [Ni(dmit)$_2$] moiety in **(3)**, which is either a uniform charged trimer state or a charge-ordered state, is discussed in Section 3.2.4, on the basis of IR reflectance spectra.

3.2.2. Electrical Resistivity

Electrical resistivity measurements for **(3)** have been performed from ambient pressure to 1.5 GPa. (Figure 3.3) At ambient pressure, **(3)** exhibits semiconducting behavior with a small activation energy (ϱ_{rt} = 2.1 · 10^{-1} Ω · cm^{-1}, E_a = 97 meV) and, although the activation energy slightly decreased at 1.7 GPa, **(3)** behabes as an insulator ($\varrho_{1.7\,GPa}$ = 4.5 Ω · cm^{-1}, E_a = 76 meV). The application of pressure controlled the electronic structure by changing the intermolecular interactions, as observed for other molecular conductors. [26]-[39] [41] The mechanism for this behavior depends on the origin of the insulating state at ambient pressure. The pressure experiments suggest that the band of the insulating state of **(3)** is 1/6 full. The character of the insulating state of **(3)** is further discussed on the basis of spectroscopic and magnetic studies. The resistivity curves can be classified into two groups and are discussed in Section 3.2.3.
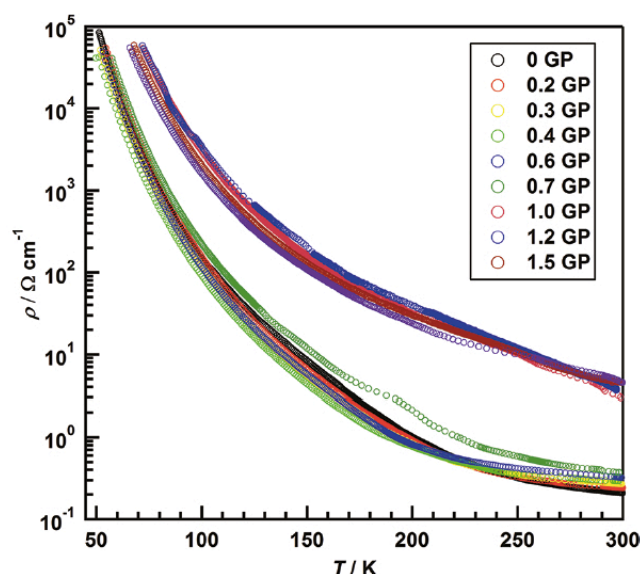
Figure 3.3: Temperature dependence of resistivity of **(1)** under applied pressure

3.2.3. Energy Band Calculation

The energy band structure of **(3)** was calculated using an extended Hückel MO tight-binding method with the structural data. Figure 3.4 shows the HOMO and LUMO for the anion moiety of **(3)**, peculiar for $M(dmit)_2$ complexes. The HOMO of the $M(dmit)_2$ molecule has b_{1u} symmetry, whereas the LUMO has b_{2g}

symmetry. The metal d orbital can mix with the LUMO but cannot with the HOMO due to the symmetry, destabilizing the HOMO and thus causing a small energy gap between the HOMO and LUMO. The side-by-side intermolecular interactions, which lead to the formation of a two-dimensional electronic structure, have a larger contribution from the HOMO than they do from the LUMO. This is because some of overlap integrals (S) for the intermolecular S ··· S pairs are canceled out due to the b_{2g} symmetry of the LUMO.
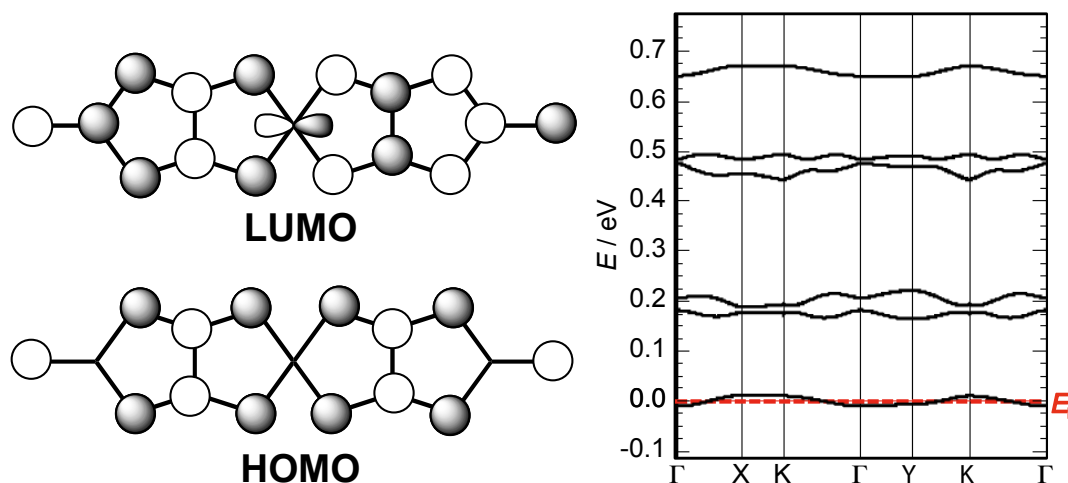
Figure 3.4: HOMO and LUMO of the neutral state of a [Ni(dmit)$_2$] molecule (left) and the energy band structure (right) for **(3)**.

The calculated S values between the LUMOs are listed in Table 3.1 with a schematic drawing of their arrangement in the anion moiety of **(3)**. On the basis of the LUMO, a quasi-onedimensional structure is formed because S values within the column (a1 - a4) are much larger than those involving the side-by-side interactions (b1 - b4 and p1 - p3). The calculated energy band structure formed from the LUMOs is shown in Figure 3.4 (right). There are 12 separated narrow bands from the LUMOs (see Table 3.1). Three of the [Ni(dmit)$_2$] molecules in the assembly have one electron, meaning that the band is 1/6 full (red bands in Figure 3.4 (right). The calculations indicate that **(3)** is a band insulator. Applying pressure on organic conductors mainly affects the bandwidth, W, and on-site coulomb repulsion, U. It appeared that there was a greater effect on U when pressure was applied during the resistivity measurements (Figure 3.3). The resistivity at room temperature rapidly increased when the pressure was greater than 0.7 GPa.

S ($\cdot 10^3$)		S ($\cdot 10^3$)		S ($\cdot 10^3$)	
a1	- 19.0	b1	0.2600	p1	- 0.44
a2	- 15.0	b2	0.2100	p2	1.10
a3	2.0	b3	0.3600	p3	- 0.91
a4	- 21.0	b4	-0.098		
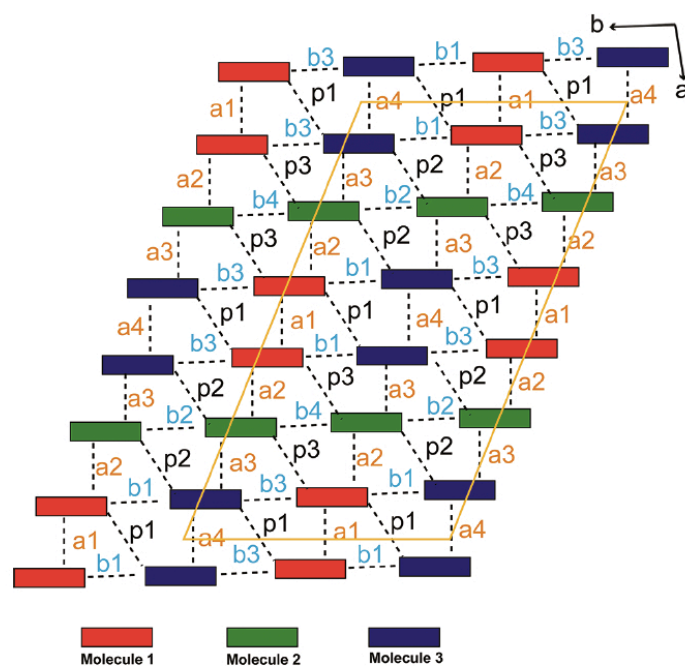
Table 3.1: Calculated Overlap Integrals (S 10^3) between the LUMOs of [Ni(dmit)$_2$] of **(3)**.

3.2.4. IR Spectrum

In order to investigate the electronic structure of **(3)**, polarized IR reflectance spectra has been performed. Figure 3.5 shows a polarized IR reflectance spectrum of **(3)** polarized along the *a* axis. The reflectance (R(ω)) spectrum for E||*a* had two distinct features: a broad maximum around 1800 cm^{-1} with an edge structure below 3000 cm^{-1} and a low-wavenumber portion below 1500 cm^{-1}, showing a few characteristic peaks. The broad maximum is not observed for E || *b* and E || *c*. These features indicate that **(3)** is a quasi-one-dimensional semiconductor. The mid-IR peak in the R(ω) spectrum mainly corresponds to an intermolecular charge transfer (CT) transition typically observed for various molecular conductors with quasi-one-dimensional character. [42] The two peaks observed at 1591 and 1690 cm cm^{-1} are attributed to ν(C=N) and ν(C=O)

of the cationic dimer [Mn(5-MeOsaltmen)(acetone)]$_2$$^{2+}$. Figure 3.5 (b) shows a magnification of the IR spectrum in the range of 750 - 1500 cm^{-1}. In this region, four peaks at 1386, 1356, 1327, and 1296 cm^{-1}, labeled ν1_rich, ν2_rich, ν1_poor, and ν2_poor, where ν1 and ν2 are the in-phase and out-of-phase C=C stretching modes of Ni(dmit)$_2$ and "rich" and "poor" denote charge-rich and -poor molecules, respectively, were observed. The four IR peaks are at positions similar to those for other 1:3 [Ni(dmit)$_2$] salts. [35]-[38] A broad maximum around 1150 cm^{-1} with dips corresponding to ν(C-S) (970 cm^{-1}) and ν(C=S) (1050 cm^{-1}) stretching modes is assigned to a C=C stretching mode. The broad maximum is attributed to an electron-molecular vibrational (e-mv) interaction due to coupling between the CT transition and a C=C stretching mode. The electronic state of [M(dmit)$_2$] (M = Ni, Pd) can be estimated from the peak position of the vibration modes of the molecule because these peaks and the maximum are sensitive to the charge. [43] On the basis of the assignment of the vibrational modes of neutral and reduced [Pd(dmit)$_2$] reported by Yamamoto et al., [44] the four peaks and the maximum in Figure 3.5 are assigned to a combination of the fundamental C=C stretching modes ν1 and ν2 of the six [Ni(dmit)$_2$] molecules in the symmetric unit of the crystal. Thus, considering the S in the *a* direction, as described in Section 3.2.3, the symmetric unit consists of a tetramer and a dimer: [-Molecule3'=Molecule3-Molecule2=Molecule1=Molecule1'=Molecule2'-Molecule3'=], where "=" and "-" represent large and small S in the *a*-direction, respectively. This symmetric unit consists of two equivalent trimmers ([=Molecule3-Molecule2=Molecule1=]) and one asymmetric trimer ([=Molecule1'=Molecule2'-Molecule3'=]).
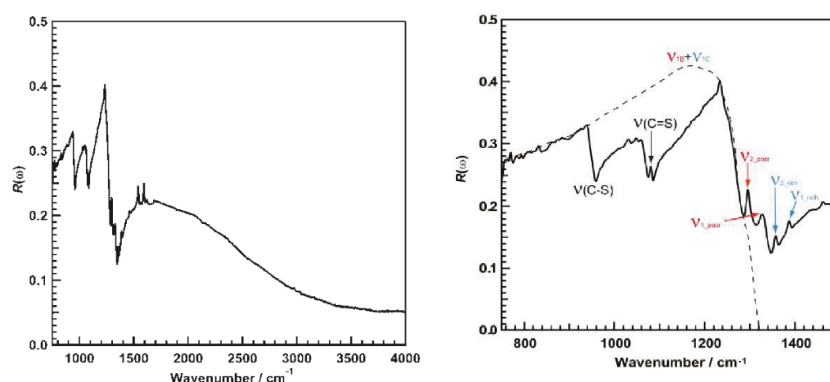

Figure 3.5: Polarized IR reflectance spectrum at 300K of **(3)** along the a axis in the 750-4000 cm^{-1} (left) and 750-1500 cm^{-1} (right) spectral range.

Combinations of in-phase and out-of-phase S's between two trimers cause three IR-active $v1$ and three Raman-active $v1$ modes. On the other hand, only two $v2$ modes belonging to the charge-poor and –rich molecules should be observed in the IR spectra because the asymmetric $v2$ mode is not involved in the e-mv interaction and is sensitive to the charge of the molecules. Therefore, there should be five C=C stretching modes. In other words, these experimental results are consistent with this argument. Interestingly, the separation in the frequency between $v1\_rich$ and $v1\_poor$ is similar to that between $v2\_rich$ and $v2\_poor$. This phenomenon indicates that the $v1\_rich$ and $v1\_poor$ modes are less perturbed by the e-mv interaction. In other words, they are charge localized. Thus, this spectrum strongly suggests that the electronic state of the anion moiety is a charge-ordered state. On the other hand, the line width of $v1C$ is significantly broad as compared to the corresponding mode in the anionic dimer (TBA)[Pd(dmit)$_2$]. [44] This observation suggests that a charge-rich molecule is sandwiched by charge-poor molecules, which favors large coupling with the CT transition. The charge on [Ni(dmit)$_2$] can be estimated from the IR spectrum, electrical resistivity, and energy band calculations. From the spectrum, the charge is [neutral]-[monoanion]-[neutral]. In other words, the neutral molecules are Molecule1 and Molecule3, and the anionic one is Molecule2. This charge ordering occurs through weak interactions between the anionic molecules. In the column, there are two neutral molecules, [Molecule1] and [Molecule3]. The side-by-side interactions between anionic [Molecule2] are very weak because transfer integrals b2 and b4 are 0.21 and -0.0098. The anions are arranged in quasi-one-dimensional $S = 1/2$ spin chains. The charge-ordered state is supported by the electrical resistivity measurements. Generally, molecular conductors in a charge-ordered state exhibit metallic or superconducting behavior under pressure because the charge-ordered state is broken by pressure. [45] In this case, however, the anionic molecules do not affect each other due to the arrangement of the molecules and the weak transfer integrals. DC magnetic susceptibility measurements also support this charge-ordered state (see next section).

3.2.5. Magnetic Susceptibility
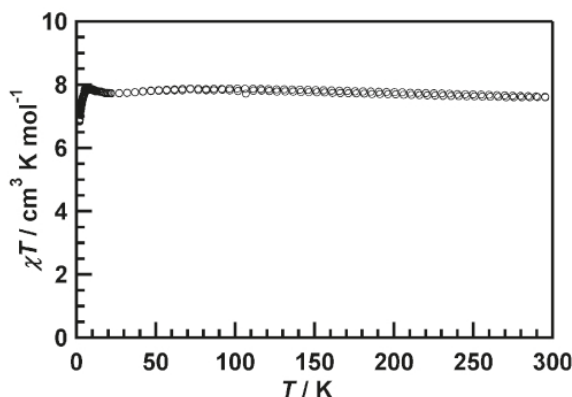
3.2.5.1. *dc Magnetic Susceptibility*

Figure 3.6: Temperature dependence of χT of **(3)** measured at 500 Oe.

The temperature dependence of DC magnetic susceptibility of a polycrystalline sample of **(3)** has been studied in a 500 Oe field in the temperature range of 1.8 - 300 K. Figure 3.6 shows a χT versus T plot of **(3)**. The value of χT slightly increased from 7.60 cm^3 · K 3 mol^{-1} at 300 K to 7.86 cm^3 · K 3 mol^{-1} at 70 K and then slightly decreased to 7.74 cm^3 · K 3 mol^{-1} at 20 K. Ferromagnetic interactions between manganese ions were observed around 8 K. This behavior is quite different from that of isolated [Mn$_2$]$^{2+}$ SMMs. The 2:7 salt [Mn(5-MeOsaltmen)(acetone)]$_2$-[Ni(dmit)$_2$]$_7$ · 4 acetone, which has a molecular packing similar to **(1)**, exhibits ferromagnetic behavior, which is typical of isolated [MnIII]$_2$$^{2+}$ SMMs. [24] The χT behavior of the 2:7 salt can be simulated using a Heisenberg dimer model with S = 2, taking into account zero field splitting (ZFS) of the Mn(III) ion (D$_{Mn}$) H = -2J$\hat{S}_{Mn1}\hat{S}_{Mn2}$ + 2D$_{Mn}$S$_{Mn,z}$^{2}, where S$_{Mn,z}$ is the *z* component of the S$_{Mn,i}$ spin vectors. In this case, however, the value of χT of **(3)** at 300 K is large compared to that of the Mn dimer only (~6.0 cm^3 · K · mol^{-1}). [46] We think that this is due to the contribution of the two Ni(dmit)$_2$ units with S = 1/2. The χT behavior of **(3)** can be understood by considering complicated interactions, such as the [Mn$_2$]$^{2+}$ ··· [Mn$_2$]$^{2+}$, [Ni]$^{n-}$ ··· [Ni]$^{n-}$, and [Mn$_2$]$^{2+}$ ··· [Ni]$^{n-}$. However, we could not accurately fit the magnetic data for **(3)**.

3.2.5.2. *ac Magnetic Susceptibilities*

The temperature dependence of the ac susceptibilities has been first measured in a 3 Oe ac field and zero dc field changing ac frequencies from **(3)** to 1500 Hz. However, both the in-phase (χ') and out-of-phase (χ'') components of the ac susceptibility of **(3)** were not frequency-dependent at T > 1.8 K. Thus, the measurement was carried out in a 500 Oe dc field. As shown in Figure 3.7, both χ' and χ'' are frequency-dependent at temperatures below 3 K, suggesting SMM behavior. However, distinct χ'' peaks are not observed above 1.8 K, even at an ac frequency of 1500 Hz. From the temperature dependence of the ac susceptibilities of **(3)** in a dc field of 500 Oe in the T range of 1.8 - 2.2 K, shown in Figure 3.8, an Arrhenius plot is plotted, as shown in Figure 3.9. The values of τ_0 and Δ_{eff}, which were estimated from a least-squares linear fit of $\tau(T) = \tau_0 \exp(\Delta_{eff}/k_B T)$, were $1.06 \cdot 10^{-6}$ s and 14.06 K, respectively. The value of τ_0 is smaller than those of general SMMs (10^{-7} to 10^{-8} s). However, a few examples of SMMs with slow relaxation times ($\sim 10^{-5}$ s) have been reported. [48] In other words, compound **(3)** can be regarded as a SMM.
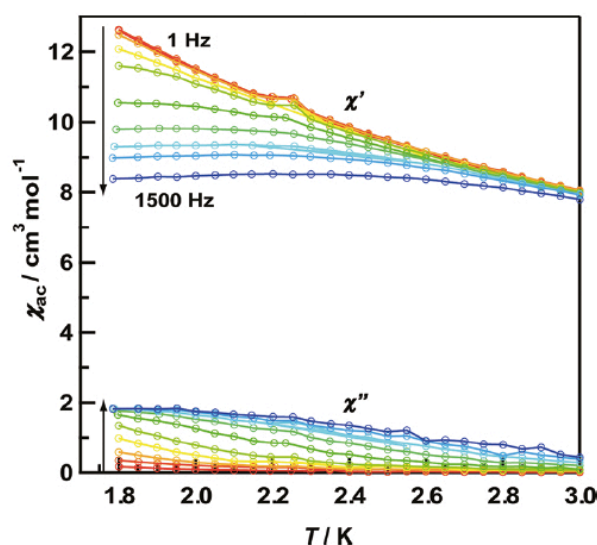
Figure 3.7: Temperature and frequency dependence of the real (χ') and imaginary (χ'') parts of the ac susceptibility for **(1)** in 3 Oe ac and 500 Oe dc fields (solid lines are only a guide for the eyes).
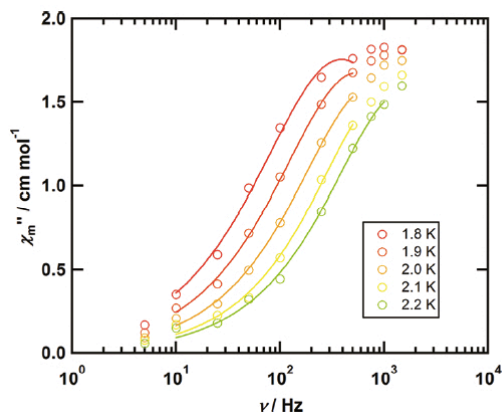
Figure 3.8: χ'' vs frequency for **(3)** in the T range of 1.8 - 2.2 K in a 500 Oe field. Solid lines indicate fitting lines
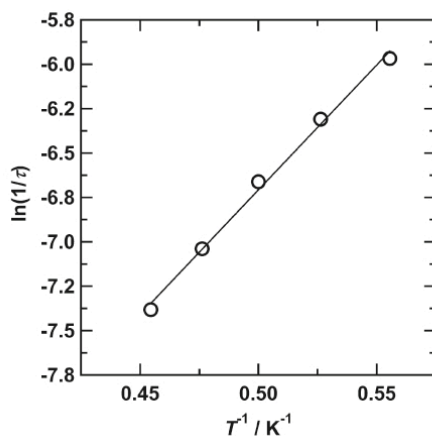
Figure 3.9: Arrhenius plot of the relaxation times for **(3)** estimated from the values of χ'' in a dc field of 500 Oe.

3.3. CONCLUSIONS

The electronic state of a structurally hybridized compound comprised of SMM and conducting layers, [Mn(5-MeOsaltmen)-(acetone)]$_2$[Ni(dmit)$_2$]$_6$, was described. SMM and semiconducting characters coexisted in crystals of **(3)**, although no correlations between them could be detected in the conduction and magnetic measurements. These results are similar to those for other hybrid materials, such as [Mn(5-MeOsaltmen)(solvent)]$_2$-[Ni(dmit)$_2$]$_7$ · 4solvent (solvent = acetone or acetonitrile). [24] However, **(3)** has a much different electronic state than the 2:7 salts. A charge-ordered state for **(3)** has been determined, which should lead to superconducting or metallic behavior in the conducting layers, although **(3)** behaved as a band insulator under pressure. Furthermore, the SMM behavior of **(3)** indicates that the SMM properties can be tuned by

changing the combination of SMMs and conducting molecules. Our results represent a new way to prepare hybrid materials based on quantum magnets and molecular conductors.

3.4. Experimental Section

3.4.1. Synthesis and Crystal Structure Determination of [Mn(5-MeOsaltmen)(acetone)]$_2$[Ni(dmit)$_2$]$_6$ (3)

Single crystals of (3) were prepared by electrochemical crystallization of an acetone solution of [Mn(5-MeOsaltmen)(H$_2$O)][PF$_6$] and (TBA)[Ni(dmit)$_2$], as previously reported. [28] [30] The chemical formula of the complex was determined on the basis of elemental and X-ray crystal structural analyses. Crystallographic data for (3): chemical formula, C$_{43}$H$_{32}$MnN$_2$Ni$_3$O$_5$S$_{30}$; crystal system, triclinic; space group, P1; a = 10.115(2) Å; b = 12.998(3) Å; c = 25.374(6) Å; a = 97.322(3)°, β = 97.076(3)°; γ = 98.119(3)°; Z = 2. [28]

3.4.2. Band Calculations

Intermolecular overlap integrals (S) between the frontier orbitals were determined by using extended Hückel molecular orbital (MO) calculations. The semiempirical parameters for the Slater-type atomic orbitals were taken from the literature. [31] Transfer integrals, t, were calculated by using the equation $t = -10S$.

3.4.3. Physical Measurements

Magnetic Measurements

The magnetic susceptibility of 1 (15.7 mg) was measured on a Quantum Design SQUID magnetometer (MPMS-XL) in the temperature and direct current (dc) field ranges of 1.8 - 300 K and -7 to +7 T, respectively. Alternating current (ac) susceptibilities were determined in the frequency range of 1_1488 Hz with an ac field amplitude of 3 Oe. A polycrystalline sample of (3) embedded in liquid paraffin was used for the measurements. Experimental data were corrected for

the sample holder, including the liquid paraffin, and for the diamagnetic contribution calculated from Pascal constants. [32]

Conductivity Measurements

The temperature dependence of the electrical resistivity of (**1**) was measured by using a standard four-probe method at ambient pressure. Gold wires (15 μm diameter) were attached to the crystal with carbon paste. High-pressure resistivity measurements on (**1**) were performed in the range of 0.2 - 1.7 GPa using a clamp-type piston-cylinder high-pressure cell. [33]

IR Reflectance Spectroscopy

Polarized reflectance spectra were acquired in the Spring-8 BL43IR beam line with a microscope. The spectral resolution was 4 cm^{-1}. The light polarization was set parallel (| | a) and perpendicular ($\perp$ b^*) to the stacking directions in the two-dimensional (2-D) sheets or almost parallel to the c axis, which is almost parallel to the long axis of [Ni(dmit)$_2$].

REFERENCES

[1] (a) Coronado, E.; Day, P. *Chem. Rev*. **2004**, 104, 5419–5448. (b) Enoki, T.; Miyazaki, A. *Chem. Rev.* **2004**, 104, 5449–5478. (c) Coronado, E.; Galán-Mascarós, *J. R. J. Mater. Chem.* **2005**, 15, 66–74. (d) Ouahab, L.
Chem. Mater. 1997, 9, 1909–1926.

[2] (a) Coronado, E.; Galán- Mascarós, J. R.; Gómez-Garcia, C. J.; Laukhin, V. *Nature* **2000**, 408, 447–449. (b) Alberola, A.; Coronado, E.; Galán- Mascarós, J. R.; Giménez-Saiz, C.; Gómez-Garcia, C. J. *J. Am. Chem. Soc*. **2003**, 125, 10774–10775.

[3] (a) Galán- Mascarós, J. R.; Coronado, E; Goddard, P. A.; Singleton, J.; Coldea, A. I.; Wallis, J. D.; Coles, S. J.; Alberola, A. *J. Am. Chem. Soc.* **2010**, 132, 9271–9273. (b) Coronado, E.; Martí-Gastaldo, C.; Navarro-Moratalla, E.; Ribera, A.; Blundell, S. J.; Baker, P. J. *Nat. Chem.* **2010**, 2, 1031–1036.

[4] (a) Ojima, E.; Fujiwara, H.; Kato, K.; Kobayashi, H.; Tanaka, H.; Kobayashi, A.; Tokumoto, M.; Cassoux, P. *J. Am. Chem. Soc.* **1999**, 121, 5581–5582. (b)

Kurmoo, M.; Graham, A. W.; Day, P.; Coles, S. J.; Hursthouse, M. B.; Caulfield, J. L.; Singleton, J.; Pratt, F. L.; Hayes, W.; Ducasse, L.; Guionneau, P. *J. Am. Chem. Soc.* **1995**, 117, 12209–12227.

[5] (a) Christou, G.; Gatteschi, D.; Hendrickson, D. N.; Sessoli, R. *MRS Bull.* **2000**, 25, 66–71. (b) Gatteshi, D.; Sessoli, R., *Angew. Chem., Int. Ed.* **2003**, 42, 268–297.

[6] (a) Boyd, P. D. W.; Li, Q.; Vincent, J. B.; Folting, K.; Chang, H.-R.; Streib, W. E.; Huffman, J. C.; Christou, G.; Hendrickson, D. N. *J. Am. Chem. Soc.* **1988**, 110, 8537–8539. (b) Caneschi, A.; Gatteschi, D.; Sessoli, R. *J. Am. Chem. Soc.* **1991**, 113, 5873–5874. (c) Sessoli, R.; Tsai, H.-L.; Schake, A. R.; Wang, S.; Vincent, J. B.; Folting, K.; Gatteschi, D.; Christou, G.; Hendrickson, D. N. *J. Am. Chem. Soc.* **1993**, 115, 1804–1816.

[7] (a) Aubin, S. M. J.; Wemple, M. W.; Adams, D. M.; Tsai, H.; Christou, G.; Hendrickson, D. N. *J. Am. Chem. Soc.* **1996**, 118, 7746–7754. (b) Yoo, J.; Brechin, E. K.; Yamaguchi, A.; Nakano, M.; Huffman, J. C.; Maniero, A. L.; Brunel, L.-C.; Awaga, K.; Ishimoto, H.; Christou, G.; Hendrickson, D. N. *Inorg. Chem.* **2000**, 39, 3615–3623. (c) Yoo, J.; Yamaguchi, A.; Nakano, M.; Krzystek, J.; Streib, W. E.; Brunel, L.-C.; Ishimoto, H.; Christou, G.; Hendrickson, D. N. *Inorg. Chem.* **2001**, 40, 4604–4616. (d) Hendrickson, D. N.; Christou, G.; Ishimoto, H.; Yoo, J.; Brechin, E. K.; Yamaguchi, A.; Rumberger, E. M.; Aubin, S. M. J.; Sun, Z.; Aromi, G. *Polyhedron* **2001**, 20, 1479–1488. (e) Boskovic, C.; Brechin, E. K.; Streib, W. E.; Folting, K.; Hendrickson, D. N.; Christou, G. *J. Am. Chem. Soc.* **2002**, 124, 3725–3736. (f) Brechin, E. K.; Boskovic, C.; Wernsdorfer, W.; Yoo, J.; Yamaguchi, A.; Sanudo, E. C.; Concolino, T.; Rheingold, A. L.; Ishimoto, H.; Hendrickson, D. N.; Christou, G. *J. Am. Chem. Soc.* **2002**, 124, 9710–9711. (g) Brechin, E. K.; Soler, M.; Davidson, J.; Hendrickson, D. N.; Parsons, S.; Christou, G. *Chem. Commun.* **2002**, 2252–2253.

[8] (a) Delfs, C.; Gatteschi, D.; Pardi, L.; Sessoli, R.; Wieghardt, K.; Hanke, D. *Inorg. Chem.* **1993**, 32, 3099–3103. (b) Barra, A. L.; Caneschi, A.; Cornia, A.; Fabrizi de Biani, F.; Gatteschi, D.; Sangregorio, C.; Sessoli, R.; Sorace, L. *J. Am. Chem. Soc.* **1999**, 121, 5302–5310. (c) Gatteschi, D.; Sessoli, R.; Cornia, A. *Chem. Commun.* **2000**, 725–732. (d) Oshio, H.; Hoshino, N.; Ito, T. *J. Am. Chem. Soc.* **2000**, 122, 12602–12603. (e) Benelli, C.; Cano, J.; Journaux, Y.; Sessoli, R.; Solan, G. A.; Winpenny, R. E. P. *Inorg. Chem.* **2001**, 40, 188–189. (f) Goodwin,

J. C.; Sessoli, R.; Gatteschi, D.; Wernsdorfer, W.; Powell, A. K.; Heath, S. L. *J. Chem. Soc., Dalton Trans.* **2000**, 1835–1840.

[9] (a) Cadiou, C.; Murrie, M.; Paulsen, C.; Villar, V.; Wernsdorfer, W.; Winpenny, R. E. P. *Chem. Commun.* **2001**, 2666–2667. (b) Andres, H.; Basler, R.; Blake, A. J.; Cadiou, C.; Chaboussant, G.; Grant, C. M.; Güdel, H.-U.; Murrie, M.; Parsons, S.; Paulscn, C.; Semadini, F.; Villar, V.; Wernsdorfer, W.; Winpenny, R. E. P. *Chem. Eur. J.* **2002**, 8, 4867–4876. (c) Yang, E.-C.; Wernsdorfer, W.; Hill, S.; Edwards, R. S.; Nakano, M.; Maccagnano, S.; Zakharov, L. N.; Rheingold, A. L.; Christou, G.; Hendrickson, D. N. *Polyhedron* **2003**, 22, 1727–1733.

[10] Castro, S. L.; Sun, Z.; Grant, C.M.; Bollinger, J. C.; Hendrickson, D. N.; Christou, G. *J. Am. Chem. Soc.* **1998**, 120, 2365–2375.

[11] Yang, E.; Hendrickson, D. N.; Wernsdorfer, W.; Nakano, M.; Zakharov, L. N.; Sommer, R. D.; Rheingold, A. L.; Ledezma-Gairaud, M.; Christou, G. *J. Appl. Phys.* **2002**, 91, 7382–7388.

[12] (a) Wernsdorfer, W.; Aliaga-Alcalde, N.; Hendrickson, D. N.; Christou, G. *Nature* **2002**, 416, 406–409. (b) Tiron, R.; Wernsdorfer, W.; Foguet-Albiol, D.; Aliaga-Alcalde, N.; Christou, G. *Phys. Rev. Lett.* **2003**, 91, 227203–1_227203_4. (c) Hill, S.; Edwards, R. S.; Aliaga- Alcalde, N.; Christou, G. *Science* **2003**, 302, 1015–1018. (d) Park, K.; Pederson, M. R.; Richardson, S. L.; Aliaga-Alcalde, N.; Christou, G. *Phys. Rev. B* **2003**, 68, 020405-1–020405-4. (e) Wernsdorfer, W.; Bhaduri, S.; Tiron, R.; Hendrickson, D. N.; Christou, G. *Phys. Rev. Lett.* **2002**, 89, 197201–1_197201_4. (f) Edwards, R. S.; Hill, S.; Bhaduri, S.; Aliaga-Alcalde, N.; Bolin, E.; Maccagnano, S.; Christou, G.; Hendrickson, D. N. *Polyhedron* **2003**, 22, 1911–1916.

[13] Tiron, R.; Wernsdorfer, W.; Aliaga-Alcalde, N.; Christou, G. *Phys. Rev. B* **2003**, 68, 140407–1 – 140407-4.

[14] Boskovic, C.; Bircher, R.; Tregenna-Piggott, P. L. W.; Güdel, H. U.; Paulsen, C.; Wernsdorfer, W.; Barra, A.-L.; Khatsko, E.; Neels, A.; Stoeckli-Evans, H. *J. Am. Chem. Soc.* **2003**, 125, 14046–14058.

[15] Miyasaka, H.; Nakata, K.; Sugiura, K.; Yamashita, M.; Clérac, R. *Angew. Chem., Int. Ed.* **2004**, 43, 707–711.

[16] Miyasaka, H.; Nakata, K.; Lecren, L.; Coulon, C.; Nakazawa, Y.; Fujisaki, T.; Sugiura, K.; Yamashita, M.; Clérac, R. *J. Am. Chem. Soc.* **2006**, 128, 3770–3783.

[17] Lecren, L.; Roubeau, O.; Coulon, C.; Li, Y.-G.; Le Goff, X. F.; Wernsdorfer,

W.; Miyasaka, H.; Clérac, R. *J. Am. Chem. Soc.* **2005**, 127, 17353–17363.

[18] Lecren, L.; Wernsdorfer, W.; Li, Y.-G.; Vindigni, A.; Miyasaka, H.; Clérac, R. *J. Am. Chem. Soc.* **2007**, 129, 5045–5051.

[19] Miyasaka, H.; Yamashita, M. *Dalton Trans.* **2007**, 399–406.

[20] (a) Clérac, R.; Miyasaka, H.; Yamashita, M.; Coulon, C. *J. Am. Chem. Soc.* **2002**, 124, 12837–12844. (b) Miyasaka, H.; Clérac, R.; Mizushima, K.; Sugiura, K.; Yamashita, M.; Wernsdorfer, W.; Coulon, C. *Inorg. Chem.* **2003**, 42, 8203–8213. (c) Ferbinteanu, M.; Miyasaka, H.; Wernsdorfer, W.; Nakata, K.; Sugiura, K.; Yamashita, M.; Coulon, C.; Clérac, R. *J. Am. Chem. Soc.* **2005**, 127, 3090–3099. (d) Lecren, L.; Roubeau, O.; Coulon, C.; Li, Y.-G.; Le Goff, X. F.; Wernsdorfer, W.; Miyasaka, H.; Clérac, R. *J. Am. Chem. Soc.* **2005**, 127, 17353–17363. (e) Miyasaka, H.; Madanbashi, T.; Sugimoto, K.; Nakazawa, Y.; Wernsdorfer, W.; Sugiura, K.; Yamashita, M.; Coulon, C.; Clérac, R. *Chem. Eur. J.* **2006**, 12, 7028–7040. (f) Saitoh, A.; Miyasaka, H.; Yamashita, M.; Clérac, R. *J. Mater. Chem.* **2007**, 17, 2002–2012. (g) Lecren, L.; Roubeau, O.; Li, Y.-G.; Le Goff, X. F.; Miyasaka, H.; Richard, F.; Wernsdorfer, W.; Coulon, C.; Clérac, R. *Dalton Trans.* **2008**, 755–766.

[21] Hiraga, H.; Miyasaka, H.; Nakata, K.; Kajiwara, T.; Takaishi, S.; Oshima, Y.; Nojiri, H.; Yamashita, M. *Inorg. Chem.* **2007**, 46, 9661–9671.

[22] Lecren, L.; Li, Y.-G.; Wernsdorfer, W.; Roubeau, O.; Miyasaka, H.; Clérac, R. *Inorg. Chem. Commun.* **2005**, 8, 626–630.

[23] (a) Davison, A.; Edelstein, N.; Holm, R. H.; Maki, A. H. *Inorg. Chem.* **1963**, 2, 1227. (b) Underhill, A. E.; Ahmad, M. M. *J. Chem. Soc., Chem. Commun.* **1981**, 67–68.

[24] Hiraga, H.; Miyasaka, H.; Takaishi, S.; Kajiwara, T.; Yamashita, M. *Inorg. Chim. Acta* **2008**, 361, 3863–3872.

[25] Hiraga, H.; Miyasaka, H.; Clérac, R.; Fourmigué, M.; Yamashita, M. *Inorg. Chem.* **2009**, 48, 2887–2898.

[26] Kato, R. *Chem. Rev.* **2004**, 104, 5319–5346.

[27] (a) Shibaeva, R. P.; Yagubskii, E. B. *Chem. Rev.* **2004**, 104, 5347–5378. (b) Kobayashi, H.; Cui, H.-B.; Kobayashi, A. *Chem. Rev.* **2004**, 104, 5265–5288.

[28] (a) K. Kubo, T. Shiga, T. Yamamoto, A. Tajima, T. Moriwaki, Y. Ikemoto, M. Yamashita, E. Sessini, M. L. Mercuri, P. Deplano, Y. Nakazawa, R. Kato, *Inorganic Chemistry*, **2011**, 50 (19), 9337-9344; (b) Kubo, K.; Miyasaka, H.; Yamashita, M. Phys. B, *Condens. Matter* **2010**, 405, S313–S316.

[29] Miyasaka, H.; Cl_erac, R.; Ishii, T.; Chang, H.-C.; Kitagawa, S.; Yamashita, M. *J. Chem. Soc., Dalton Trans*. **2002**, 1528–1534.

[30] Steimeche, G.; Sieler, H. J.; Kirmse, R.; Hoyer, E. Phosphor. *Sulfur* **1979**, 7, 49–55.

[31] (a) Albright, T. A.; Hofmann, P.; Hoffmann, R. *J. Am. Chem. Soc.* **1977**, 99, 7546–7557. (b) Joergensen, K. A.; Wheeler, R. A.; Hoffmann, R. *J. Am. Chem. Soc.* **1987**, 109, 3240–3246. (c) Keszler, D. A.; Hoffmann, R. *J. Am. Chem. Soc.* **1987**, 109, 118–124.

[32] Boudreux, E. A.; Mulay, L. N. *Theory and Application of Molecular Paramagnetism*; John Wiley and Sons: New York, **1976**; p 491.

[33] (a) Walker, I. R. *Rev. Sci. Instrum.* **1999**, 70, 3402–3412. (b) Ishii, Y.; Tamura, M.; Kato, R.; Hedo, M.; Uwatoko, Y.; Môri, N. *Synth. Met.* **2005**, 152, 389–393.

[34] Miyasaka,H.; Clérac, R.;Wernsdorfer, W.; Lecren,L.; Bonhomme, C.; Sugiura,K.-I.; Yamashita, M. *Angew. Chem., Int. Ed.* **2004**, 43, 2801–2805.

[35] Faulmann, C.; Delpech, F.; Malfant, I.; Cassoux, P. *J. Chem. Soc., Dalton Trans.* **1996**, 2261–2267.

[36] Valade, L.; Legros, J.-P.; Bousseau, M.; Cassoux, P.; Garbauskas, M.; Interrante, L. V. *J. Chem. Soc., Dalton Trans.* **1985**, 783–794.

[37] Nakamura, T.; Underhill, A. E.; Coomber, A. T.; Friend, R. H.; Tajima, H.; Kobayashi, A.; Kobayashi, H. *Inorg. Chem.* **1995**, 34, 870–876.

[38] Johannsen, I.; Bechgaard, K.; Rindorf, G.; Thorup, N.; Jacobsen, C. S.; Mortensen, K. *Synth. Met.* **1986**, 15, 333–343.

[39] (a) Jérome, D.; Mazaud, A.; Ribault, M.; Bechgaard, K. *J. Phys., Lett.* **1980**, 41, 95–98. (b) Creuzet, F.; Jérome, D.; Moradpour, A. *Mol. Cryst. Liq. Cryst.* **1985**, 119, 297–302. (c) Jérome, D. *Science* **1991**, 252, 1509–1514.

[40] (a) Taniguchi, H.; Miyashita, M.; Uchiyama, K.; Satoh, K.; Môri, N.; Okamoto, H.; Miyagawa, K.; Kanoda, K.; Hedo, M.; Uwatoko, Y. *J. Phys. Soc. Jpn.* **2003**, 72, 468–471. (b) Kini, A. M.; Geiser, U.; Wang, H. H.; Carlson, K. D.; Williams, J. M.; Kwok, W. K.; Vandervoort, K. G.; Thompson, J. E.; Stupka, D. L.; Jung, D.; Whangbo, M.-H. *Inorg. Chem.* **1990**, 29, 2555–2557. (c) Williams, J. M.; Kini, A. M.; Wang, H. H.; Carlson, K. D.; Geiser, U.; Montgomery, L. K.; Pyrka, G. J.; Watkins, D. M.; Kommers, J. M.; Boryschuk, S. J.; Crouch, A. V. S.; Kwok, W. K.; Schirber, J. E.; Overmyer, D. L.; Jung, D.; Whangbo, M.-H. *Inorg. Chem.* **1990**, 29, 3272–3274.

[41] (a) Brossard, L.; Ribault, M.; Valade, L.; Cassoux, P. *Phys. B+C* **1986**, 143,

313–315. (b) Bousseau, M.; Valade, L.; Legros, J.-P.; Cassoux, P.; Carbauskas, M.; Interrante, L. V. *J. Am. Chem. Soc.* **1986**, 108, 1908–1916.

[42] (a) Tajima, H.; Yakushi, K.; Kuroda, H.; Saito, G. *Solid State Commun.* **1985**, 56, 159–163. (b) Jacobsen, C. S.; Tanner, D. B.; Williams, J. M.; Geiser, U.; Wang, H. H. *Phys. Rev. B* **1987**, 35, 9605–9613.

[43] (a) Pokhodnya, K. I.; Cassoux, P.; Feltre, L.; Meneghtti, M. *Synth. Met.* **1999**, 103, 2187. (b) Romaniello, P.; Lelj, F.; Arca, M.; Devillanova, F. A. *Theor. Chem. Acc.* **2007**, 117, 621–635.

[44] Yamamoto, T.; Nakazawa, Y.; Tamura, M.; Fukunaga, T.; Kato, R.; Yakushi, K. *Phys J. Phys. Soc. Jpn.* **2011**, 80, 074717_1–074717_16.

[45] Miyagawa, K.; Kanoda, K.; Kawamoto, A. *Chem. Rev.* **2004**, 104, 5635–5654.

[46] Thomas, L.; Lionti, F.; Ballou, R.; Gatteschi, D.; Sessoli, R.; Barbara, B. *Nature* **1996**, 383, 145–147.

[47] (a) Ako, A. M.; Mereacre, V.; Hewitt, I. J.; Cl_erac, R.; Lecren, L.; Anson, C. E.; Powell, A. K. *J. Mater. Chem.* **2006**, 16, 2579–2586. (b) Kachi-Terajima, C.; Miyasaka, H.; Saitoh, A.; Shirakawa, N.; Yamashita, M.; Clérac, R. *Inorg. Chem.* **2007**, 46, 5861–5872.

[48] (a) Ishikawa, N.; Sugita, M.; Ishikawa, T.; Koshihara, S.; Kaizu, Y. *J. Am. Chem. Soc.* **2003**, 125, 8694–8695. (b) Boskovic, C.; Bircher, R.; Tregenna-Piggott, P. L. W.; Güdel, H. U.; Paulsen, C.; Wernsdorfer, W.; Barra, A.-L.; Khatsko, E.; Neels, A.; Stoeckli-Evans, H. *J. Am. Chem. Soc.* **2003**, 125, 14046–14058. (c) Gatteschi, D.; Sessoli, R.; Cornia, A. *Chem. Commun.* **2000**, 725–732.

II

PROCESSING OF MULTIFUNCTIONAL MATERIALS[*]

CHAPTER 4

Conducting Organic Polymers (PEDOT)

In the second part of this thesis, a study on processing methods based on the insertion of magnetic carriers into Conducting Organic Polymers (COPs) to obtain multifunctional materials as thin film is reported. The investigation of the influence of factors such as the doping method and the nature of the counterion in the physical properties of materials is pointed out.

4.1 CONDUCTING ORGANIC POLYMERS

Conductivity in organic conjugated polymers has been first measured in 1977 by H. Shirakawa, A. G. McDiarmid and A. J. Hegger who found a high value of conductivity (10^5 S/cm) in halogen-doped polyactylene. [1] Since then, many other conducting polymers have been studied and some examples are reported in Chart 4.1.
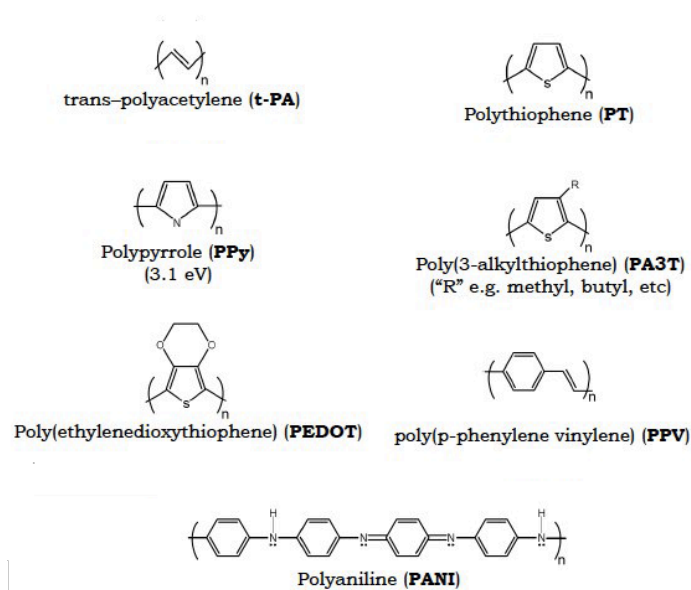

Chart 4.1: some of the most commonly used conjugated conducting polymers

A close look to the COPs reported in chart p.1, highlights that all of them are conjugated polymers, i.e. their backbones consist of alkyl chains with conjugated double bonds.

Depending on the C-based backbone arrangement, it is possible to tune properties as solubility, charge density and electronic properties of the conducting polymer. One of the goals of this research field is to find a cheap way for obtaining conducting polymers with desired shape and chemical and physical features.

Considering polyacetylene as a prototype conducting polymer, a schematic representation of the conjugated backbone can be drawn, as shown in Figure 4.1.
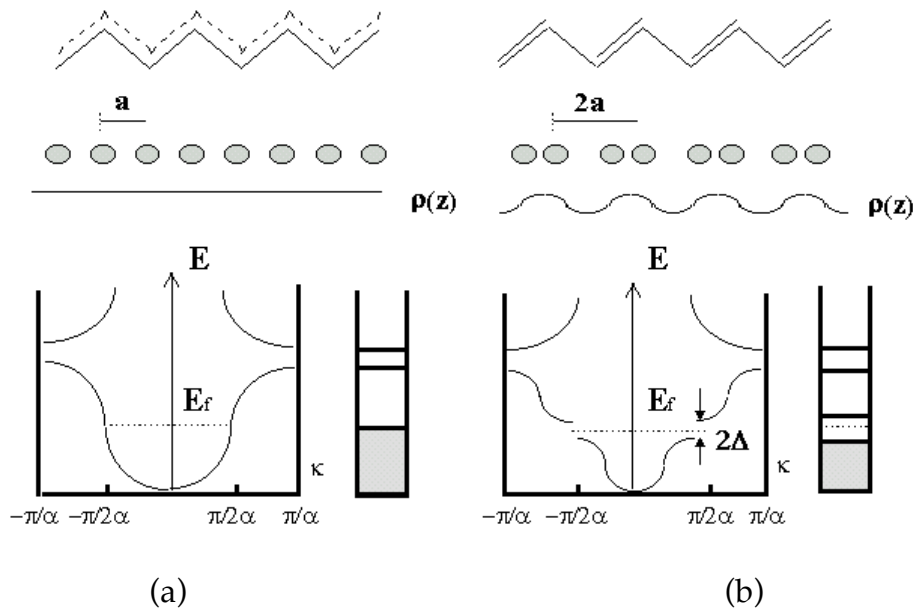

Figure 4.1: schematic representation of the polyacetylene backbone (a) and under the Peierls distortion effect (b); $\rho(z)$ is the electronic density and **a** the lattice period.

Each carbon atom is hybridized sp^2 and brings one delocalized π-electron. This leads to the formation of a one dimensional (1D) chain along which π delocalization occurs. However, since this is not a stable configuration, a lattice distortion will take place leading to a rearrangement of the energy levels inducing charge localization and semiconductor behavior. [1][2]

Enhancement of conductivity is possible by polymer doping process. A dopant is a species (neutral or ionic) able to remove (oxidize) (p-doping) or to inject (reduce) electrons (n-doping) from/into the polymer π-backbone. The doping process increases conductivity because a) the injection or removal of electrons leads to an increase of the charge density; b) the electrostatic interaction between the partially charged repeating unit and the nuclei of the nearby units

will occur permitting charge delocalization through the polymer chain. (Scheme 4.1) [3] [4]
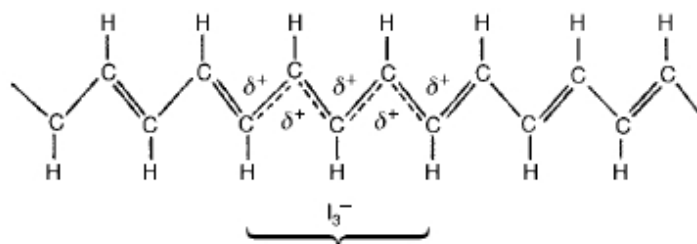
Scheme 4.1: charge delocalization occurring in the polyacetylene backbone after I_2 doping process.

Doping may be done following the methods listed below:

- Chemical doping: a chemical reaction occurs when the polymer is put in contact with a n – or p – type dopant that is inserted into the polymer as counterion;

- Electrochemical doping: by applying a potential, a reduction or oxidation of the polymer backbone occurs, and a charge-balancing ion enters the polymer matrix from the solution;

- Photo-doping: light irradiation promotes local π electrons to the excited state forming electron-hole pairs (excitons) that can migrate throughout the conjugated polymer chain. This kind of conductivity drops as excitons decay to the ground state leading to charge recombination. Photo-doping is the only non-redox process that simply involves the rearrangement of the energy levels without counterion insertion. [5]

In redox doping, the counterion is not covalently bonded to the polymer backbone as usually occurs for conventional semiconductors. In fact, the dopant atomic or molecular ion is positioned in the interstitial space between conjugated polymer chains.

As the doping counterion is a carrier of magnetism, then a multifunctional material can be obtained. Both the nature of the counterion and the synthetic route may influence the physical properties of the obtained material.

The main limitation to conductivity in doped organic polymers arises from disorder because it leads to charge localization. To overcome this drawback, efforts are recently aimed at enhancing the order into the polymer. The first promising result in this direction has been obtained by Schön et al. [6] who

found superconductivity in polymer film of regioregular poly(3-hexylthiophene) for temperature values below ~ 2.35 K. This result demonstrates that in these materials conductivity is strictly dependent on the order grade and encourages further efforts in this research field to prepare even more ordered polymeric systems.

4.2 PEDOT

Polythiophenes are an important class of polymers suitable to be used in optoelectronic devices such as LEDs thanks to their almost transparent color and high conductivity. [7] However, their relative instability under air and humidity exposure, a short life of the doped state and insolubility in a large number of solvents have for long hampered their use. [4] [8]

In order to overcome these drawbacks, a large number of polythiophenes have been synthetized. Among them, poly(3,4-ethylenedioxythiophene) (PEDOT) exhibits the most promising features, showing high stability in air and under high temperatures.

PEDOT is synthesized by polymerization of the monomeric unit 3,4-ethylenedioxythiophene (EDOT). Some of its chemical and physical features are summarized in Table 4.1. [4] [9]
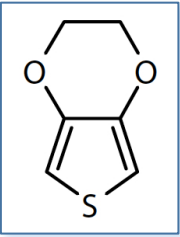
Synonyms / Abbreviations	EDT, EDOT	
Chemical Formula	3,4-ethylenedioxythiophene	
Physical Characteristics		
	Viscosity	11 mPa
Technical Data	Form	liquid
	Odor	unpleasant
	Color	colorless
	Density	1.34 g$/$cm^3 at 20°C
	Boiling Point	225°C

Table 4.1: Physical and chemical parameters for EDOT

The principal chemical feature of EDOT is that it is extremely sensitive to oxidation and then unstable in air. Anyway, chemical oxidation of EDOT allows easy polymerization using oxidative agents as protons, Lewis acids and several metal ions. Among them, the most commonly used are the inorganic complexes of Fe^{III} such as $FeCl_3$. As an example, the synthesis of PEDOT doped with $FeCl_4^-$ is reported in Scheme 4.2.
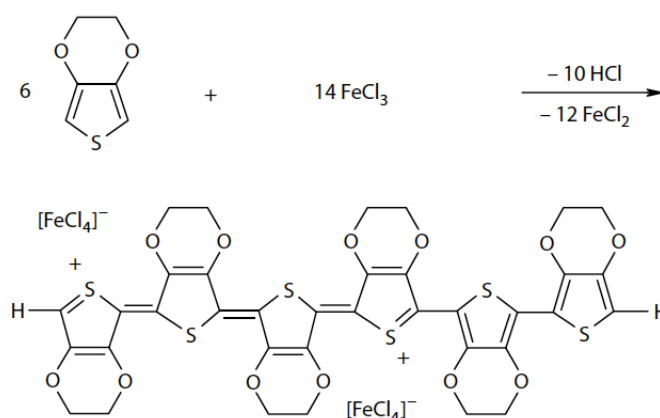
Scheme 4.2: acid catalyzed synthesis of PEDOT doped with $FeCl_4^-$ ions

The obtained doped PEDOT shows higher conductivity with respect to all the other known polyheterocycles: PEDOT – $FeCl_4^-$ shows a conductivity of ca. 15 S/cm while polypyrrole – $FeCl_4^-$ synthesized under the same conditions has a conductivity of ca. $5 \cdot 10^{-3}$ S/cm. [4][10] Despite its high conductivity, doped PEDOT shows two main drawbacks, i.e. difficult control of the quick chemical oxidation and insolubility into the more common solvents.

With the aim to control as much as possible the oxidation reaction, the electrochemical method has offered the possibility to tune the oxidation condition by modulation of the applied potential. In addition, this method limits the counterion insertion only to its solubility and stability under the reaction conditions.

4.2.2 PEDOT:PSS

In order to improve the solubility of PEDOT and then its processability, intense efforts have been done for obtaining a doped PEDOT solution.

The most successful result has been obtained by doping EDOT with a polyacid such as the polystyrene sulfonic acid (PSS) bearing acidic sulfonato groups that allows polymer solubility in aqueous solution. [10]
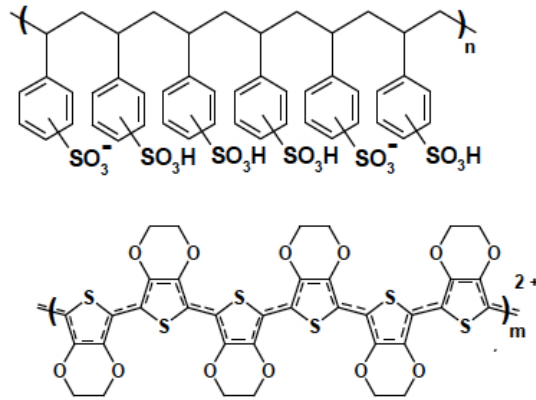

Figure 4.2: PSS (up) and PEDOT chains in PEDOT:PSS dispersion.

The *in situ* polymerization of EDOT in the presence of polystyrene sulfonic acid and a small amount of Fe^{III} ions as catalyst leads to the formation of a water stable dispersion of PEDOT:PSS (poly-3,4-ethylenedioxythiophene : polystyrenesulfonic acid) that is one of the best results in the field of COPs, (Figure 4.2) being the only commercialized example of highly conductive polythiophene. [12]

This dispersion consists of PEDOT:PSS grains in which PSS chains are entangled with PEDOT segments. (Figure 4.3) The hydrophilic sulfonic groups of PSS concentrate mostly in the outside shell of the grains. In addition, the charged surface of these micrometric particles avoids coagulation. [13]

Due to the presence of sulfonato groups, pH control is also fundamental for tuning the conducting properties of the polymer, and it has been demonstrated that the highest conductivity values are reached in the $0 - 3$ pH range. [4] [14]
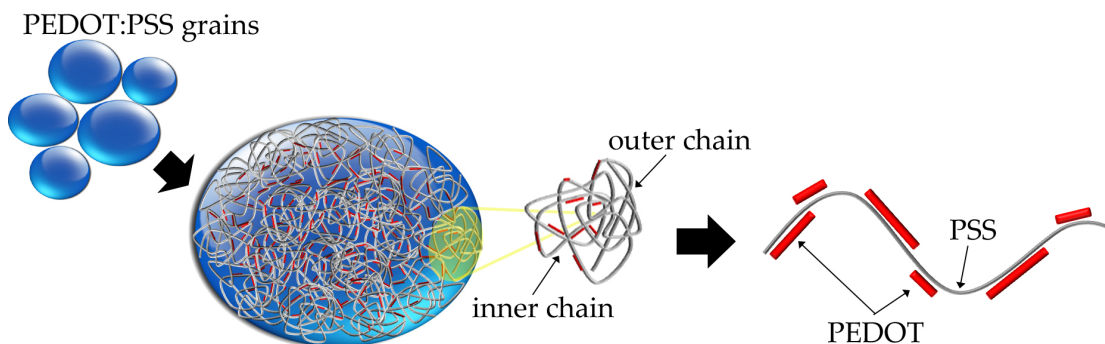

Figure 4.3: schematic representation for a grain of PEDOT:PSS dispersion.

Depending of the ratio between PEDOT and PSS weights, different kinds of dispersions can be obtained. PH500™ has been selected in this work because of its high conductivity, and its chemical/physical parameters are summarized in Table 4.2.

Synonyms / Abbreviations	PEDT / PSS, PEDOT / PSS	
Chemical Formula	Poly(3,4-ethylenedioxythiophene)-poly(styrenesulfonate)	
Description of Product	Aqueous dispersion, blue liquid	
Physical Characteristics		
	Solid content	1.0 – 1.3 %
	Specific conductivity[*]	300 S/cm
	Viscosity	8 – 25 mPa
	Particle Size Distribution d50	50 nm
Technical Data	Form	liquid
	Odor	odorless
	Color	dark blue
	PEDOT:PSS ratio	1:2.5 (by weight)
	pH	1.5 – 2.5 at 20°C
	Density	1 g/cm^3 at 20°C
	Boiling Point	approx 100°C

Table 4.2: Physical and chemical parameters for *CLEVIOS*™ **PH 500**

Due to its the easy processability from aqueous solution, PEDOT:PSS can be processed as thin, light blue, transparent and homogeneous films by using common deposition techniques as spin coating, drop casting, … In addition, structured deposition as screen printing, inkjet and various forms of contact printing are commonly employed to process this material. [15] Other ways for structured deposition of PEDOT:PSS have been realized by modifying the wetting properties of the surface, that is by depositing water repellants [16] or by using photo-lithographical techniques. [17] [18]

REFERENCES

[1] H. Shirakawa, E. J. Louis, A. G. MacDiarmid, C. K. Chiang, A. Heeger, *J.C.S. Chem. Comm.*, 1977, 578-580

---

[*] *After the addition of 5% Dimethyl sulfoxide. Measured on the dried coating.

[2] R. E. Peierls, *Quantum Theory of Solids*, Oxford University Press, Oxford, **1955**

[3] A. J. Heeger, *Angew. Chem. Int. Ed.*, **2001**, (40), 2591-2611

[4] A. Elschner, S. Kirchmeyer, W. Lövenich, U. Merker, K. Reuter *Principles and Applications of an Intrinsically Conductive Polymer*, **2011**, CRC Press, Taylor and Francis Group, LLC

[5] (a) J. C. Chiang, A. G. MacDiarmid, *Synth. Met.* **1986**, 13, 193; (b) A. G. MacDiarmid, J.-C. Chiang, A. F. Richter, A. J. Epstein, *Synth. Met.* **1987**, 18, 285.; (c) A. G. MacDiarmid, A. J. Epstein, *Faraday Discuss. Chem. Soc.* **1989**, 88, 317, and refs therein; (d) A. G. MacDiarmid, A. J. Epstein in *Science and Applications of Conducting Polymers*, Eds.:W. R. Salaneck, D. T. Clark, E. J. Samuelsen, Adam Hilger, Bristol, **1990**, p. 117

[6] J. H. Schön, A. Dodabalapur, Z. Bao, Ch. Kloc, O. Schenker, B. Batlogg, *Nature*, **2001**, (410), 189-191

[7] (a) N. C. Billingham and P. D. Calvert., *Adv Polym Sci,* **1989**,. 90:1–104; (b) H. Münstedt. **1988**, *Polymer* 29(2):296–302

[8] G. Daoust , M. Leclerc, **1991,** *Macromolecules* (24)**,** 455-459

[9] F. Jonas, G. Heywang and W. Schmidtberg. DE 38 13 589 A1 (Bayer AG), Prior:April 22, **1988**

[10] G. Heywang and F. Jonas, *Adv Mater,* **1992,** 4(2):116–118

[11] (a) L. Sun, S. C. Yang, *Polym. Prepr. Am. Chem. Soc. Div. Polym. Chem.* **1992**, 33, 379; (b) G. Heywang, F. Jonas, *Adv. Mater.* **1992**, 4, 116

[12] J. Friedrich, K. Werner, US-A 5 300 575; G. Heywang, F. Jonas, Adv. Mater. **1992**, 4, 116

[13] (a) U. Lang, N. Naujoks, J. Dual, *Synthetic Metals,* **2009**, (159) 473–479 (b) U. Lang, E. Müller, N. Naujoks, J. Dual, *Adv. Funct. Mater.,* **2009**, 19, 1215–1220

[14] A.N. Aleshin, S.R. Williams, A.J. Heeger, *Synthetic Metals*, **1998**, (94), 173-177

[15] F. C. Krebs, *Sol Energy Mater Sol Cells*, **2009**, 93(4):394–412.

[16] D. Hohnholz, A. G. MacDiarmid. *Synth Met*, **2001**, 121(1):1327–1328.

[17] T. Tachikawa, N. Itoh, S. Handa, D. Aoki, T. Miyake. *SID-Proceeding*, **2005**, 34.3:1280–1283.

[18] (a) Handbook of Organic Conductive Materials and Polymers (Ed.: H. S. Nalwa), Wiley, New York, **1997**; (b) Handbook of Conducting Polymers (Eds.: T. A. Skotheim, R. L. Elsenbaumer, J. F. Reynolds), 2nd ed., Marcel Dekker, New York, **1998**

CHAPTER 5

PEDOT thin films doped with polyoxometalate (POM) $[Co_4(H_2O)_2(PW_9O_{34})_2]^{10-}$ anions

5.1 INTRODUCTION

Polyoxometalates (POMs) are a wide class of inorganic compounds; recently, thanks to their great potentialities, they have found applications in different fields as catalysis, medicine, analytical chemistry and especially in material science.

POMs are widely studied because of their attractive electronic and molecular properties. They are soluble and stable in aqueous and non-aqueous solutions and have the ability to accept various numbers of electrons giving rise to a mixed-valence species. Moreover they can accommodate d-transition metals, leading to interesting magnetic properties. [1] [2]

There are a lot of different kinds of polyoxometalates, depending on the size, shape and chemical elements forming the clusters. Among the most common POMs, MO_6 units with octahedral geometry, MO_5 units with square planar or bipyramidal geometry or MO_4 units with tetrahedral geometry, form the polymeric oxoanions, where, generally, M is V^{5+}, Mo^{6+}, W^{6+} metal ion. [3]

The most common POMs types are shown in Figure 5.1. Their names originate from the scientist who first prepared them or found their structures.

a)   b)   c)

Figure 5.1: POMs: a) Kegging anion; b) Lindqvist anion; c) Well-Dawson anion

Those inorganic clusters are able to accommodate one or more paramagnetic

metal ions into a cage of diamagnetic metal oxides. This configuration leads to the isolation of the magnetic ion, so the complex shows paramagnetic properties at the molecular level. [4] For this reason, POMs are used as models for understanding magnetic properties, particularly when they are embedded in conducting layers: in this case it is possible to study the interactions between conducting layers and magnetic networks.

Besides, given that POMs show mixed-valence electrons with half-filled conducting band, they may give a further contribution to the whole conductivity.

In particular, the $[Co_4(H_2O)_2(PW_9O_{34})_2]^{10-}$ polyoxometalate exhibits electrochemical stability and interesting physical properties: it shows ferromagnetic interactions [2] [5] and the Co(III) metallic centers may reversibly accept up to four electrons. [6] In fact, this cobalt-containing polyoxometalate (POM) has proved to be an extremely active, stable, homogeneous water oxidation catalyst with either chemical or photochemical oxidants, as recently reported in literature. [7] [8] [9]

For these reasons, $[Co_4(H_2O)_2(PW_9O_{34})_2]^{10-}$ has been selected for doping the conducting polymer poly(3,4-ethylenedioxythiophene) PEDOT. The electrochemical stability and the physical properties of the obtained multifunctional material are the subjects of this chapter. The influence of the synthetic procedure on the obtained material properties is also investigated.

5.2 RESULTS AND DISCUSSION

5.2.1 Synthesis and characterization of $[(C_4H_9)_4N]_8H_2[Co_4(H_2O)_2(PW_9O_{34})_2]$

The $[TBA]_8H_2[Co_4(H_2O)_2(PW_9O_{34})_2]$ $(TBA^+ = (C_4H_9)_4N^+)$ has been prepared following a slight modification of the synthetic route reported in literature.[6] An aqueous solution of the analogue $K_{10}[Co_4(H_2O)_2(PW_9O_{34})_2] \cdot 22\ H_2O$ salt has been mixed with a 1,2-dichloroethane solution of TBABr. Extraction of the organic phase followed by slow ether diffusion affords deep purple crystals of $[TBA]_8H_2[Co_4(H_2O)_2(PW_9O_{34})_2]$.

X-ray structural analysis has been performed on a single crystal that was taken

out from the solution and placed immediately under a stream of nitrogen gas (at 120 K) and exposed to the X-ray beam. The structure of the polyoxoanion is similar to the corresponding potassium salt. [8] This polyoxotungstate is formed by two Keggin derivatives that chelate four Co(II) ions. The rigidity of the tungstophosphate fragment $(PW_9O_{34})^{9-}$ leads to a high symmetrical arrangement in which four sharing edges MO_6 octahedra are coplanar. (Figure 5.2)
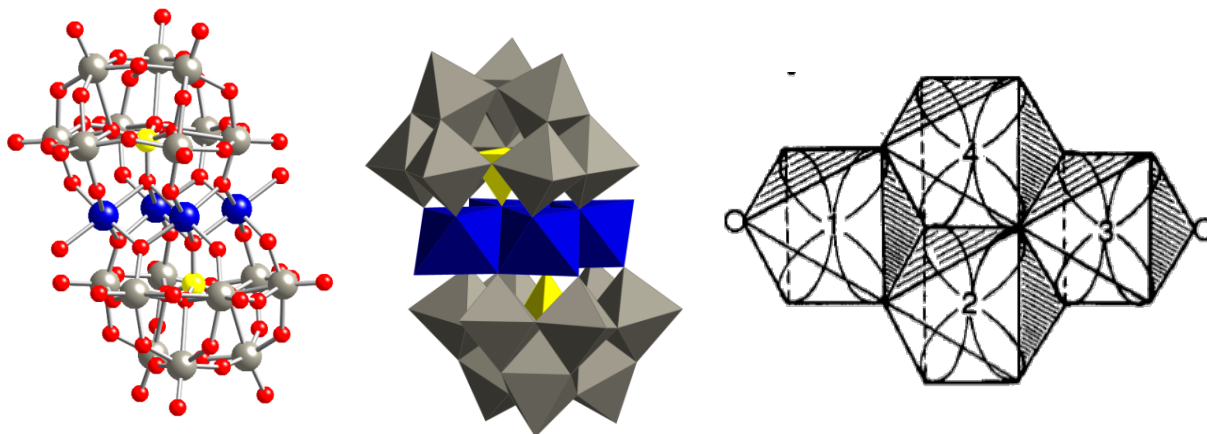

Figure 5.2: Structure of $[Co_4(H_2O)_2(PW_9O_{34})_2]^{10-}$ anion (left) and four cobalt belt geometry (right)

Structural data demonstrate the presence of 8 tetrabuthylammonium cations per formula. As the charge of the polyoxoanion is -10, the presence of two H^+ is necessary to counterbalance the anionic charge of the anion. These two H^+ cations are probably bound to the external oxygen atoms of the polyoxoanion and were not found in the X-ray analysis. Some residual peaks of electron density are located in empty regions of the structure which are assigned to water molecules, giving a total formula of $TBA_8H_2[Co_4(H_2O)_2(PW_9O_{34})$ 20 H_2O. These water molecules are very weakly bound and are quickly lost when the crystals are not in contact with the mother liquor. In fact, the loss of crystallinity is evident by the naked eye in just a few minutes.

Table 5.1: Crystal data and structure refinement for $TBA_8H_2[Co_4(H_2O)_2(PW_9O_{34})_2] \cdot 20$ H_2O

Formula weight	7032.67	
Temperature	120(2) K	
Wavelength	0.71073 Å	
Crystal system	monoclinic	
Space group	$P2_1/n$	
Unit cell dimensions	a = 18.9958(2) Å	α= 90°.
	b = 23.1904(3) Å	β= 91.8416(12)°.
	c = 28.1342(5) Å	γ = 90°.
Volume	12387.3(3) $Å^3$	
Z	2	
Density (calculated)	1.887 Mg/m^3	
Absorption coefficient	8.661 mm^{-1}	
F(000)	6704	
Theta range for data collection	2.34 to 32.04°.	
Index ranges	-27<=h<=28, -33<=k<=34, -41<=l<=37	
Reflections collected	182852	
Independent reflections	40540 [R(int) = 0.0546]	
Refinement method	Full-matrix least-squares on F^2	
Data / restraints / parameters	40540 / 52 / 1072	
Goodness-of-fit on F^2	1.095	
Final R indices [I>2sigma(I)]	R1 = 0.0889, wR2 = 0.2193	
R indices (all data)	R1 = 0.1760, wR2 = 0.2750	

Thermogravimetric analysis of the TBA salt (see Figure 5.3) does not provide evidence of co-crystallized water molecules, as the weight loss at 200 ºC is almost negligible. However, it is difficult to confirm if the two water molecules coordinated to the cobalt ions are lost, due to the large difference in mass when compared to the total mass of the compound. At temperatures higher than 200 ºC the compound losses weight due to the decomposition of the TBA^+ cations and, at 740º C the weight loss corresponds to the 31% of the initial value, which is in good agreement with the loss of the 8 TBA^+ cations contained in the salt.
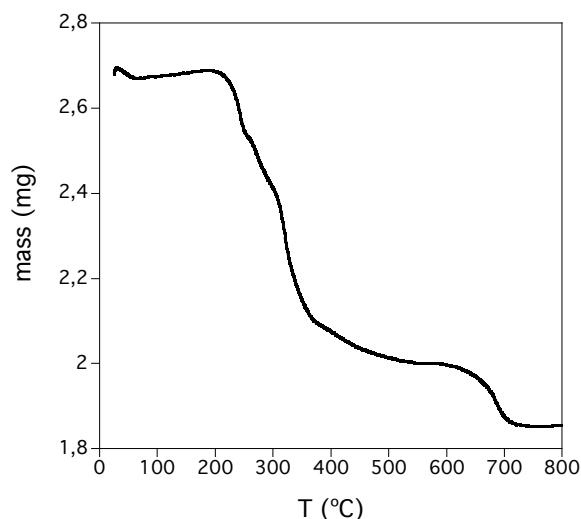
Figure 5.3: Thermogravimetric analysis of the salt $TBA_8H_2[Co_4(H_2O)_2(PW_9O_{34})_2]$

The electrochemical behavior of the salt $TBA_8H_2[Co_4(H_2O)_2(PW_9O_{34})_2]$ in acetonitrile has been previously reported. [6] Although in this work a polyoxometalate salt containing one additional TBA^+ cation per formula unit (a difference which is probably due to the different method of crystallization used) has been used in this work, the electrochemical behavior is essentially similar to the previously reported: the polyoxoanion exhibits three quasi-reversible waves within the interval between -1.6 and -2.2 V, which correspond to tungsten reductions (only detected when a graphite working electrode is used), and three reversible oxidation peaks at +0.9, +1.2 and +1.5 V (see Figure 5.4). The first two anodic peaks correspond to one-electron oxidations of each of the two cobalt (II) ions bound to a water molecule, while the third one was not reported in the previous study but is probably due to the oxidation of the other Co(II) ions of the cluster.
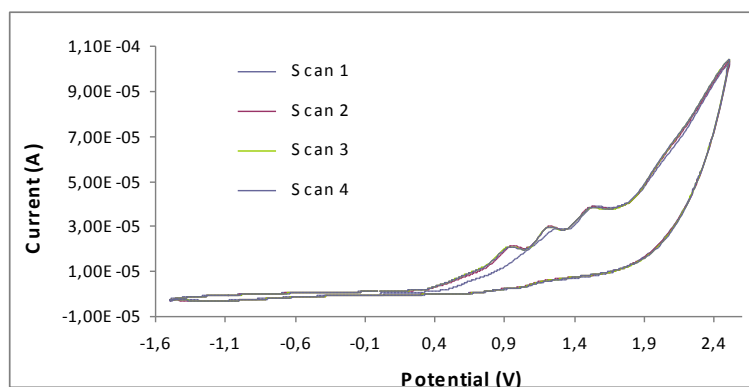

Figure 5.4: Cyclic voltammetry of $[TBA]_8H_2[Co_4(H_2O)_2(PW_9O_{34})_2]$ in ACN

5.2.2 Electrochemical polymerization

For obtaining PEDOT films doped with the POM anion, the potentiodynamic and potentiostatic electropolymerization methods have been discussed here.

Polymer films have been prepared from a solution of free monomer (EDOT) and $TBA_8H_2[Co_4(H_2O)_2(PW_9O_{34})_2]$ salt in CH_3CN in a three – electrode single compartment electrochemical cell. (Section 5.4.2)

The potentiodynamically generation of PEDOT films **(4)**, obtained by applying a potential within the range 1.0 and -2.0 V, is shown in Figure 5.5 (left). The cyclic voltammogram (CV) shows an irreversible oxidation peak around 1.0 V potential that increases regularly in the subsequent cycles, due to the film growth. The CV backsweep shows two reduction peaks around -0.2 and -0.5 V corresponding to the reduction of the initially deposited material. By repetitively sweeping between negative potentials and the maximum oxidation one, the polymer's redox system appears in the range -0.7 and -0.4 V as polymer coats the electrode. These features are common in most potentiodynamic generations of PEDOT polymers. [11]

Application of recurrent potential between -0.90 and +1.30 V induces the development of the new redox system corresponding to the doping/undoping process of the growing polymer. [12]
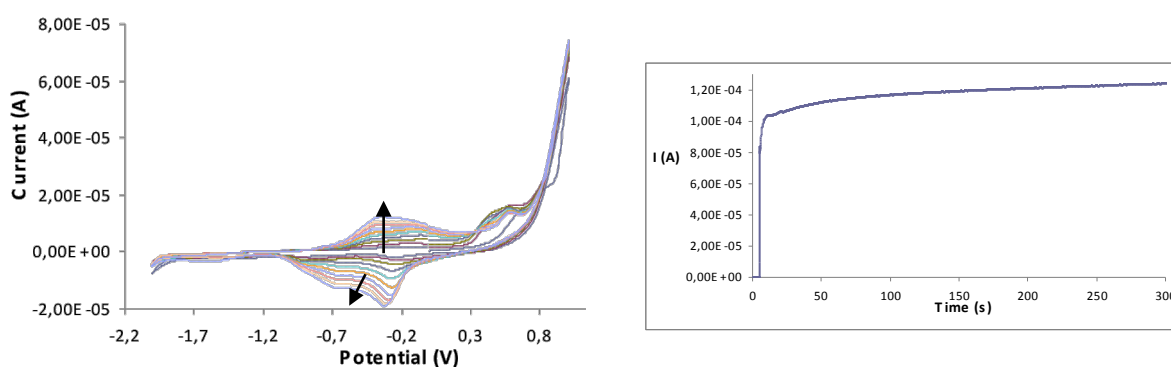

Figure 5.5: Film generation by cyclic voltammetry **(4)**[*left*]; film generation by coulometry **(5)** [*right*]

The potentiostatically generation of the PEDOT polymer **(5)**, performed by applying a 1.0 V constant potential is shown in Figure 5.5 (right). The current remains almost constant over the whole polymerization time.

After each experiment, a blue polymer attached on the platinum electrode is observed.

5.2.2.1 in situ *UV-Vis*

By using an indium tin oxide (ITO) transparent glass as working electrode, the spectroelectrochemical experiments have been performed, as described in the Experimental Part. The UV-Vis spectra registered during the **(4)** synthesis are reported in Figures 5.6 and 5.7.
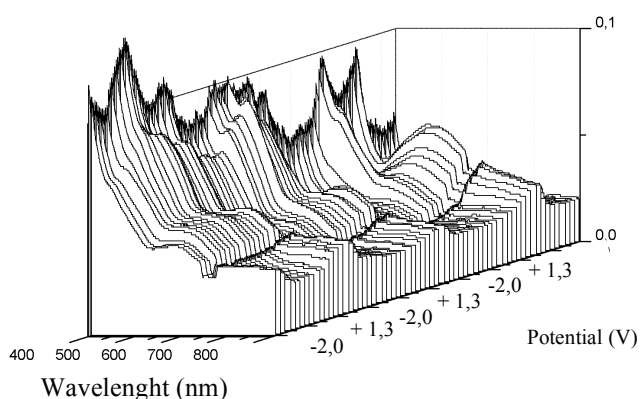

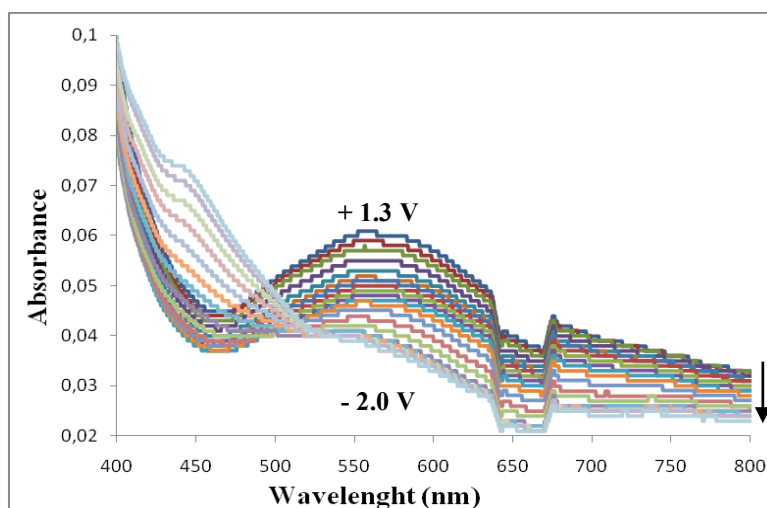**Figure 5.6:** UV-Vis spectra during film generation of **(4)** by cyclic voltammetry, ITO WE

Figure 5.7: *in situ* UV-Vis spectra for **(4)** from +1.3 V to -2.0 V; ITO WE

Although the absorbance is rather weak, one peak around 550 nm can be recognized, reaching the maximum intensity absorbance at + 1.3 V; periodically, a different peak, around 450 nm, appears as the previous one

decreases in intensity and the potential becomes more negative. Figure 5.7 is referred only to the first cycle for clarity. The latter peak can be assigned to the polymer in the reduced state, while the former is assigned to the oxidized polymer state, in accordance with some similar data reported in literature. [13] For the following sweeps the same behavior is registered but with an enhancement of absorbance intensity.

The *in situ* UV-Vis measurements have been performed also for **(5)**. In Figure 5.8, a broad band around 700 nm becomes more intense over time and it is assigned to the PEDOT oxidized state, as reported in literature. [6]
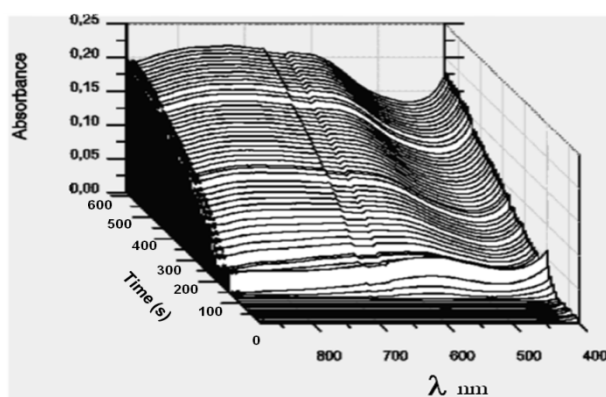

Figure 5.8: *in situ* UV-Vis spectra for **(5)**; constant potential of 1.3 V for 600 s; ITO working electrode,

After electropoymerization, a thin blue film covering the ITO glass is observed.

5.2.2.2 *EQCM*

The electrochemical quartz crystal microbalance (EQCM) is an ideal tool for examining transport of the incorporated chemical species in thin conducting films. In fact, the change in oscillation frequency of a quartz crystal is directed related to a mass variation occurring at the electrode surface. These experiments are useful to investigate phenomena such as doping/dedoping processes, although with EQCM measurements it is not possible to discriminate among anions, cations or neutral molecules. [14] More details about EQCM are reported in Appendix A.

In the following the results of mass variation versus potential are interpreted in a qualitative manner.

The EQCM experiment has been performed following the same procedure reported for the previous experiments and in Figure 5.9 the mass variation versus potential has been shown for the synthesis of **(4)**. During the first anodic sweep, a mass increase has been detectable only at more positive potentials than + 1.0 V, indicating that the polymerization only happens above this potential value. This can be related to the oxidation peak that appears at the positive potential limit in Figure 5.5, left. The mass increase continues in the initial part of the cathodic scan, up to a potential of about -0.7 V. From this value, the mass of the polymer remains constant down to a potential of about - 1.0 V, where a slight decrease of mass takes place. This can be due to some degree of polyoxometalate expulsion from the film or even to an electrodissolution process of some of the shorter polymer chains that would become soluble upon reduction and attainment of neutral charge. This kind of electrodissolution has previously been observed in other conducting films of polypyrrole doped with the polyoxometalate $[PW_{12}O_{40}]^{3-}$. [16] As expected, in the subsequent cycles the mass increase is initiated at less positive potentials in agreement with the fact that the oxidation potential is lower for longer polymer chains. After every cycle, there is net mass increase evidencing the polymer growth.
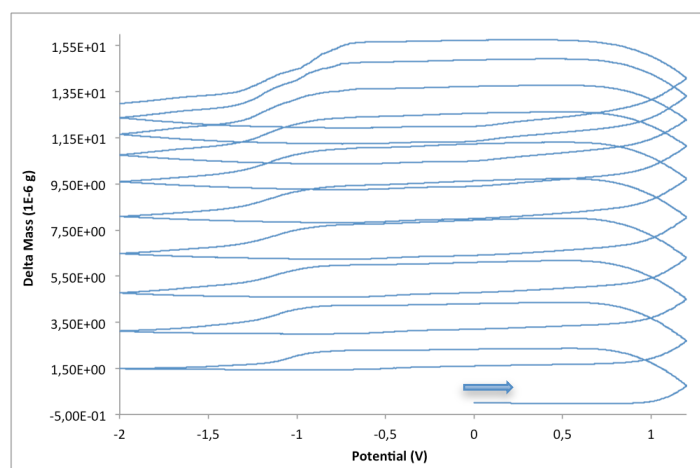

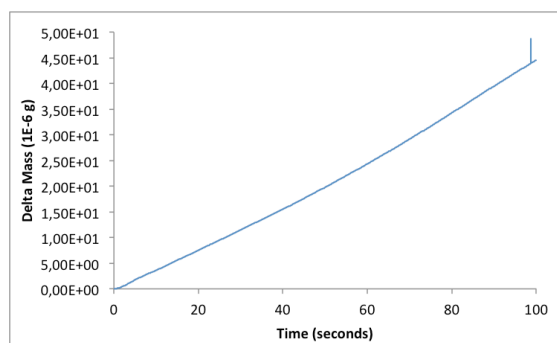**Figure 5.9:** Δmass response of quartz crystal during the synthesis of **(4)**

Figure 5.10: Δmass response of quartz crystal during the synthesis of **(5)**

In Figure 5.10 the mass variation for **(5)** synthesis of a PEDOT/POM film is presented. A continuous mass increase of the polymer with time (and also with charge) is observed which, according to some authors, can be an indication of the formation of a homogeneous film. [17]

5.2.3 Characterization of doped polymers

As observed by Naoi et al. [18], during the oxidation/reduction of PPy, cations, anions or both ions migrate out or into the polymer to achieve the charge compensation. On the contrary, Paik et al. [19] [20] observed that the heteropolytungstate ion $P_2W_{18}O_{62}^{6-}$ of Dawson structure can be retained in PPy obtained polymer for extended periods. Particularly, the heteropolytungstate anion have suitable chemical features, as the large molar mass, that allow this kind of complexes to be a perfect ion for studying the effects of polymerization method on the doped polymer permeability. [14]

In order to investigate the stability of **(4)** and **(5)**, both generated polymers have been subjected to potential cycling in ACN solution of TBAClO$_4$ or LiClO$_4$

The cyclic voltammogramms (CVs) for **(4)**, subjected to potential cycling when immersed in ACN solution containing TBAClO$_4$ or LiClO$_4$, have been reported in Figure 5.11 left and right, respectively.
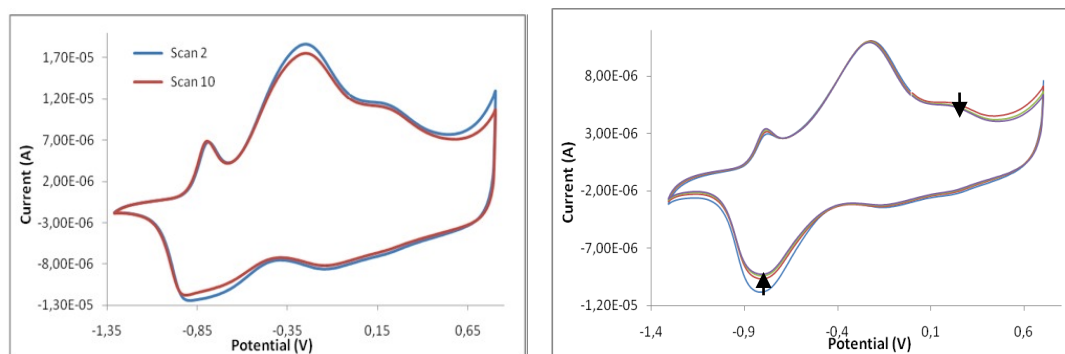
Figure 5.11: CVs of **(4)** in a 0.1 M TBAClO$_4$ [*left*]; and in a 0.1 M LiClO$_4$ [*right*] ACN solutions

Both CVs showed a very similar behavior that did not change significantly during 10 subsequent cycles. Only a very slight decrease in the intensity is observed in each case after 10 cycles. This kind of behavior is expected for polymers whose composition is not significantly altered after each potential cycle. If this is true, after each complete cycle, the net insertion of ions into the polymeric matrix from the solution (necessary to keep the electroneutrality upon the redox processes of the polymer) must be almost negligible and, accordingly, the polyoxometalate anion is expected to remain in the polymer and not exchanged significantly with the solution. This point will be confirmed with the ECQM experiments (Section 5.2.3.2).

On the other hand, the CV reported in Figure 5.11 is similar to the PEDOT film CV reported in literature: a weak anodic shoulder, a main anodic wave and a cathodic wave are detectable. [12] [21] Differences in peaks positions, especially for the intense and well-resolved anodic peak, are a direct consequence of the considerable influence of the nature and charge of electrolyte cation, as already reported in literature. [12] [21] [22]

The cyclic voltammogramms (CVs) for **(5)**, subjected to potential cycling when immersed in ACN solution containing TBAClO$_4$ or LiClO$_4$, have been reported in Figure 5.12 left and right, respectively. The shape of the CVs exhibits an evolution with the number of cycles, leading to clear differences between the first and subsequent cycles. Particularly, it can be highlighted that the anodic peak in the first scan completely disappears after few sweeps. In literature, this peak is assigned to POM loss. [16] [23] If the film looses POM ions, others anions should enter in the film for maintaining the electroneutrality.
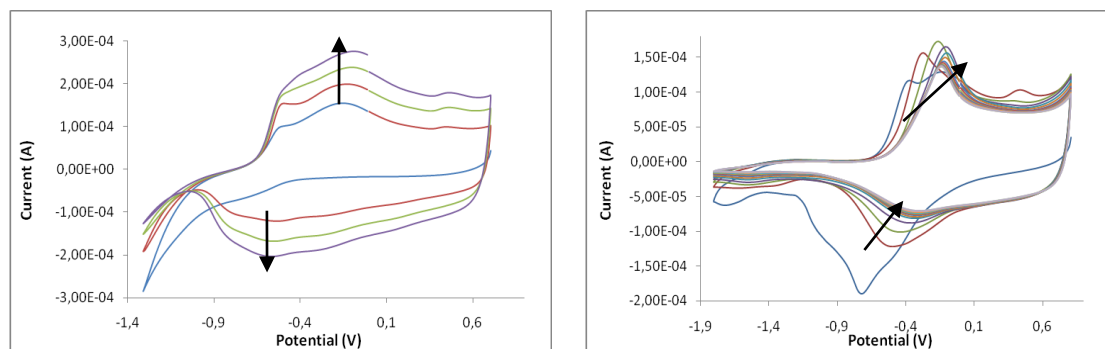
Figure 5.12: CVs of **(5)** in a 0.1 M TBAClO$_4$ [*left*]; and in a 0.1 M LiClO$_4$ [*right*] ACN solutions

For the CV performed in LiClO$_4$ (Figure 5.12, right) the first cycle (in blue) exhibits a broad cathodic wave centred at about -0.7 V, which dramatically decreases in intensity in the next cycles and also suffers an anodic shift. An evolution of the composition of the polymer is clearly taking place with potential cycling. During the cathodic polarization, the reduction of the polymer must be accompanied either by the insertion of Li$^+$ cations (which would probably be solvated) or the expulsion of polyoxometalate anions. It is actually very likely that both processes are happening at the same time.

The same processes must happen in the CV performed in TBAClO$_4$ (Figure 5.12, left). In this case, however, a clear negative shift of the cathodic peak is observed in the first cycle (blue line), which appears at more negative potentials than -1.5 V and, then, is out of the potential window employed in the experiment. Such a negative shift is expected, as the insertion of the TBA$^+$ cations in the polymeric matrix is required to keep the electroneutrality when the polymer is reduced. The insertion of the larger cations (compared with the Li$^+$ cations) require the opening of larger pores in the polymer and so bigger structural changes in the polymer chains, which can only be effected with larger (more negative) potential values. Again, an expulsion of the polyoxometalate anions is likely, along with insertion of TBA$^+$ cations.

During the reverse (anodic) scan, the oxidation of the hybrid material takes place. One of these processes is then necessary: either the ejection of the cations (Li$^+$ or TBA$^+$) inserted during the previous cathodic scan, and/or the insertion of perchlorate anions from the solution. Therefore, depending on the actual exchange processes happening (and its extension), an accumulation of salt

inside the polymeric film (LiClO$_4$ or TBAClO$_4$) can be taking place, or even a partial substitution of the polyoxometalate anions inside the polymer by the anions present in the solution. All these changes will be further discussed with the electrochemical quartz crystal microbalance results (Section 5.2.3.2) and the EDX analysis (Section 5.2.4.1).

5.2.3.1 *UV-Vis* in situ

The UV-Vis *in situ* experiments have been performed with the aim of understanding better the equilibria evolved when the doped polymers are subjected to potential cycling. Depending of the electropolymerization method, the doped polymer behavior is different as shown in Figures 5.13 and 5.14.
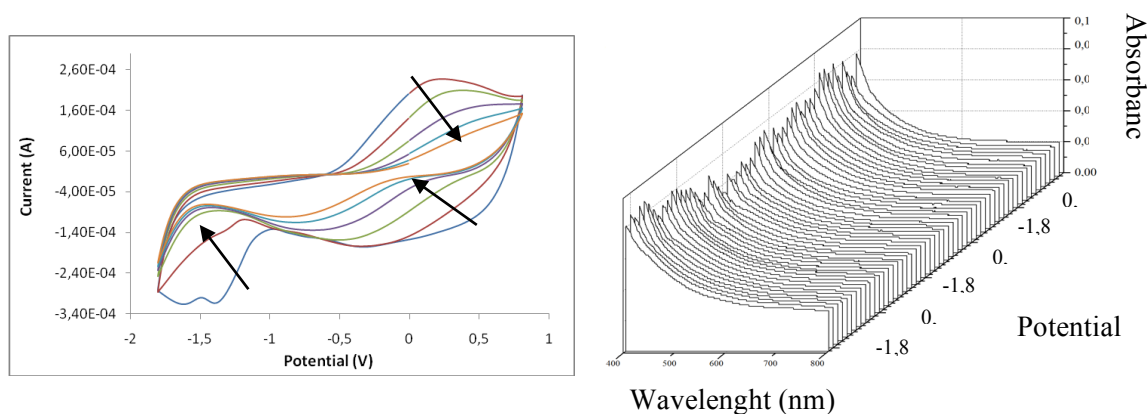

Figure 5.13: CVs (left) and *in situ* UV-Vis spectrum (right) for **(4)** immersed in ACN of LiClO$_4$

In fact, a development in the CV profile has been observed for **(4)** whereas no peak appears in the *in situ* UV-Vis spectra. (Figure 5.13) The ITO glass was almost totally transparent before, during and after the experiment.
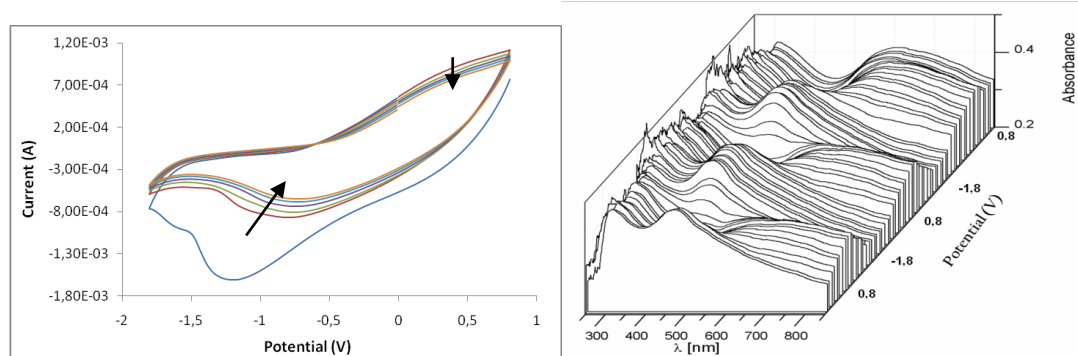
Figure 5.14: CVs (left) and *in situ* UV-Vis spectrum (right) for **(5)** immersed in ACN of LiClO$_4$

Also for **(5)**, the difference between the first cycle with respect to the following ones is evident: a large cathodic peak appears around -1.2 V whereas in the second cycle, it disappears and moves to a less intense peak, centered around -0.8 V that is attributed to a POM loss. (Figure 5.15) A close look to the UV-Vis spectra shows a periodic change of two bands. In Figure 5.15, the UV-Vis spectra for the first sweep from 0.8 V to -1.8 V are reported. Three bands are evident and centered: (I) around 300 nm; (II) at 450 nm; (III) at 650 nm. The first one is related to the POM while the other ones are due to PEDOT.

(I) is independent of the potential since the only change is a slight difference in intensity, although appearing in the limit region of the instrument scan. This band is characteristic of the polyoxometalates [23] and is attributed to charge transfer from an O^{2-} ion to a W^{6+} ion in the POM cluster at W=O and W-O-W bonds. [24]

(II) appears when moving to more negative potentials and is more intense than band (III). It is attributed to a $\pi \rightarrow \pi^*$ transition. [25], [26] It is noteworthy that there is a maximum of absorbance when the potential is around -1.3 V; this corresponds to the maximum of intensity of the cathodic peak in the CV.

(III) appears when the potential shifts towards positive values. Its spectral features (wavelength and shape) strongly resembled those of the oxidized-PEDOT broad band that was observed in the UV-Vis spectra of the electropolymer synthesis. This conclusion is supported by lot of

examples present in literature. The absorption wavelength strictly depends on the doping ion inserted into the film. [24] [27]
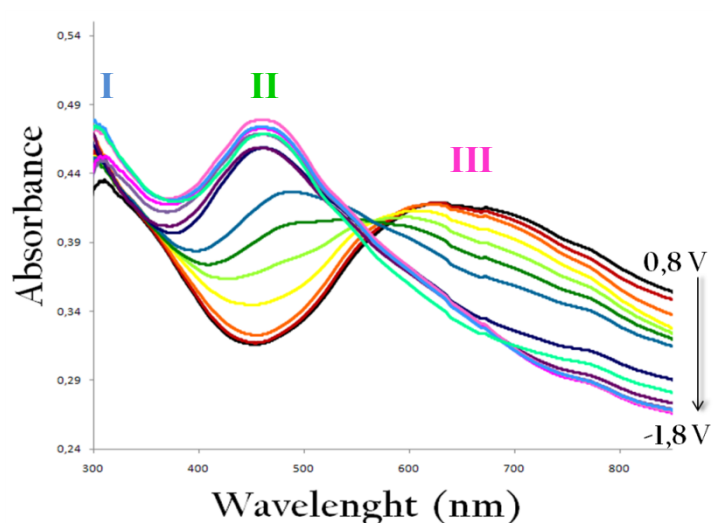

Figure 5.15: UV-Vis spectra from chrocoulometry generated film [Potential from 0.8 V to -1.8 V] in a 0.1 M LiClO$_4$ ACN solution; ITO working electrode

The bands absorbance diminishes a little as the number of the sweeps increases. This effect can be ascribed to a lower transparency of the ITO glass due to the formation of the solid product.

On the basis of UV-Vis spectra it is possible to determine the E$_g$, the energy band gap, by extrapolation of the π - π^* absorbance onset to the background, a value around to 2,2 eV for the PEDOT doped with POM can be estimated. [28]

5.2.3.2 *EQCM*

The EQCM experiments have been performed for both **(4)** and **(5)** films. (Figure 5.16 and 5.17)
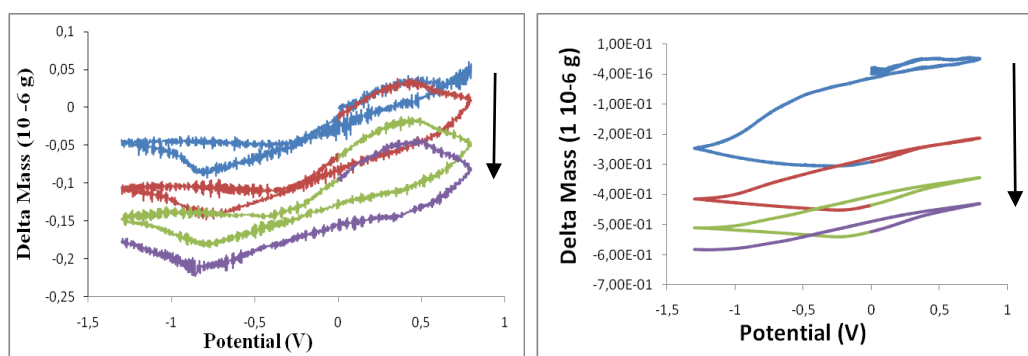
Figure 5.16: Mass changes for **(4)** film immersed in LiClO$_4$ (*left*) and TBAClO$_4$ (*right*) ACN solutions

In Figure 5.16 (left) it can be observed that, in the first anodic scan the mass of the film increases slightly which can only be due to an insertion of perchlorate anions into the film from the solution. This increase of mass continues until the anodic limit is reached and then in the reverse (cathodic) scan, a steady decrease of mass is registered which continues down to -0.75 V, where a minimum in the mass value can be found. As the total decrease of mass is greater than the increase of mass registered in the previous anodic scan, the mass loss cannot be due only to expulsion of perchlorate anions but to an additional ejection of either some polyoxometalate anions or some oligomers of PEDOT which would be soluble upon reduction. As the mass variation is very small, it can be assumed that polyoxometalate anions (having a very large molecular mass) remain inside the polymer and that some oligomers are ejected from the polymer upon reduction. A similar electrodissolution process has previously been described for polypyrrol films doped with Keggin polyoxometalates. [16] At lower potentials than -1.0 V (in the cathodic scan), a slight increase of mass in detected which must be attributed to the insertion of solvated Li$^+$ cations. The solvation of the highly polarizing Li$^+$ cations accounts for the observed mass increase which otherwise would not be detected owing the small mass of the lithium cations. In the following reversed anodic scan there is no mass variation up to about 0.3 V, where a new mass increase is detected. This mass increased must be attributed to the insertion of perchlorate anions, as in the previous anodic scan. At potentials higher than 0.4 V a new mass decrease is observed. As a similar loss of mass does not take place in the

first anodic scan, but only in the second (and subsequent) anodic scans, this loss of mass must be ascribed to the expulsion of solvated lithium cations that were inserted in the previous cathodic scan. After each complete cycle, a net mass loss is observed for the polymer, although it is less after each cycle and therefore it shows a tendency to stabilize after some few cycles. It is also to be noticed that the whole mass variations are very small for this experiment (10^{-7} g) in agreement with the almost unchanged cyclic voltammograms for this system (shown in Figure 5.11, left).

An almost similar behavior exhibit the mass variation versus potential when the film is cycled in $TBAClO_4$ (Figure 5.16, right), but in this case no increase of mass is detected at the end of each cathodic scan (which was in the previous case attributed to an insertion of lithium cations) and, accordingly, there is no a corresponding mass decrease at the end of the anodic scan (which was previously attributed the a release of lithium cations). Therefore it can be deduced that the TBA^+ cations are not exchanged between the solution and the film due to its larger size when compared to the lithium cations.

The CV in $TBAClO_4$ ACN solution of the doped PEDOT generated by coulometry is shown in Figure 5.17. The mass variation in this case is one order of magnitude larger than for the potentiodynamically-generated films. It is observed that the mass of the polymer is greatly reduced at the end of each cathodic scan (below approximately -1.0 V), which is attributed now to a polyoxometalate ejection from the film into the surrounding solution. The mass loss becomes less after each cycle showing a tendency to stabilize in agreement with the behavior of the corresponding cyclic voltammogram (see Figure 5.12). The little amount of added mass at the oxidation potentials suggests an insertion of ClO_4^- ions.
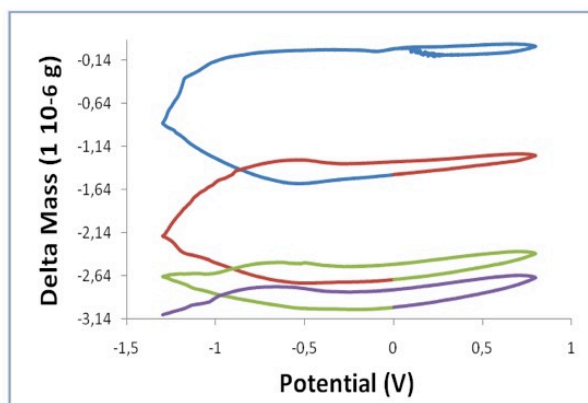
Figure 5.17: Mass changes of PEDOT/POM films generated by coulometry in 0,1M TBAClO$_4$ ACN solution

It is possible to conclude that the polymer generation method is crucial for the film features: perhaps the **(5)** film is likely to have a bigger porosity or different cross-linking degree with respect to the CV-generated one. A similar conclusion was reached for other polymers containing PPy and Keggin polyoxometalates or other large anions, such as macrocyclic anions. [14]

5.2.4 Physical properties for (5)

5.2.4.1 *SEM/EDX*

Since the progressive alternation in the voltammetric profile observed when the material is submitted to consecutive potential cycles could also reveal alterations in the film morphology, [23] scanning electron microscopy (SEM) and energy-dispersive X-rays (EDX) analyses are reported here for **(5)** films.

These analyses have not been performed for **(4)** sample, since it has been not possible to remove the film from the electrode without altering or destroying the sample.

The **(5)** shows a matt and a bright part, which is the one attached to the electrode, but EDX spectra have been demonstrated that the sample is homogeneous. For this reason, only the EDX spectrum and SEM micrography for the matt part is shown in Figure 5.18.
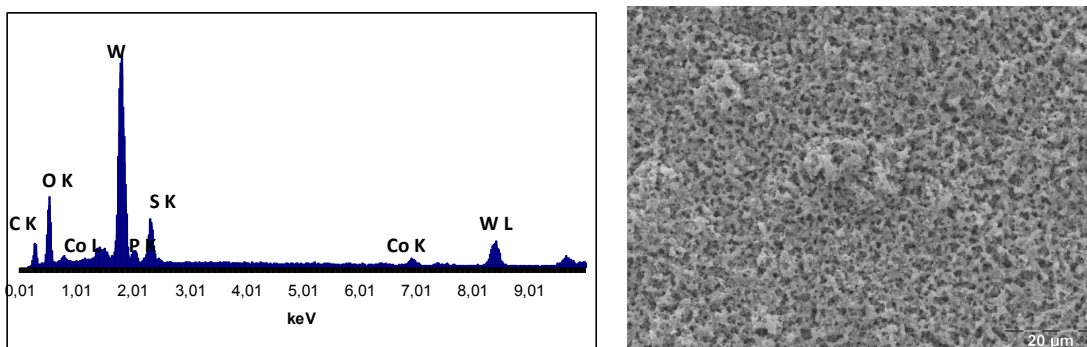
Figure 5.18: EDX spectra (**left**) and SEM micrography (**right**) for a freshly synthesized film at 1.0 V

The EDX spectrum exhibits intense peaks of tungsten (due to POM anions) and S (due to PEDOT chains).

From the relative signal ratio of Co (K) and S (K) peaks, a ratio of about 10:1 EDOT/POM has been found. This is confirmed by elemental analysis ($[C_6H_4SO_2]_{11.85}[Co_4(H_2O)_2(PW_9O_{34})_2]$ 35 H_2O). Although the synthesis has performed in non-aqueous solution, water molecules may be inserted into the polymer from the air once the film is separated from the solution, as this kind of conducting polymers can be hygroscopic.

In Figure 5.19, the SEM and EDX spectra for a potentiostatically generated film at 1.5 V have been reported.
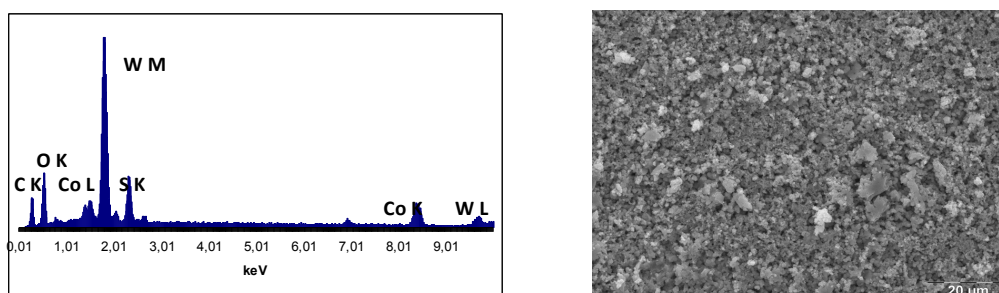

Figure 5.19: EDX spectra (**left**) and SEM micrography (**right**) for a freshly synthesized film at 1.5 V

For this film, the intensity ratio of the S(K) and Co(K) peaks is larger than for the polymers generated at 1.0 V. This may imply that a larger ratio EDOT/POM is observed when the potential of electropolymerization increases.

5 μm SEM micrographies, showing a different morphology for these two samples, are reported in Figure 5.20.
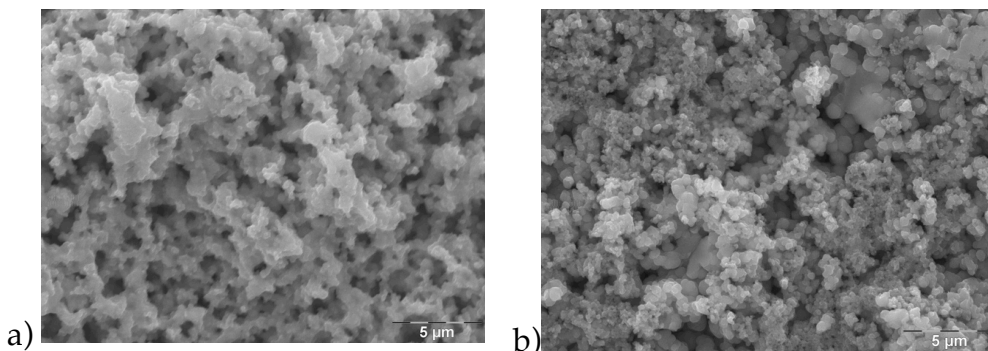

Figure 5.20: SEM micrographies of coulometry generated film a) at 1,0V for 750 seconds; b) at 1,5V for 750 seconds;
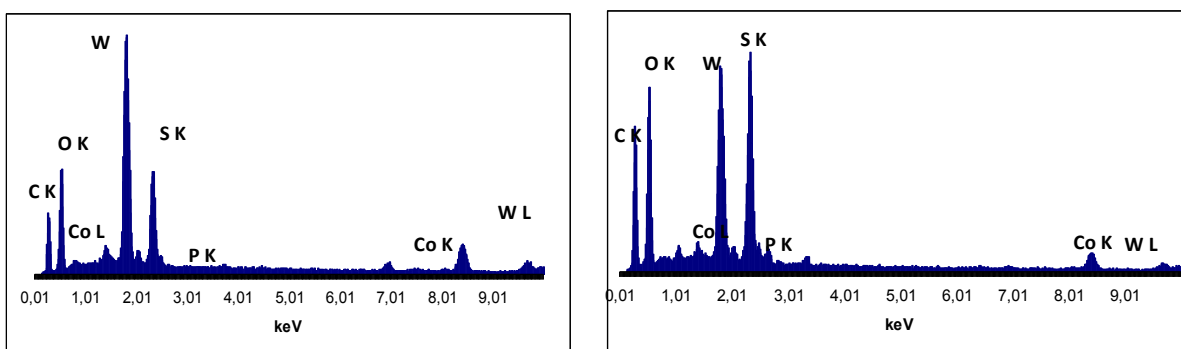

Figure 5.21: EDX spectra for the film after 2 scans (**left**) and after 20 scans (**right**), in LiClO$_4$ (0,1 M) ACN solution

Film composition changes become more evident from the EDX spectra showed in Figure 5.21 (right): after 20 cycles in which the film is put in contact with a solution of LiClO$_4$ (0,1 M) in ACN, the peaks due to the POM are strongly reduced, in particular the W(M) peak is lower than the S(K) one that. This is consistent with the electrochemical results.

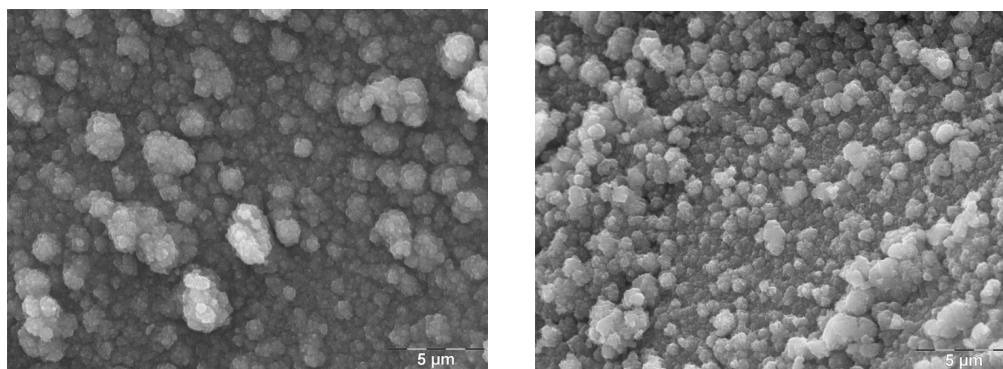SEM micrographies for these two films, reported in Figure 5.22, an increase of a "sponge-like" deposit.

Figure 5.22: SEM micrographies obtained for the film after a cycle (**left**) and after 20 cycles (**right**) in LiClO$_4$ (0,1 M) ACN solution

As demonstrated previously [11] [23], it is clear that a correlation between morphology and film composition exists, but it is not so easy to determine. Although no information about the bulk morphology can be obtained, nonetheless the influence of factors such as the potential of electropolymerisation on the surface morphology has been demonstrated. Moreover, the ions exchange phenomena have some effects on the polymer surface and the SEM micrographies highlight these differences, although it is necessary to deeper understand the relationship between morphology and ions exchange.

5.2.4.2 ex situ *conductivity measurements*

The "four-contacts probe" has proven to be a convenient tool for the measurement of resistivity. [29]
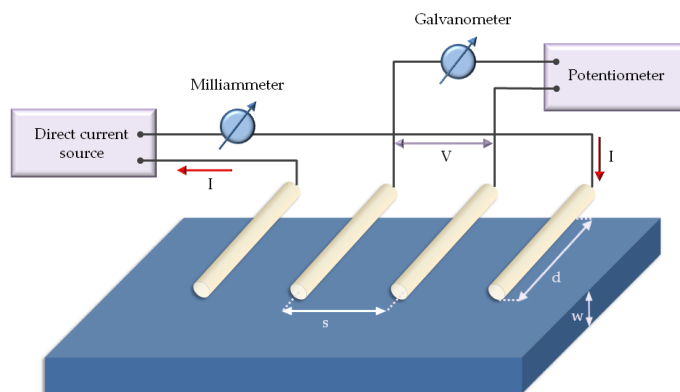
Figure 5.23: Circuit used for resistivity measurements with a four-probe arrangement on a rectangular sample

A constant current (I) is applied between the outer pair of the "four-contacts probes" while the potential difference (ΔV) arising from this current is measured at the two inner contacts. (Figure 5.23) It is possible to calculate the resistance (R) using the measured potential difference by the Ohm's law (V=IR). The conductivity is then calculated from **Equation x.1**:

$$\sigma \ (S \cdot cm^{-1}) = \frac{s \ (cm)}{R \ (\Omega) \cdot d \ (cm) \cdot w \ (cm)} \qquad \textbf{(Eq. X.1)}$$
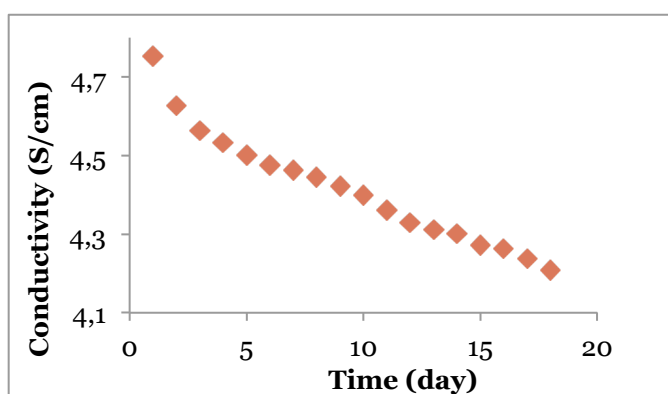

Figure 5.24: Resistivity (left) and conductivity (right) measured every day for 17 days

Resistivity and conductivity measurements (at r. t.) for **(5)** have been shown in Figure 5.24. The initial conductivity has a value of 4,75 S/cm and after 17 days a

decrease in the conductivity of approximately a 11% is registered. This could be due to a reaction of the polymer backbone with molecular oxygen, disrupting the conjugation and a consequent impeding the inter-chain charge movement. This effect leads to a lowering the mobility of the charge and hence the conductivity. [30]

5.2.4.3 *Magnetic Measurements*

Magnetic measurements are shown in Figure 5.25. In the temperature range between 40 and 100 K, the polymer magnetic contribution is observed: as the temperature goes down, it is possible to observe an antiferromagnetic coupling. The presence of a maximum at ~10 K confirms the presence of the Co clusters. In fact, this is the typical curve, expected for such system. Comparing the temperature vs χT graph reported in Figure 5.25 with the one reported in literature [2], it is possible to assume that the POM anion is inserted in the polymer and that its structural characteristics are not changed.
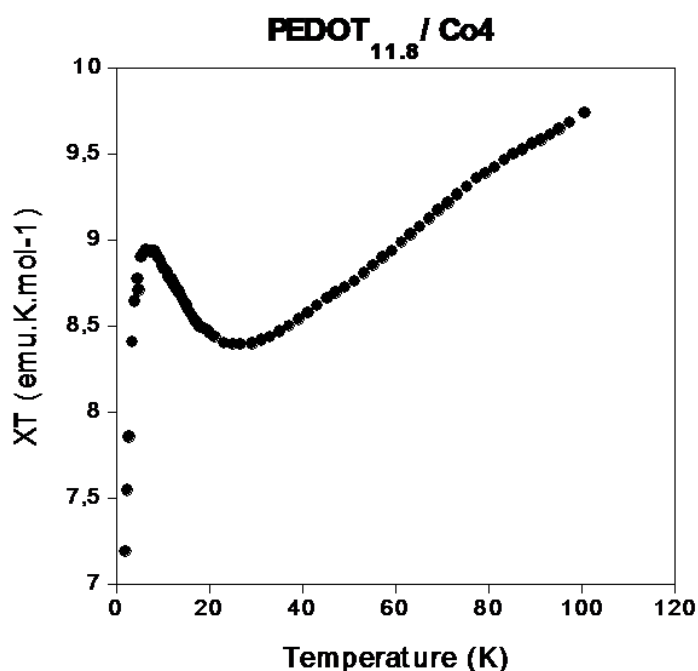

Figure 5.25: Magnetic measurements for the freshly synthesized **(5)**

5.3 Conclusions

A new multifunctional material consisting of a conductive film of PEDOT doped with the magnetic polyoxometalate $[Co_4(H_2O)_2(PW_9O_{34})_2]^{10-}$ has been obtained. As far as we know this is the largest polyoxometalate that has been used as a dopant anion of a conducting polymer of PEDOT. Depending on the synthesis method, it was possible to synthesize different materials with different characteristics.

According to the electrochemical quartz crystal microbalance (EQCM) results, the PEDOT/POM film obtained using a potentiodynamic method **(4)** is more stable than a similar material obtained using a constant potential of synthesis **(5)**, when the materials are subjected to potential cycling in acetonitrile solutions of $LiClO_4$ and $TBAClO_4$. The polyoxometalates are not expelled from the potentiodynamically synthetized films while they are expelled from the films obtained by potentiostatic methods. Moreover, the EQCM results indicate that lithium cations are easily exchanged between the films and the solution when the potential is cycled, while the larger tetrabutylammonium cations are not exchanged in the range of potentials studied. The morphology of **(5)** has been studied using SEM and the composition of the films obtained potentiostatically has been determined by chemical analysis and the EDX spectra. The conductivity of **(5)** film has been determined by the four contacts method to be ~4 S/cm at room temperature, and the conductivity decreases by 11% over a period of 18 days. The magnetic measurements also reveal the presence of the POM anion inserted into the polymer.

As a future perspective, a study of **(4)** and **(5)** as electrocatalysts towards water oxidation appears very interesting as, recently it has been reported that the polyoxometalate $[Co_4(H_2O)_2(PW_9O_{34})_2]^{10-}$ is an extremely active water oxidation catalyst with either chemical or photochemical oxidants. [7]

5.4 Experimental Section

All reagents were used as received including HPLC grade CH_3CN (ACN).

5.4.1 Synthesis of $[Co_4(H_2O)_2(PW_9O_{34})_2]^{10}$

The synthesis of $[TBA]_8H_2[Co_4(H_2O)_2(PW_9O_{34})_2]$ $(TBA^+ = C_4H_9)_4N^+)$ was performed following the reported method [6] [31] [32], although with a slight modification: an aqueous solution of the salt $K_{10}[Co_4(H_2O)_2(PW_9O_{34})]\cdot 22\ H_2O$ (2.7 mmol in 270 mL) was added to an identical volume of TBABr (42 mmol) in 1,2-dichloroethane. The polyoxoanion was extracted into 1,2-dichloroethane. A second organic extract was collected by a further addition of TBABr organic solution. The organic extracts were left in slow diffusion with Et_2O. In few days, deep purple crystals were formed; they were collected and washed quickly with EtOH and Et_2O. The identity of the compound was determined by IR spectroscopy [(cm^{-1}) ν_{as}(P-O), 1067 (sh), 1043; ν_{as}(W=O), 967, 947; ν_{as}(W-O$_b$-W), 883; ν_{as}(W-O$_c$-W), 835, 776], X-ray diffraction: Oxford Diffraction XcaliburTM diffractometer equipped with a sapphire 3CDD detector. The data collection routine, unit cell refinement and data processing were carried out with the program CRYSTALIS elemental analysis (Anal Calc for $[(C_4H_9)_4N]_8H_2[Co_4(H_2O)_2(PW_9O_{34})_2]$: C 23.04, H 4.44, N 1.69 ; found: C 22.72, H 4.40, N 1.66) and thermogravimetric analysis. The elemental analysis was made at the Universidad Computense de Madrid by LECO CHNS-932 (3288).

5.4.2 Electrochemical synthesis of doped polymers

Polymer films were grown in a small-scale (volume: 15 mL), three-electrode single compartment electrochemical cell, each electrode was spaced by a Teflon cap. The working electrode (WE) was a platinum disk with 0.2 cm^2 geometric area. The WE surface was polished with 1.0, 0.3 and 0.05 μm alumina and washed with distilled water and ethanol before each experiment. The counter electrode was a platinum wire. The reference electrode (RE) comprised an Ag wire immersed in a solution of $AgNO_3$ (0.01 M) and $TBAClO_4$ (0.1 M) in acetonitrile (ACN). The Ag/Ag^+ RE was calibrated against ferrocene/ferrocenium redox couple (1mM) in the same solvent/electrolyte system. At scan rate between 20 and 200 mV/s, ferrocene presented $E_{1/2} = +0.087$ V(+0.080 experimental) vs. Ag/Ag^+, with a peak separation, ΔE_p (anodic

to cathodic) of 71 mV(65 experimental). All potentials quoted are relative to the Ag/Ag^+ RE. The measurements were made at room temperature (ca. 25°C), within the potential window +2500 to -2000 mV using the cyclic voltammetry (CV) method and 1.0 V constant potential during the chronocoulometry (Coul) method. The solutions were degassed with pure nitrogen for 5 minutes before use and blanketed with nitrogen gas during the voltammetric scans.

All polymers were routinely prepared from a 0.1 M solution of free monomer (EDOT) in a solution of TBA(POM) 2.0 $*10^{-2}$ M in CH_3CN by applying a potential between 1.0 and -2.0 V (potentiodynamic generation) or by applying a constant potential at 1.0 V for 300 s (potentiostatic generation).

The elemental analysis was performed for the potentiostatically generated doped PEDOT at the Universidad Computense de Madrid by LECO CHNS-932 (3288): for $[C_6H_4SO_2]_{11.85}[Co_4(H_2O)_2(PW_9O_{34})_2]$ 35 H_2O: anal. calc. C 12.30, H 1.05, S 5.47, N 0.0; found: C 12.31, H 1.75, S 5.41, N 0.17.

The obtained doped polymers have been subjected to potential cycling in acetonitrile solutions of $LiClO_4$ (0.1 M) and $TBAClO_4$ (0.1 M).

5.4.2.1 *UV-Vis* in situ

The WE was an indium-tin oxide (ITO) coated glass; the CE was a platinum foil and the RE comprised an Ag wire immersed in a solution of $AgNO_3$ (0.01 M) and $TBAClO_4$ (0.1 M) in acetonitrile (ACN). The three-electrode system was inserted in the cell and the solution was degassed with pure nitrogen for 5 minutes. The experiments have been performed at room temperature and UV-Vis spectra were acquired over the range 900 - 350 nm.

5.4.2.2 *EQCM*

The cell was made with a crystal electrode in which one side of the crystal faces the solution and the other faces air. The resonant frequency of the fundamental mode of our crystal is 7.995 Hz. The diameter of the quartz crystal is 13.5 mm and the one of the gold electrode is 5.1 mm. A bare of platinum was used as counter electrode and Ag/Ag^+ in acetonitrile, $TBAClO_4$ 0.1 M, $AgNO_3$ 0.01 M electrode was used as reference one.

5.4.3 Physical Measurements

SEM/EDX

Scanning electron microscopy (SEM) experiments have been carried out using Philips SEM-XL30 equipped with an EDAX microprobe, used for determing metallic atomic composition of samples.

Ex-situ Conductivity

The *ex situ* conductivity measurements were performed on a polymer film obtained from polymerization applying a constant potential of 1,5 V for 750 seconds. Then it was detached from the electrode, washed with ACN and left drying under vacuum. The sample was cut for obtaining an almost rectangular shape (length of $3.25*10^{-2}$ cm; width of $3*10^{-2}$ cm). The thickness was around $5*10^{-3}$ cm as measured with the aid of an optical microscope. Four platinum wires were connected to the film using a conducting graphite paste.
Conductivity measurements were made using a linear four-probe geometry in a Quantum Design MPMS-9 equipment.

Magnetic measurements

The magnetic susceptibility measurements were carried out in the temperature range 2-300 K with an applied magnetic field of 0.1 T on a sample of compound **(5)** with a Quantum Design MPMS-XL-5 SQUID susceptometer. The susceptibility data were corrected for the sample holder previously measured using the same conditions.

REFERENCES

[1] M. Clemente-León, B. Agricole, C. Mingotaud, C. J. Gómez-García, E. Coronado and P. Delhaes, *Langmuir*, **1997**, *13*, 2340-2347
[2] C. J. Gómez-García, E. Coronado and Juan J. Borris-Almenar, *Inorganic Chemistry*, **1992**, 31 (*Vol. 9*), 1667-1673

[3] Shaoqin Liu, Zhiyong Tangb, *Nano Today*, **2010**, *5*, 267-281

[4] J. M. Clemente-Juan, M, Clemente-León, E. Coronado, A. Forment, A. Gaita, C. J. Gómez-García, E. Martínez-Ferrero, *Polyoxometalates: from magnetic models to multifunctional materials*, **2002**, Toshihiro Yamase and Michael T. Pope Editors

[5] H. Andres, J.M. Clemente-Juan, M. Aebersold, H.U. Güdel, E. Coronado, H. Büttner, G. Kearly, J. Melero, R. Burriel, *J. Am. Chem. Soc.*, **1999**, *121*, 10028-10034

[6] M. S. Balula, J. A. Gamelas, H. M. Carapuc¸ A. M. V. Cavaleiro, W. Schlindwein, *Eur. Journ. of Inorg. Chem.* **2004**, 619.

[7] Yin, Q.; Tan, J.M:; Besson, C.; Geletii, Y.V; Musaev, D.G.; Kuznetsov, A.E.; Luo, Z.; Hardcastle, K.I.; Hill, C.L. *Science* **2010**, 328, 342;

[8] Huang, Z.; Luo, Z.; Geletii, Y.V.; Vickers, J.W.; Yin, Q.; Wu, D.; Hou, Y.; Ding, Y.; Song, J.; Musaev, D.G.; Hill, C.L.; Lian, T. *J. Am. Chem. Soc.* **2011**, 133, 2068.

[9] J.J. Stracke, R. G. Finke *J.Am. Chem. Soc.* **2011**, 133, 14872

[10] L.M. Abrantes, C.M. Cordas, E. Vieil, *Electrochim. Acta*, **2002**, *47*, 1481.

[11] B. Groenendaal, G. Zotti, P.-H. Aubert, S.M. Waybright, J.R. Reynolds, *Adv. Mater.* **2003**, *15*, 855-879

[12] Said Akoudad, Jean Roncali, *Electroc. Comm.*, 2 (**2000**) 72.

[13] Xiwen Chen, Ke-Zhao Xing, Olle Ingana¨s, *Jour. Phys. Chem.* **1996**, *8*, 2439.

[14] W. Paik, I.-H. Yeo, H. Suh, Y. Kim, E. Song, *Electrochim. Acta*, **2000**, *45*, 3833.

[15] C. Weidlich, K.-M. Mangold, K. Jŭttner, *Electrochim. Acta*, **2005**, *50*, 1547.

[16] T. F. Otero, S. A. Cheng, F. Huerta, *Journ. Phys. Chem. B*, **2000**, *104,* 10522.

[17] V.M. Schmidt, H. Heitbaum, Electrochim. Acta 38 (**1993**) 349

[18] K. Naoi,M. Lien, H. Smyrl, *J. Electroche. Soc.*, 138 (**1991**) 440

[19] H. Sung, H. So, W. Paik, *Electrochim. Acta*, 39 (**1994**) 645

[20] H. Sung, T. Lee, W. Paik, *Synth. Metals* 69 (**1995**) 485

[21] I. F. Perepichka, M. Besbes, E. Levillain, M. Salle, J. Roncali, *Chem. Mat.*, **2002**, *14*, 449T.

[22] Mohamed Besbes, Galle TrippØ, Eric Levillain, Miloud Mazari, Franck Le Derf, Igor F. Perepichka, Aïcha Derdour, Alain Gorgues, Marc SallØ, Jean Roncali, *Adv. Mater.*, **2001**, *13*, 1249

[23] F. Otero, S. A. Cheng, F. Huerta, *Journ. Phys. Chem. B*, **2000**, *104,* 10528-10533

[24] ZHANG, Xiao-Feng, LIN, Shen, LUO, Geng-Geng, LIU, Chun-Lian, *Chinese Journ. of Chem.*, **2007**, *25*, 323.

[25] T. Yohannes , J.C. Carlberg, 0. Inganiis, T. Solomon, *Synth. Met.*, **1997**, *88*, 15.

[26] P. Schottland, K. Zong, C. L. Gaupp, B. C. Thompson, C. A. Thomas, I. Giurgiu, R. Hickman, K. A. Abboud, J. R. Reynolds, *Macromolecules*, **2000**, *33*, 7051

[27] L. Groenendaal, G. Zotti, F. Jonas, *Synth. Met.*, **2001**, *118*, 105.

[28] CA Thomas, **2001**,PhDThesis.

[29] F.M. Smits, *The Bell Syst. Tec. Journ.*, **1958**, 712.

[30] N.S. Allen, K. S. Murray, R. J. Fleming, B.R. Saunders, *Synthetic Metals* 81 (**1997**) 237-247

[31] C. J. Gómez-García, E. Coronado, P. Ghez-Romero, N. Casafi-Pastor, *Inorg. Chem.***1993**, *32, 3378.*

[32] Richard G. Finke, Michael W. Droege, Peter J. Domaille, *Inorg. Chem.* **1987**, *26, 3886*.

CHAPTER 6

PEDOT thin films doped with magnetic nanostructures ([Fe^{II}Cr^{III}(ox)$_3$]$^-$ anions)

6.1 INTRODUCTION

Excellent examples of molecular magnetic conductors have been obtained by using bis(etilenditia)tetratiafulvalene (BEDT-TTF) as organic donor, giving rise to conductivity, and charge-compensating bimetallic oxalato complexes [M^{II}M^{III}(ox)$_3$]$^-$ (M^{II} = Mn, Co, Ni, Fe, Cu; M^{III} = Fe, Cr), incorporating ferromagnetic properties. These polymeric anions exhibit a honeycomb layered structure in which the metal ions interact through superexchange. (Figure 6.1)
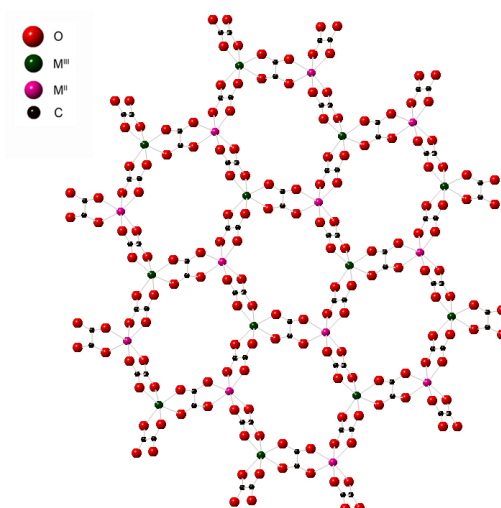

Figure 6.1: honeycomb layers exhibited by M^{II}M^{III}(ox)$_3$]$^-$ bimetallic oxalato complexes

Particularly, (BEDT-TTF)$_3$[MnCr(ox)$_3$], synthesized by Coronado et al, is the first example of molecular ferromagnetic metal. [1] Molecular oxalate complexes have also shown the possibility of generating paramagnetic superconductors when combined with BEDT-TTF. [2][3] In fact, Day et al. [4] reported on (BEDT-TTF)$_4$[(H$_2$O)Fe(ox)$_3$]·C$_6$H$_5$CN, that is the first paramagnetic superconductor. The importance and the potentiality of oxalate ligand leap off the page. For that reason, hetero bi-metallic oxalate complexes have been chosen as ferromagnetic carriers embedded into a conducting polymeric matrix for the preparation of new hybrid materials.

In this chapter these anionic complexes are combined with the conducting polymer poly(3,4-ethylenedioxythiophene) PEDOT. The incorporation of magnetic anions into the positively-charged chains of PEDOT, should occur simultaneously to monomer oxidation. The *in-situ* chemical oxidation of EDOT monomers can be easily induced by ionic oxidants like Fe(III), Mn(IV) or similar metal ions in a suitably high oxidation state.[5] Among them, the Fe(III) ion has been selected in this work.

The synthesis of PEDOT doped films has been carried out by adding a solution containing Fe(III) and [Cr(III)(ox)$_3$]$^{3-}$ to EDOT. In these conditions Fe(III) ion is reduced to Fe(II) while EDOT is oxidized and polymerization starts. This *in-situ* chemical oxidation of EDOT in Fe(III)[Cr(III)(ox)$_3$] neutral solution allows avoiding the presence of undesired ions that can be detrimental for the final composition and physical properties of the obtained material.

Two different Fe(III):EDOT ratios have been used to prepare different hybrid materials with the aim to compare their physical properties. These hybrid materials have been characterized by SEM and HR-TEM and their magnetic and electrical properties have also been studied.

6.2 RESULTS AND DISCUSSION

6.2.1 Synthesis of [Fe(II)Cr(III)(ox)$_3$]$^-$-doped PEDOT

Fe(III)[Cr(III)(ox)$_3$] can be obtained in *n*-ButOH solution upon direct reaction between Ag$_3$[Cr(ox)$_3$] and FeCl$_3$·6H$_2$O (1:1 Fe:Cr ratio) followed by precipitation of AgCl. Upon addition of EDOT to this solution, a deep blue colored material, typical of oxidized PEDOT, appears. By changing the ratio Fe(III) : EDOT, two different materials have been obtained: **(6)**, Fe(III) : EDOT ratio of 1:1 and **(7)** Fe(III) : EDOT ratio of 1:10. (see Experimental Section)

6.2.2 Physical Measurements

Due to the fast process of polymerization, it has been possible to characterize only the final solid material.

6.2.2.1 *SEM/EDX*

SEM images have been recorded for **(6)** and **(7),** as shown in Fig. 6.2 and Fig. 6.3, respectively. The morphology of both films is very similar and features holes that deform the surface, probably due to rapid solvent evaporation and quick polymerization reactions.

Contrary to some other materials reported in the literature [6] in which monomer oxidation occurs in presence of H_2O_2, the materials **(6)** and **(7)** are slightly flat and do not have a completely amorphous structure. (see Figure 6.2 and 6.3)

The EDX analyses confirm the Fe(III):EDOT ratio of 1:1 for **(6)** and around 1:10 for **(7)**. EDX analyses are reported in Appendix B. In Fig. 6.2 (right), the appearance of the Cl peak reveals the presence of a small amount of $FeCl_3 \cdot 6H_2O$ residue, added during the synthesis of the $Fe(III)[Cr(III)(ox)_3]$ solution.
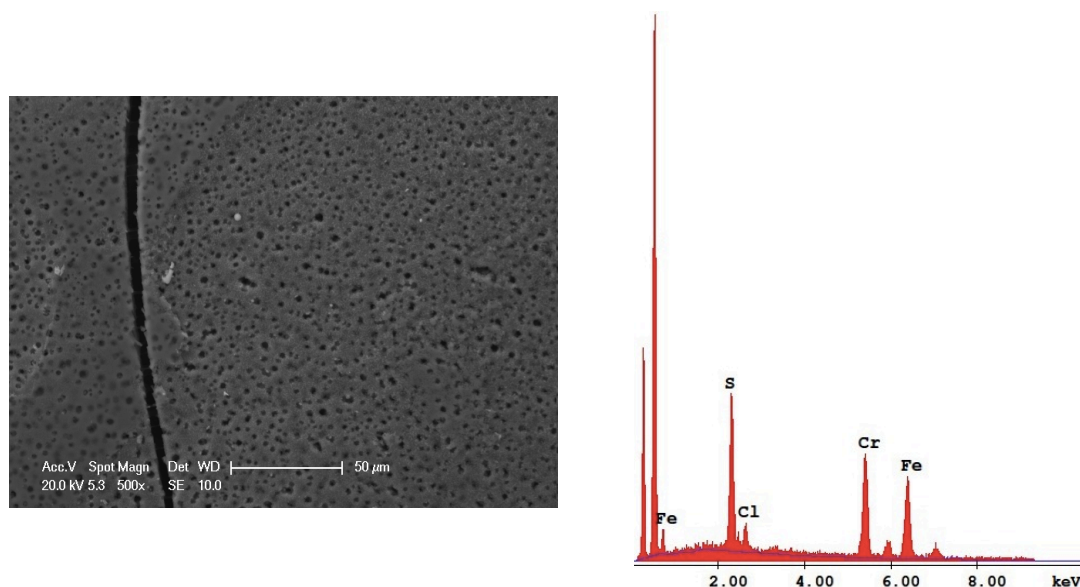

Fig. 6.2: SEM micrography of $Fe(II)[Cr(III)(ox)_3]^-$ doped PEDOT **(6)** (50 μm, left) and EDX analysis (right).
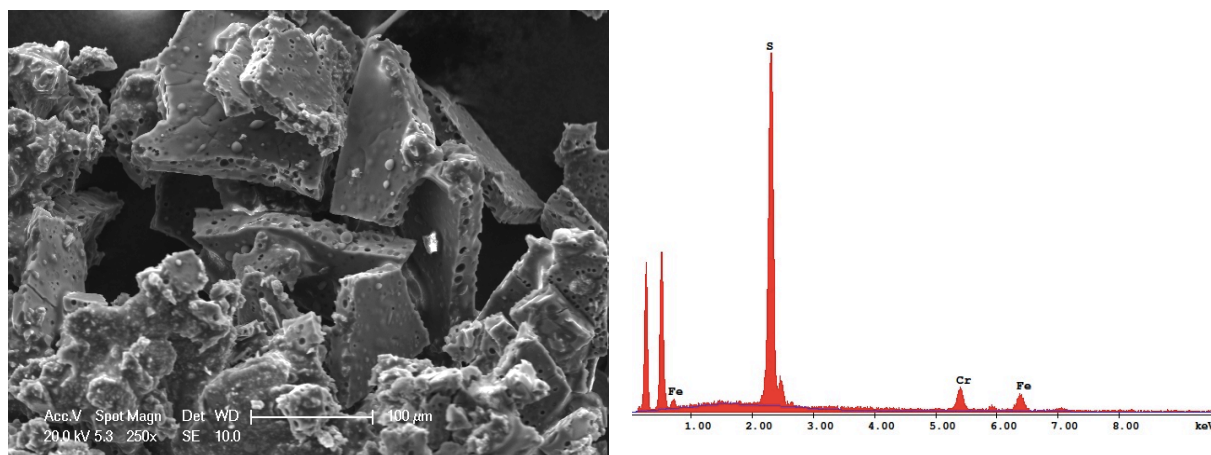
Fig. 6.3: SEM micrography of Fe(II)[Cr(III)(ox)$_3$]$^-$ **(7)** (100 μm, left) and EDX analysis (right).

In Fig. 6.3, a SEM image showing the inner morphology of **(7),** is reported. It is evident the presence of holes inside the material that may have some influence in the material properties, as described in the following paragraphs.

6.2.2.2 *HR-TEM*[*]

Few drops of freshly synthesized **(6)** were placed in a HR-TEM grid and left undergo complete solvent evaporation by heating at ~150 °C for half an hour,. The grid had been completely dried under vacuum and stored in a dry box, at r.t.
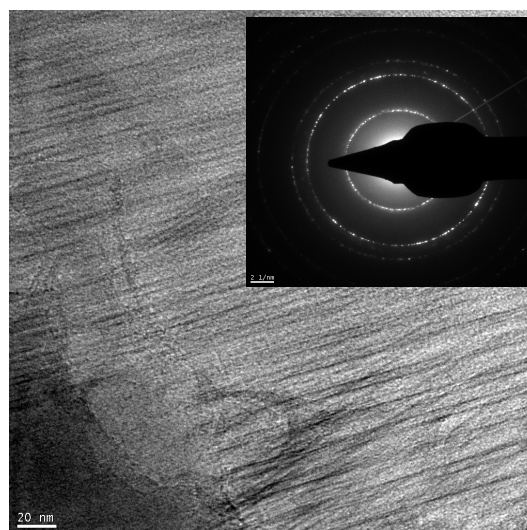

Fig. 6.4: HR-TEM image **(6)** (20 nm). The inset shows the electron diffraction of the sample.

---

[*] HR-TEM measurements were performed with the help of Gonzalo Abellán, ICmol, Valencia, (Spain).

Fig. 6.4 shows some straight and equally separated lines in the HR-TEM image of (**6**). Some of them are darker and present different orientations as they correspond to layers located at different depths. Electronic Diffraction reveals that the material is polycrystalline. The EDX of the deposited material for HR-TEM shows that the Cr:Fe ratio is close to the theoretical 1:1, while S concentration (due to EDOT) is very low compared to that recorded with EDX for the same sample (Fig. y.3, right). This loss of EDOT may be due to the vacuum treatment necessary to perform the HR-TEM measurements.

For (**7**), HR-TEM measurements do not reveal the same kind of structures reported in Fig. 6.4. Fig.6.5 shows a mapping for three heavy elements (S, Fe and Cr).
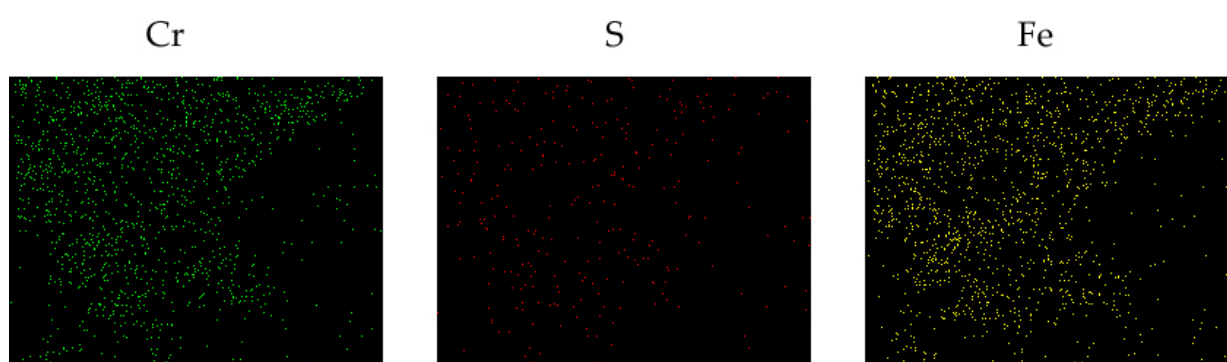

Fig. 6.5: HR-TEM element mapping for (**7**) (50 nm)

Fig. 6.6 shows the HR-TEM of the same material section in which the element mapping has been done. By comparing both images (Fig 6.6, left and right), it is possible to recognize the same material shape in the element mapping.
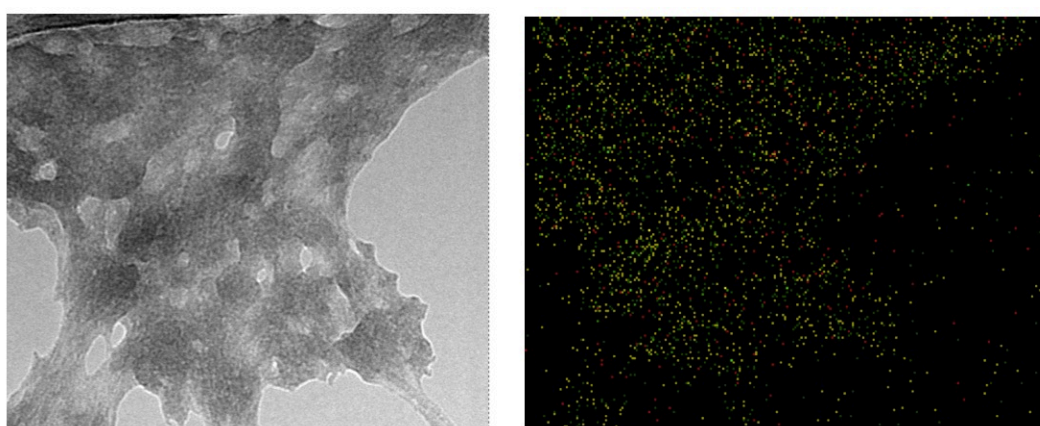

Fig. 6.6: HR-TEM of freshly synthetized (**2**) (50 nm) section and the complete element mapping in a dark field

Even in this case, the EDX analysis reveals a low concentration of S. The great volatility of EDOT could justify this behavior.

6.2.2.3 *Magnetic Measurements*

Magnetic measurements have been performed for **(6)** and **(7)**.

The thermal variation of the $\chi_m T$ product for compound **(6)** shows a room temperature value of ca. 4.8 emu.K.mol^{-1} (Fig. 6.7), very close to the expected value for a Cr(III) and a Fe(II) isolated ions (the expected value for g = 2 is 4.875 emu.K.mol^{-1}). When the temperature is lowered $\chi_m T$ shows an initial decrease to reach a minimum at ca. 20 K followed by a sharp increase al lower temperatures to reach a maximum at ca. 7 K. Below ca. 7 K, the $\chi_m T$ product shows a sharp decrease to reach a value of ca. 3.2 emu.K.mol^{-1} at 2 K (Fig. 6.7). The initial decrease observed in $\chi_m T$ as the temperature is lowered, differs from the behavior observed in other compounds with the [FeCr(ox)$_3$]$^-$ layer, where there is a constant value and an increase at lower temperatures as a result of a ferromagnetic Fe-Cr coupling through the oxalato bridge. This discrepancy may be explained by the possible partial substitution of Cr(III) by Fe(III) that would lead to a ferrimagnetic Fe(III)-Fe(II) coupling, as observed in the [Fe(II)Fe(III)(ox)$_3$]$^-$ lattice. [7] [8] [9]
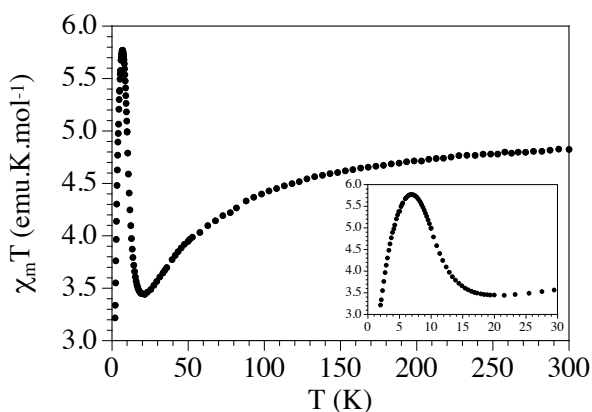

Figure 6.7: Thermal variation of the $\chi_m T$ product for **(6)**. Inset shows the low temperature region.

In order to confirm the presence of a long range magnetic ordering in **(6)** AC magnetic susceptibility measurements (Fig. 6.8) have been performed. These measurements shows a maximum in both, the in-phase (χ_m') and the out-of-phase (χ_m'') signals, confirming the presence of a long range order, as observed in other salts with the [FeCr(ox)$_3$]$_-$ lattice. [7] [8] [9] [10] Both signals, χ_m' and χ_m'' are unusually frequency-dependent. In fact, the Arrhenius plot, Ln ν vs. 1/T, of the frequency dependence of the temperature of the maximum in χ_m'' (Fig. 6.8, right) shows a linear behavior with

an activation energy of 109 K ($Ln \, \nu = \nu_0 - E_a/kT_{max}$), a similar value to those found in other ferromagnetic two dimensional systems with domain wall movement [11] [12] [13] [14] and too low for a spin glass or spin-glass-like behavior (where the values are at least one order or magnitude higher). [15] Nevertheless, the domain wall movement has to be excluded since this process occurs after the ferromagnetic order is established and in (**6**) we do not observe an ordering temperature above the χ_m'' peak. A more plausible explanation is the presence of a superparamagnetic behavior with an activation energy of 109 K, close to that observed in other single molecule magnets. [16] [17] [18] This superparamagnetic behavior would appear as a consequence of the small size of the nanoparticles. Note also that a small contribution to this value may arise from the already mentioned possible Fe(III)/Cr(III) or Fe(III)/Fe(II) disorder. In fact, in other examples with this [FeCr(ox)$_3$]$^-$ lattice) some Fe(III) ions may replace some Cr(III) ions since Fe(II) is easily oxidized to Fe(III) by atmospheric O$_2$. The ordering temperature of the ferromagnetic [FeCr(ox)$_3$]$^-$ layer, T_c, measured as the temperature at which the χ_m'' signal becomes non-zero is close to 9 K. This temperature is lower than the typical one reported for the [FeCr(ox)$_3$]$^-$ lattice (where the T_c is ca. 12-13 K) [7] [8] [9] [10] and suggests the presence of some disorder probably due to a partial substitution of Cr(III) by Fe(III) or even some Fe(II) by Fe(III) with a loss or a reduction of one EDOT cation per substituted Fe(II).
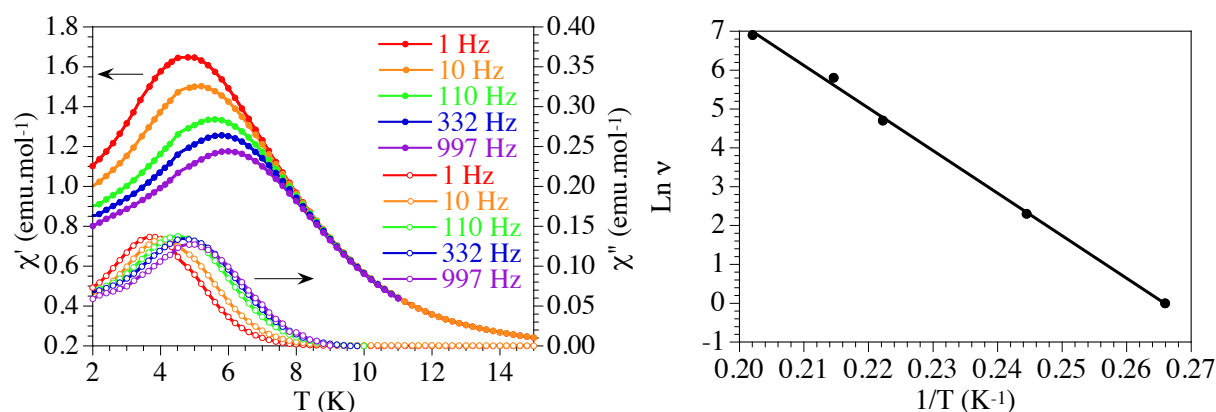

Figure 6.8: (*left*) In-phase (χ_m', filled symbols, left scale) and out-of-phase (χ_m'', empty symbols, right scale) AC signals at different frequencies for (**6**) (Fe:S ~ 1:1): (*right*) Arrhenius plot of the frequency dependence of the maximum on the χ_m'' signal

The presence of a ferromagnetically ordered [Fe(II)Cr(III)^{III}(ox)$_3$]$^-$ sub-lattice is further confirmed by the isothermal magnetization at 2 K that shows a hysteresis with a coercive field of ca. 36 mT (360 G) (Fig. 6.9). Note that this coercive field is similar to

those found in the (C$_4$H$_9$)$_4$N$^+$ and FeCp$_2$* salts with the same [Fe(II)Cr(III)(ox)$_3$]$^-$ sublattice (320-330 G). [7] [8] [9] [19]
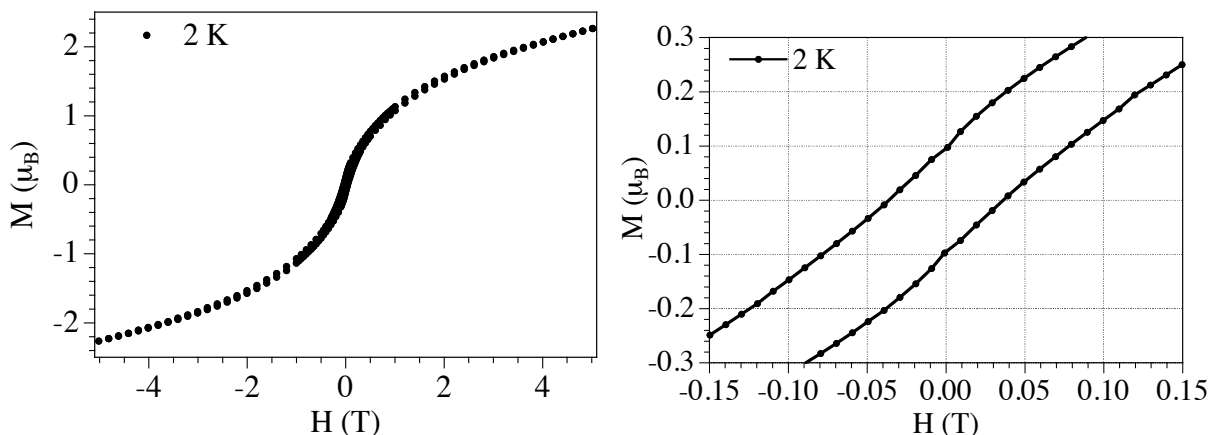

Figure 6.9 (left) Isothermal magnetization of (**1**) at 2 K. **(right)** The low field region.

Compound (**7**) shows a similar behavior to that of the other known examples containing the [FeCr(ox)$_3$]$^-$ 2D net. The χ_mT product at r. t. is very close to the expected value (ca. 4.875 emu.K.mol^{-1}) and this means that the molecular weight corresponding to a ratio 10:1 is correct (see Fig. 6.10). When the temperature is lowered (**7**) shows a constant value down to ca. 20 K. Below this temperature χ_mT shows a sharp increase to reach a maximum at ca. 8 K followed by a sharp decrease to reach a value of ca. 3.2 emu.K.mol^{-1} at 2 K. This behavior is very similar to those observed in other [FeCr(ox)$_3$]$^-$ lattices and confirms the presence of ferromagnetic Cr-Fe interactions in compound (**7**), as observed in other compounds with the same [FeCr(ox)$_3$]$^-$ lattice. [7] [8] [9] [10] [19]
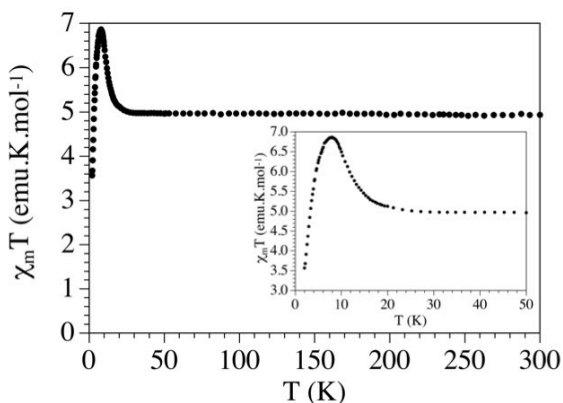

Figure 6.10: Thermal variation of the χ_mT product for (**7**). Inset shows the low temperature region.

Also for **(7)**, AC measurements show a maximum in the in phase signal and an out-of-phase signal for temperatures below ca. 9 K. (Fig. 6.11) This means that this sample also presents a ferromagnetic long-range order with $T_c \approx 9$ K. Usually, the χ_m'' peak should be frequency-independent but in this sample (as in **(6)**) there is a shift in the AC signal that can be attributed to the presence of some disorder and to a superparamagnetic behavior of the nanoparticles. Nevertheless, in compound **(7)** the fit to an Arrhenius law gives a higher activation energy of 227 K, which cannot be attributed to the movement of the domain walls but rather to a superparamagnetic behavior of the nanoparticles of $[FeCr(ox)_3]^-$.
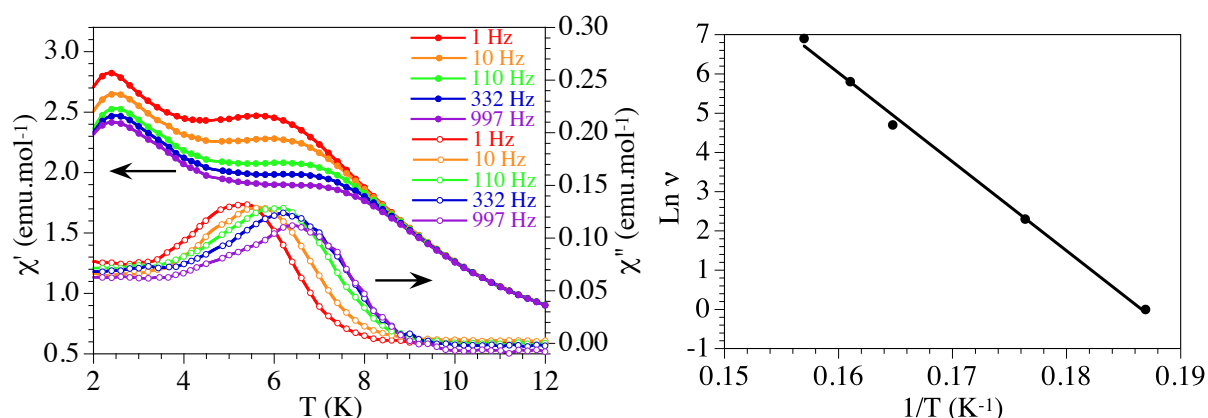

Figure 6.11: (*left***)** In-phase (χ_m', filled symbols, left scale) and out-of-phase (χ_m'', empty symbols, right scale) AC signals at different frequencies for **(7)** (Fe:S ~ 1:10). (***right***) Arrhenius plot of the frequency dependence of the maximun on the χ_m'' signal

The presence of a ferromagnetically ordered $[Fe^{II}Cr^{III}(ox)_3]^-$ sub-lattice is also further confirmed by the isothermal magnetization at 2 K that shows a hysteresis with a coercive field of ca. 21 mT (210 G) (Fig. 6.12), slightly below the one observed in compound **(6)**. The differences in the coercive field are probably due to differences in the relaxation times of both compounds as a consequence of the differences in the polymeric environments in both compounds. It could also be due to a difference in the size of the nanoparticles, since the coercive field is strongly dependent on the size of the superparamagnetic nanoparticles.
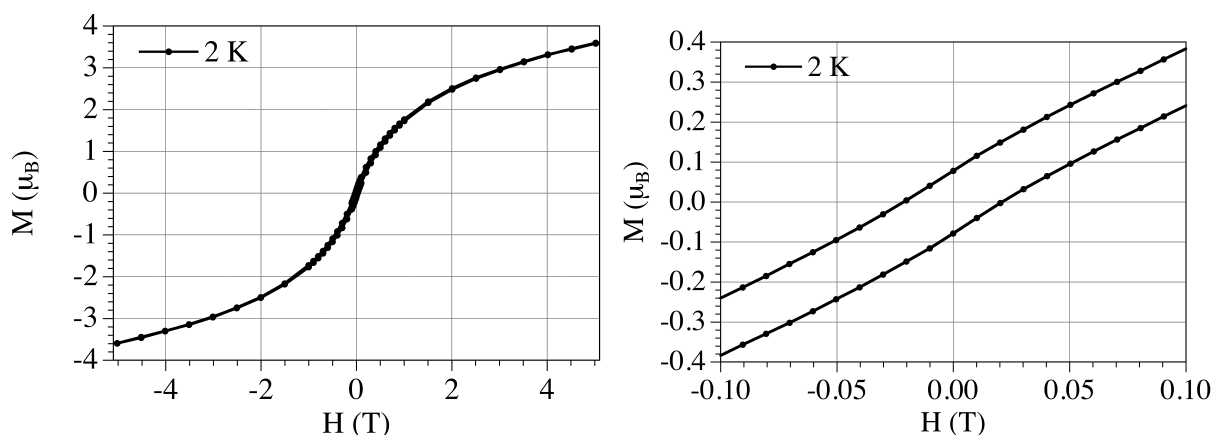
Figure 6.12 (*left***)** Isothermal magnetization of (**7**) at 2 K. (***right***) The low field region.

6.2.2.4 *Processing by Spin Coating*

(6) and (7) have been processed byspin coating over a thin flexible glass. Then, the glass has been heated to allow solvent evaporation. Film thickness has been estimated to be about 300 nm and 150 nm for (**6**) and (**7**) samples, respectively. The inhomogeinity of the obtained films is probably due to the quick polymerization of PEDOT. In fact, one observes transparent and light blue color parts.

6.2.2.5 *Conductivity Measurements*

The electrical conductivity of the films obtained with the spin-coating technique was measured with the four contacts method as a function of the temperature. These measurements show that compound (**6**) is a good electrical conductor, with a r.t. conductivity of 0.012 S.cm^{-1} although it presents a reversible transition to an insulator state at ca. 250 K in the cooling scan and ca. 270 K in the warming scan (Fig. 6.13). Unfortunately, this transition precludes the study of the possible influence of the magnetic order on the conducting properties at low temperatures. Since the transition presents a hysteresis of ca. 20 K and it presents some re-entrant steps in the cooling and warming scans, it is probably due to some localization process in the almost completely changed polymeric chain (since the high Fe:S ratio indicates that almost all the EDOT monomers are fully oxidized). In order to avoid this localization process, it is necessary to increase the EDOT:anion rate, as was done in compound (**7**).
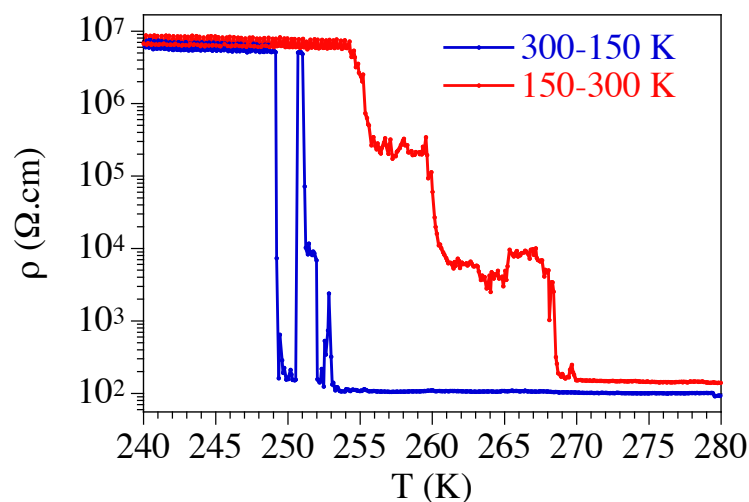
Figure 6.13. Thermal variation of the dc electrical conductivity for a spin coated film of compound (**6**) of 320 nm thickness

Compound (**7**) is a worse electrical conductor, with a r.t. conductivity of 2.9×10^{-5} S.cm^{-1}, probably due to the much lower charge density in the polymeric matrix (one oxidized EDOT monomer every ca. 10). When the temperature is decreased the resistivity increases in a classical semiconducting behavior (Fig. y.14, left). Thus, the Arrhenius plot (Ln ϱ vs. 1/T) shows a straight line whose slope gives an activation energy of 170 meV (Fig. y.14.right).
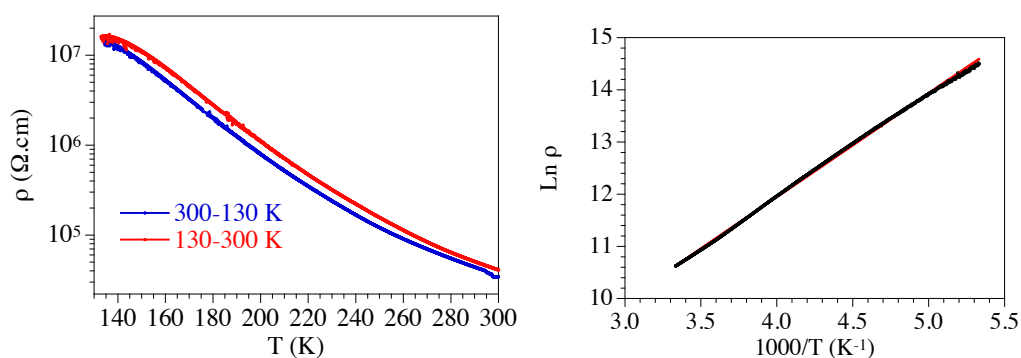

Figure 6.14. (*left*) Thermal variation of the dc electrical conductivity for a spin coated film of (**7**). (*right*) Arrhenius plot (Ln ϱ vs. 1/T) for the same film. Solid line shows the corresponding fit to the Arrhenius law.

Unfortunately, the relatively low r.t. conductivity and the high activation energy lead to a very high resistance value at low temperatures, above the detection limit of our equipment, precluding, as in (**6**), a study of the possible influence of the magnetic ordering of the [FeCr(ox)$_3$]$^-$ sub-lattice on the conducting properties of the polymeric matrix.

6.3 Conclusions

By *in-situ* chemical oxidation of EDOT monomers, two new hybrid materials have been synthesized, that are only formed by doped chains of oxidized PEDOT and [Fe(II)Cr(III)(ox)$_3$]$^-$ anions. These compounds represent the first examples in which these magnetic anions are combined with PEDOT. HR-TEM reveal the presence of nanostructures of 2D polycrystalline systems. Magnetic measurements show ferromagnetic coupling due to Fe(II)-Cr(III) ions and the presence of some disorder and a superparamagnetic behavior in the hybrid magnetic polymers. Conductivity experiments reveal a reversible transition to an insulator state around 250 K for the material prepared with an EDOT:anion ratio of ca. 1:1 and a classical semiconducting behavior for the material prepared with an EDOT:anion ratio of ca. 10:1. The transition in the first case can be attributed to a reversible localization process in the highly charged PEDOT polymer. The higher r.t. conductivity values for the more oxidized film agree with the expected behavior. These materials show that by simply playing with the EDOT:anion ratio it is possible to modulate the electrical properties of the resulting material.

In the light of these promising results, efforts to improve the properties of these materials should be addressed to: 1) achieving a better chemical control over the polymerization process in order to slow it down for obtaining materials with better homogeneity and 2) playing with the Fe(III)/EDOT ratio in order to obtain materials with improved conducting properties.

6.4 Experimental Section

K$_2$C$_2$O$_4$ · H$_2$O, H$_2$C$_2$O$_4$ · 2 H$_2$O, K$_2$CrO$_7$, 3,4-ethylenedioxythiophene (EDOT), AgNO$_3$, FeCl$_3$·6H$_2$O were purchased from Aldrich and used as received, including HPLC grade CH$_3$CN (ACN).

6.4.1 Synthesis and characterization

Synthesis of K$_3$[Cr(ox)$_3$]

The synthesis of K$_3$[Cr(ox)$_3$] was performed according to the procedure reported in the literature. [20] 2.3 g (1.2 · 10^{-2} mol) of K$_2$C$_2$O$_4$ · H$_2$O were added to 5.5 g (6.1 · 10^{-2} mol)

of $H_2C_2O_4 \cdot 2\ H_2O$ dissolved in 80 mL of distilled boiling water. When the two compounds were completely dissolved, 1.9 g ($6 \cdot 10^{-3}$ mol) of K_2CrO_7 were carefully added. The solution turned to dark green and was left cooling overnight. Prismatic dark crystals were obtained and collected by filtration.

Synthesis of Fe(III)[Cr(III)(ox)$_3$] solution

1.0 g (6 mmol) of $AgNO_3$ were added to 40 mL of an aqueous solution containing 1.0 g (2 mmol) of $K_3[Cr(ox)_3]$ (Ag:Cr ratio of 3:1). After one night, deep dark crystals of $Ag_3[Cr(ox)_3]$ were collected and dried under vacuum. Afterwards, 1.40 g (2 mmol) of the obtained product were put in a beaker containing 0.33 g (2 mmol) of $FeCl_3 \cdot 6H_2O$ (1:1 Fe:Cr ratio) and 5 mL of *n*-ButOH. AgCl precipitate was filtered off. The resulting brown solution containing the Fe(III)[Cr(III)(ox)$_3$] salt, was left at r.t.

Synthesis of PEDOT doped with Fe(II)[Cr(III)(ox)$_3$]˙ anions

0.54 mL of Fe(III)[Cr(III)(ox)$_3$] (0.4 M) solution were added to 0.02 mL of EDOT monomer in Fe(III):EDOT ratio of 1:1 **(6)** or to 0.20 mL of EDOT monomer in Fe(III):EDOT ratio of 1:10 **(7)**. Polymerization started immediately and after 10-20 minutes all reagents reacted to yield a blue doped PEDOT material. The product was then put in a watch glass, heated at ca. 150°C for complete evaporation of *n*-ButOH, stored under vacuum for a night and then stored at 4 °C.

6.4. 2 Physical Measurements

Electron Microscopy

SEM/EDX: Scanning electron microscopy (SEM) experiments have been carried out using Philips SEM-XL30 equipped with an EDAX microprobe, used for determining metallic atomic composition of samples.

HR-TEM: High Resolution - Transmission Electronic Microscopy (HR-TEM) experiments have been carried out using TECNAI G2 F20 (FEI) with 200kV field emission (FEG) and 0.18 nm resolution. Samples were prepared by dropping of fresh prepared H_2O/Acetone (1:3) solution of the dispersed particles over a copper grid (Lacey Formvar/Carbon, 300 mesh, copper approx. grid hole size: 63 μm). Samples

were tested when they were dried. The digital analysis of the HR-TEM micrographs was done using Digital Micrograph Software.

Electron diffraction pattern and spectroscopic technique as EDS and Mapping were performed using this apparatus.

Magnetic Measurements

The magnetic susceptibility measurements were carried out in the temperature range 2-300 K with an applied magnetic field of 0.1 T on a sample of compound **(6)** and **(7)** samples with a Quantum Design MPMS-XL-5 SQUID susceptometer. The isothermal magnetization was performed on the same sample at 2 K with magnetic fields up to 8 T. The susceptibility data were corrected for the sample holder previously measured using the same conditions.

Spin Coating

Spin coating experiments were performed by using Chemat Technologies model KW-4A apparatus. Freshly prepared solution of **(6)** and **(7)** samples were spin-coated (1000 rpm, 1 minute) onto thin flexible glass (prior to deposition, the glass substrates were extensively cleaned, using chemical and UV-ozone methods) and the layers were subsequently annealed at 150°C on a hotplate for 10 min, resulting in a layer thickness of approximately 300 nm and 150 nm for **(6)** and **(7)** samples, respectively. After spin-coating, the homogenous and with a light blue color films were dried and transferred into a dry box.

Conductivity Measurements

D.C. conductivity measurements over the range 150–300 K were performed using the four contacts method for spin-coated **(6)** and **(7)** samples. Contacts between the film and platinum wires (25 mm diameter) were made using graphite paste. The samples were measured in a Quantum Design PPMS-9. The cooling and warming rate was 1 K min^{-1} and the results were, within experimental error, identical in the cooling and warming sweeps.

REFERENCES

[1] Coronado, E., Galán-Mascarós, J.R., Gómez-García, C.J. and Laukhin, V.N. (2000). *Nature*, **408**, pp. 447-449

[2] M. Clemente-Leon; E. Coronado; C. Marti-Gastaldo; Romero, *Chem. Soc. Reviews* **2011** (40) 473-497 and references therein

[3] E. Coronado, S. Curreli, C. Giménez-Saiz, C. J. Gómez-García, *Inorganic Chemistry*, **2011** (51) 1111–1126 and references therein

[4] Graham, A.W., Kurmoo, M. and Day, P. (**1995**), *J. Chem. Soc., Chem. Commun.*, pp. 2061-2062

[5] "PEDOT, Principles and Applications of an Intrinsically Conductive Polymer", A. Elschner, S. Kirchmeyer, W. Lövenich, U. Merker, K. Reuter, **2011**, CRC Press

[6] J. Vaillant, M. Lira-Cantu, K. Cuentas-Gallegos, N. Casañ-Pastor, P. Gómez-Romero, *Progress in Solid State Chemistry*, **2006**, (34) 147-159

[7] M. Clemente-León, E. Coronado, J. R. Galán-Mascarós, C. J. Gómez-García *Chem. Commun.* **1997**, 1727-1729;

[8] E. Coronado, M. Clemente-León, J. R. Galán-Mascarós, C. Giménez-Saiz, C. J. Gómez-García, E. Martínez-Ferrero *Dalton Trans.* **2000**, 3955-3961;

[9] E. Coronado, J. R. Galán-Mascarós, C. J. Gómez-García, J. Ensling, P. Gütlich *Chem. Eur. J.* **2000**, *6*, 552-563]

[10] H. Tamaki, Z. J. Zhong, N. Matsumoto, S. Kida, M. Koikawa, N. Achiwa, Y. Hashimoto, H. Okawa *J. Am. Chem. Soc.* **1992**, *114*, 6974;

[11] E. Coronado, C. J. Gómez-García, A. Nuez, F. M. Romero, E. Rusanov, H. Stoeckli-Evans *Inorg. Chem.* **2002**, *41*, 4615-4617;

[12] F. Bellouard, M. Clemente-Leon, E. Coronado, J. R. Galan-Mascaros, C. J. Gómez-García, F. Romero, K. R. Dunbar *Eur. J. Inorg. Chem.* **2002**, 1603-1606;

[13] S. Triki, J. Sala-Pala, F. Thetiot, C. J. Gómez-García, J. C. Daran *Eur. J. Inorg. Chem.* **2006**, 185-199;

[14] E. Coronado, C. J. Gómez-García, A. Nuez, F. M. Romero, J. C. Waerenborgh *Chem. Mater.* **2006**, *18*, 2670-2681]

[15] J. A. Mydosh, *Spin Glasses: an experimental introduction*, Taylor & Francis, London, **1993**.]

[16] R. Sessoli, A. K. Powell *Coord. Chem. Rev.* **2009**, *253*, 2328-2341;

[17] D. Gatteschi, R. Sessoli, *Angew. Chem. Int. Ed.* **2003**, *42*, 268-297;

[18] D. Gatteschi, A. L. Barra, A. Caneschi, A. Cornia, R. Sessoli, L. Sorace *Coord. Chem. Rev.* **2006**, *250*, 1514-1529]

[19] E. Coronado, J. R. Galán-Mascarós, C. J. Gómez-García, R. Burriel *J. Magn. Magn. Mater.* **1999**, *196-197*, 558-560;

[20] J.C. Bailar Jr, E. M. Jones, H. S. Booth, M. Greennert, *Inorg. Synth.,* **1939**, (1), 35-38

CHAPTER 7

PEDOT thin films doped with magnetic nanoparticles (Prussian Blue Analogues)

7.1 INTRODUCTION

Much research effort has been directed towards the development of methodologies and processes for the incorporation of magnetic nanoparticles into polymeric matrices. Of particular interest is the integration of magnetic nanoparticles with conducting polymers since the resulting nanocomposites may possess unique magnetic, electrical, and optical properties. [1] [2] [3]

Such nanomaterials can find applications in electromagnetic interference shielding, electrochromic devices, sensing and actuating technologies, nonlinear optical systems, and molecular engineering of nanomotors.

The aim of this research is to integrate magnetic nanoparticles into a polymeric conducting matrix. To do that nanoparticles of Prussian Blue analogues (PBA) (for example NiII-FeIII cyanide bridged nanoparticles) have been combined into matrices of electrically conducting films of PEDOT [poly(3,4-ethylenedioxythiophene)]. These nanoparticles have shown to be of interest in molecular magnetism as they exhibit interesting magnetic or photomagnetic properties, which can be chemically tuned by varying their composition and size. [4] - [10] Furthermore, they are not aggregating in solution as they are negatively charged.

The synthesis of magnetic nanoparticles of PBA having sizes of approximately 4 nm and exhibiting single-domain superparamagnetic behavior when they are diluted in a non-conducting polymer matrix, has recently been described in literature. [11]

Taking advantage of the negative charge of these nanoparticles, electropolymerization of EDOT monomers can be carried out in a solution containing these nanoparticles as charge-balancing anions to afford new PEDOT-based hybrid materials, as discussed in this Chapter. Sample characterization, presented in this work, include morphological investigation (HR-TEM, SEM, EDX, DLS) as well as the study of magnetic and electrical

properties down to low temperatures, including magnetoresistance measurements.

7.2 RESULTS AND DISCUSSION

7.2.1 Synthesis and characterization of $Cs_{0.46}Ni[Fe(CN)_6]_{0.94}$ nanoparticles

Ni(II) - Fe(III) cyanide-bridged nanoparticles have been synthesized by mixing two solutions containing $NiCl_2$ and CsCl, and $K_3[Fe(CN)_6]$, respectively. As reported in literature, [11] these NPs **(1 sol)** are stable for several days.

The presence of nanoparticles in solution has been confirmed by the occurrence of the Tyndall Effect[*] (Figure 7.1, left). A hydrodynamic diameter of the particles of about 7 nm has been estimated from Dynamic Light Scattering (DLS) measurements (Figure 7.1, right) on **(1 sol)**, filtered with a 0.2 μm filter.
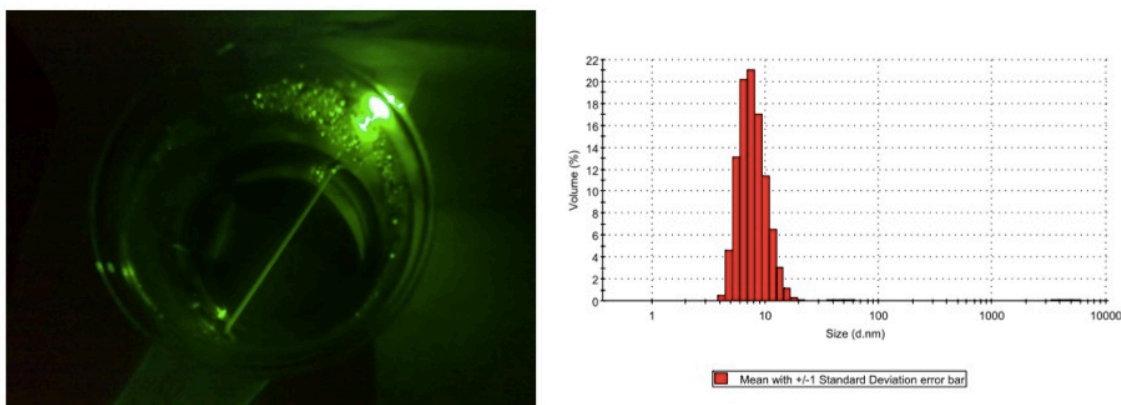

Figure 7.1: Tyndall effect for **(1 sol)** (left); DLS of **(1 sol)** (right).

7.2.1.1 *HR-TEM*

High Resolution Tunnelling Electron Microscopy (HR-TEM) confirms the presence of isolated nanoparticles of ca. 5 nm average diameter (Figure 7.2) similarly to findings already reported in literature. [11]

---

[*] The Tyndall Effect occurs when a collimated light is scattered by 1 – 1000 nm diameter particles. It is caused by reflection of the incident radiation from the surfaces of the particles, reflection from the interior walls of the particles, and refraction and diffraction of the radiation as it passes through the particles.
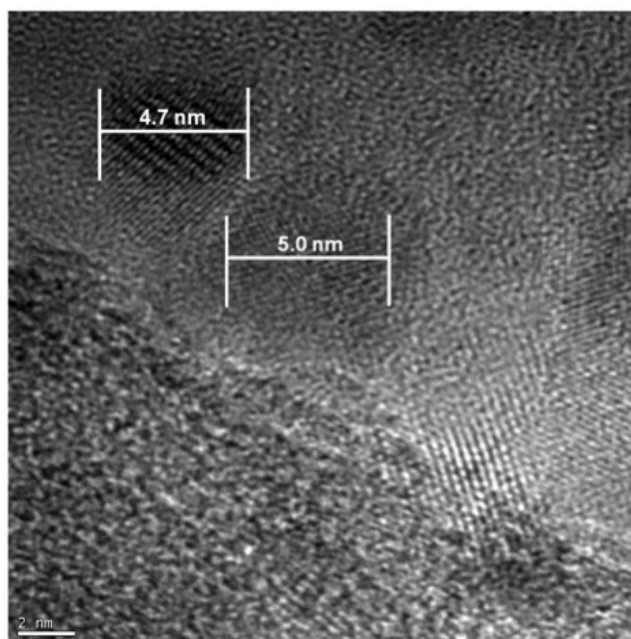
Figure 7.2: HR-TEM of $Cs_{0.46}Ni[Fe(CN)_6]_{0.94}$

Energy-dispersive X-rays (EDX) spectra acquired on the same sample confirm the presence of Cs, Fe and Ni atoms. In particular from the atomic percentage, a ratio Ni : Fe of about 1:1 has been found, as expected.

7.2.3 Synthesis of $Cs_{0.46}Ni[Fe(CN)_6]_{0.94}$ nanoparticles doped PEDOT

As described in Chapter 4, the EDOT poor solubility in aqueous solution can be overcome following different methods. Here, an alternative approach has been discussed: the use of an oxidized PEDOT solution, which is commercially available: PH500® (Clevios™, Heraeus). It is worth noticing that this polymer is highly conductive (it has an electrical conductivity of about 300 S cm^{-1}, with 5% DMSO addition). Synthesis of the doped material has been performed, as described in detail in the Experimental Section, by mixing the **(1 sol)** with a water solution of PEDOT:PSS (PSS = polystyrenesulfonic acid). This mixture **(2 sol)** still presents Tyndall Effect. The solid hybrid material **(8)** has been obtained after acetone addition.

7.2.4 Characterization of $Cs_{0.46}Ni[Fe(CN)_6]_{0.94}$ nanoparticles doped PEDOT

Since **(8)** is insoluble in a large number of solvents, characterization has been only performed on **(2 sol)** before acetone addition.

7.2.4.1 *DLS*

As reported in literature, PH500® is composed of ~ 30 nm diameter particles. [13] Knowing the NPs diameter, the influence of added PEDOT/PSS in the **(1 sol)** solution has been investigated. These polymeric particles disappear in the DLS measurements when the reaction with the magnetic nanoparticles occurs. In fact, DLS measurements of **(2 sol)** solution only show the presence of NPs with a diameter slightly larger than 5 nm. (Figure 7.5, left). In some cases a weak peak due to ~ 20 nm NPs distribution is also observed. This peak is always weak and may be indicative of the presence of few PH500™ unreacted micelles. (see Appendix B)
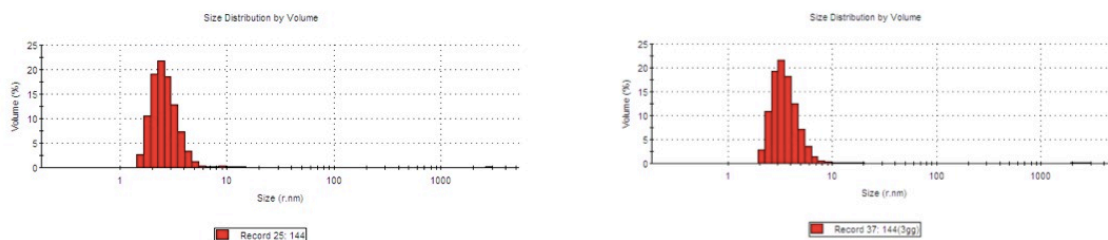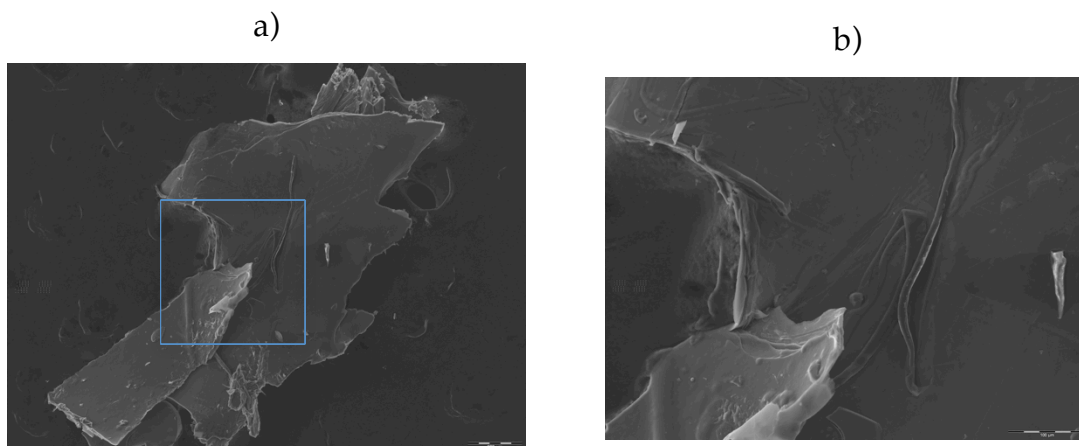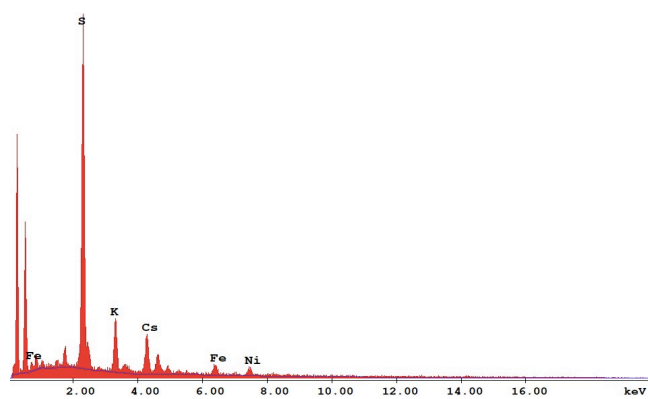

Figure 7.5: DLS size distribution of NPs coated with PH500®, solution **(2 sol)**, freshly prepared (left) and after 3 days aging (right).

7.2.4.2 *SEM/EDX*

The dried flocculates have been analyzed with Scanning Electron Microscopy (SEM) and EDX spectra were recorded. SEM images are shown in Figure 7.6.
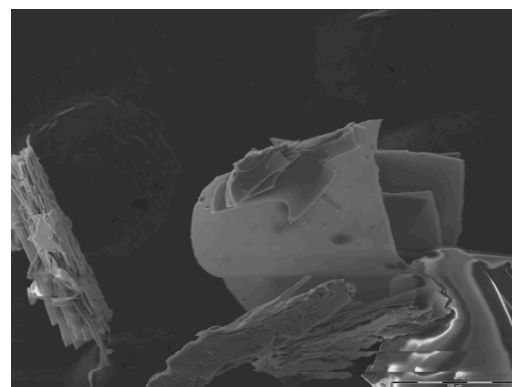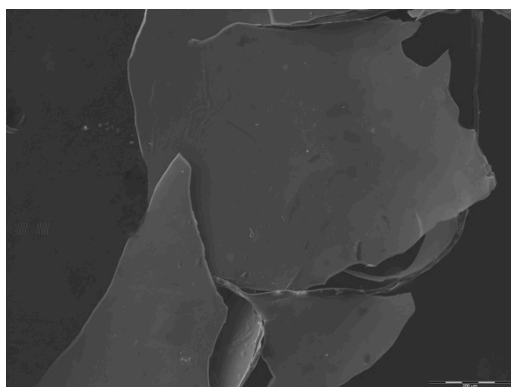
a)   b)

c)

d) e)

f)
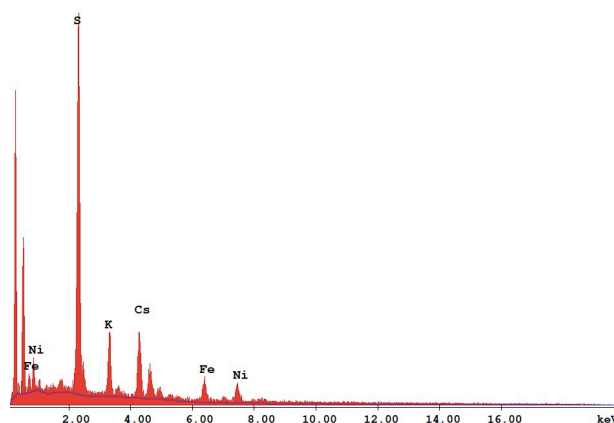
Figure 7.6: SEM of NPs doped PEDOT films obtained under different conditions: **a)** dried flocculate obtained from ~ 8 nm diameter NPs (200 μm); **b)** a closer view of the blue section indicated in figure **a)** (100 μm) and c) EDX spectrum for the same sample shown in figure **a); d), e)** two different images of the film obtained from ~ 7 nm diameter NPs coated with PH500 ® and 5% DMSO and **f)** EDX spectrum.

EDX spectra of all the studied samples show (Figure 7.5 **c)** and **f)**), the presence of PEDOT (S peak) and NPs (Fe and Ni peaks). The ratio Ni:Fe is around 1:1 for all samples. For the first two samples (Figure 7.5 **a)** and **b)**), the ratio S:Ni is

almost 20:1, while for the third doped PEDOT (Figure 7.5 **d)**), the ratio is around 10:1.

The obtained doped polymers show a flat morphology, similar to other examples reported in literature.

7.2.4.3 *HR-TEM*

HR-TEM images have been acquired on a sample prepared by dropping **(2 sol)** on a copper grid. The obtained images are. The dark points appearing in the images shown in Figure 7.6 suggest the presence of NPs.
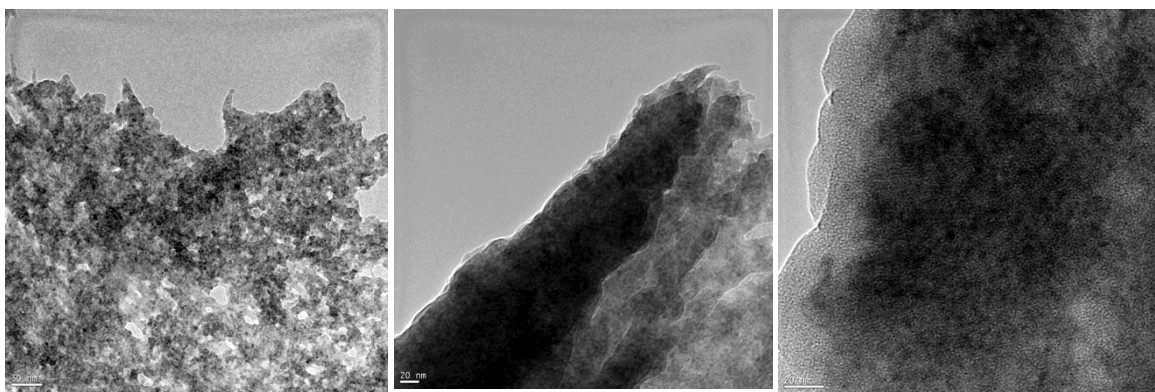

Figure 7.7: HR-TEM images for ~ 8 nm diameter NPs doped PEDOT.

7.2.5 Physical Properties

7.2.5.1 *Magnetic Measurements*

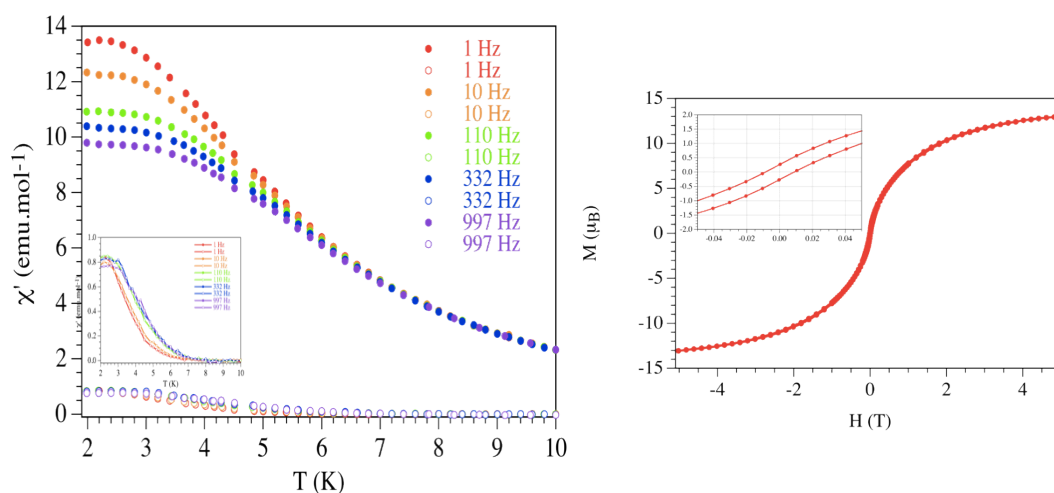Results of magnetic measurements performed on these samples are shown in Figure 7.8.

Figure 7.8: Magnetic measurements for NPs and PEDOT/PSS flocculate **(8)** (Ni:S ~ 3:1): plot ac (left) and dc (right).

For **(8)**, the in-phase (χ') and the out-of-phase (χ'') components are frequency dependent, as shown in Figure 7.8 (left). This behavior is typical of superparamagnetic nanoparticles. The blocking temperature (T_B) is around 7 K. Furthermore, the isothermal magnetization shows a hysteresis with a coercive field of ≈ 90 Gauss. (Figure 7.8, right) These results confirm the presence of the PBA NiFe magnetic nanoparticles in the polymer matrix.
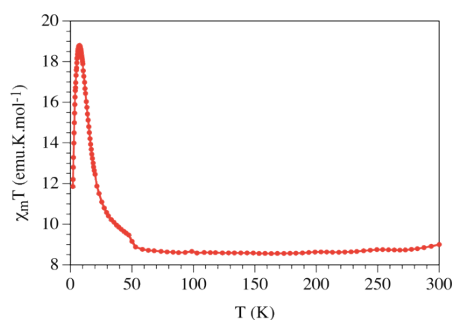
Figure 7.9: $\chi_m T$ vs T graph for the flocculated NPs with PEDOT/PSS.

7.2.5.2 *Processing by Spin Coating*

As mentioned above, the solid NPs doped PEDOT material was insoluble in organic solvents. Then, in order to process the system, a new diluted solution **(3 sol)**, with nanoparticles and PH500 in a ratio monomer : Ni = 60 : 1 has been prepared. In this case, it has been possible to perform a spin coating over a thin

flexible glass, following the procedure described in Appendix A. After the spin coating process, the glass has been heated at 150° for 10 minutes. Film thickness is estimated to be about 60 nm. The obtained film is homogenous and light blue colored.

7.2.5.3 *Conductivity Measurements*

4 platinum wires (diameter of 0.25 μm) have been attached to the resulting film and the conductivity has been measured from room temperature down to 2 K. No hysteresis appears upon heating the sample from 2 K to r.t. as shown in Figure 7.10.
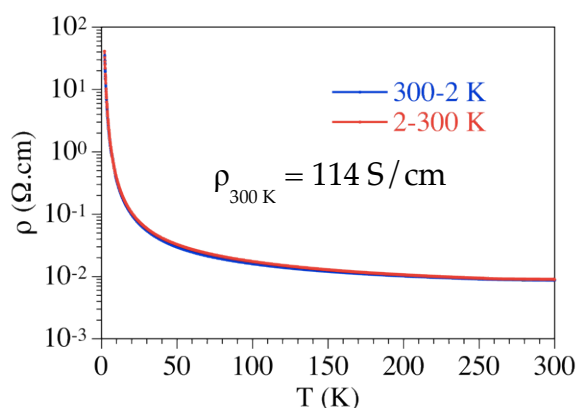
Figure 7.10: Temperature dependent plot of resistivity during the process of cooling (blue line) and warming (red line).

This film has a very high conductivity at room temperature (114 S/cm) and the resistivity increases when the temperature decreases, consistently to what expected for an activated behavior (Figure 7.10). Nevertheless, this is not the classical behavior of a semiconductor since the Arrhenius plot (Figure 7.11, left) is not linear. The conductivity can be well reproduced with the Variable Range Hopping model:

$$r = r_0{}^*exp[(T_0/T)^a]$$

with a = 1/2, which is the expected value for a 1D system; (a = 1/[d+1], being d the dimensionality of the system) (Figure 7.11, right). This behavior is typical of organic polymeric systems.
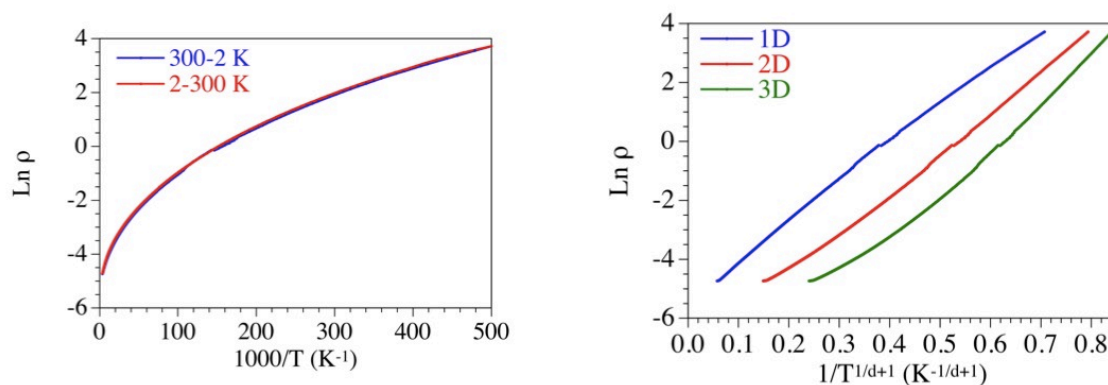
Figure 7.11: Arrhenius plot for the thin film obtained from **(4 sol)** solution (left); Lnρ depending of the system dimensionality (right).

The conductivity has also been measured on a 4 months aged sample. As reported in Figure 7.12 (left), the conductivity diminishes of about ten times with respect to the fresh sample.
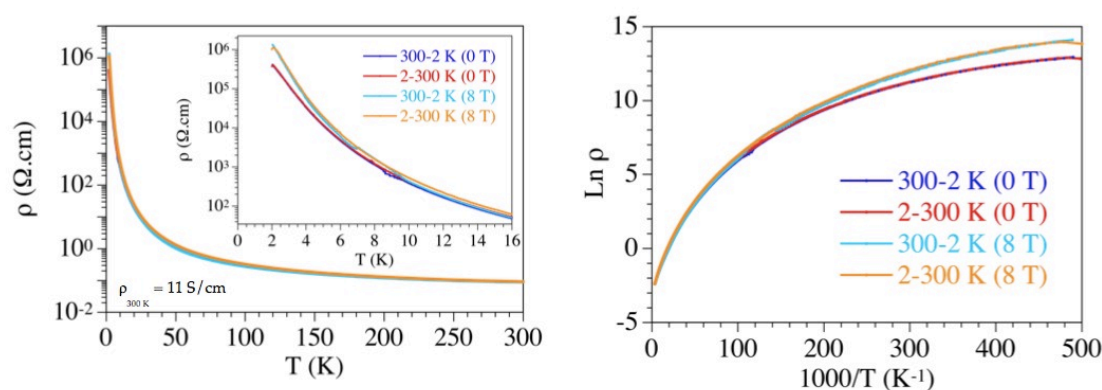
Figure 7.12: Resistivity (left) and Lnρ measurements (right) measured in the presence or absence of applied 8 T magnetic field.

Finally, magnetoresistance measurements have also been performed to study the possible interplay between conductivity and magnetism in this hybrid film. It is interesting to note that this temperature is very close to the blocking temperature displayed by the NP as shown by magnetic Ac measurements. This result suggests that there must be an interaction between both sublattices. A possible reason for this interaction may be the change in the orientation of the magnetic NP that try to align parallel to the magnetic field. The rotation of the NP may induce slight changes in the polymeric matrix that lead to changes in the resistivity of the polymer film.
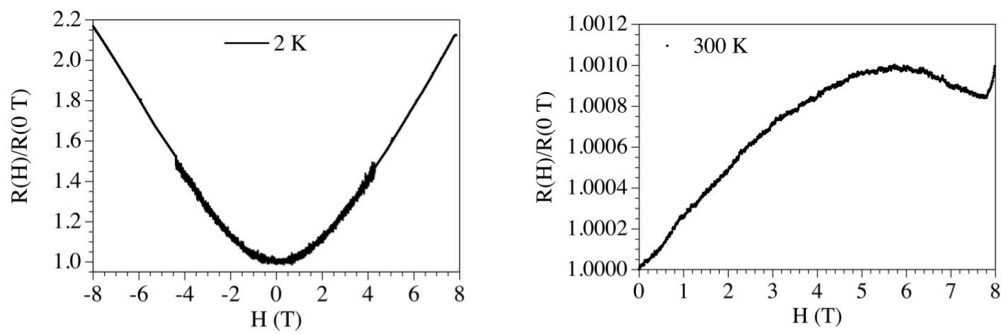
Figure 7.13: Resistance vs magnetic field at 2K (left) and at r.t. (right).

At low temperatures (2 K) the resistance at 8 T is more than twice the resistance at 0 T (Figure 7.13, left), indicating a significant magnetoresistance effect. Such a behavior is only observed at low temperatures (below ca. 8 K). At higher temperatures the resistance does not change with the magnetic field (Figure 7.13, right) as at 8 T the resistance is only ca. 0.1% higher than that at 0 T. By studying the influence of the magnetic field on the I - V curves it is possible to infer that the applied field only influences the low T behavior (Figure 7.14).
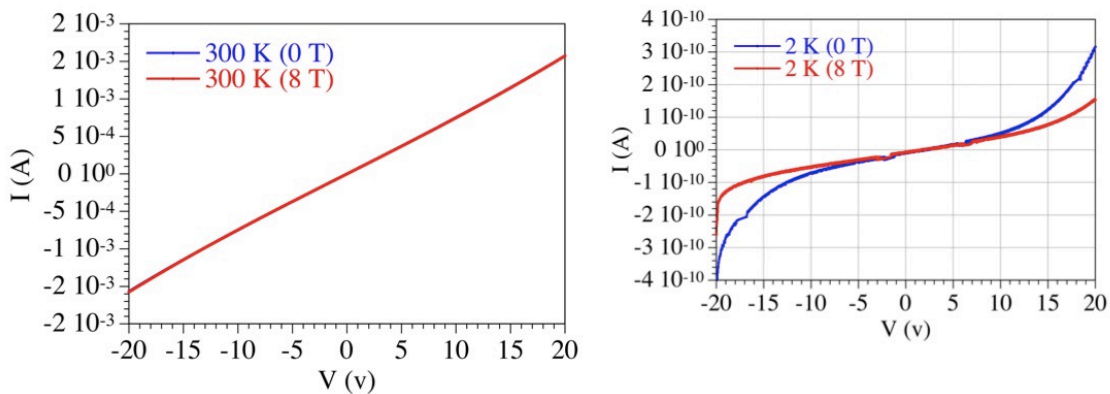
Figure 7.14: I-V plot at r.t. (left) and at 2 K (right).

On the other hand, at 300 K, a linear I-V behavior (Ohm's law) (Figure 7.14, left) is observed, while at 2K the I-V plot shows a deviation from the Ohm's law (Figure 7.14, right). This is due to the fact that the resistance is quite high at low temperatures and the sample is not an Ohmic conductor for high intensities anymore. This is quite common and indicate that the intensity overpasses the threshold intensity.

7.3 CONCLUSIONS

The combination of magnetic nanoparticles of Prussian Blue Analogues with PEDOT leads to an interesting nanocomposite in which the negatively charged particles are easily coated with the already oxidized PEDOT, PH500® to give a hybrid material that can be easily processed as a thin film.

This new material has a very high room temperature conductivity of about 114 S/cm and magnetic measurements show superparamagnetic properties. The magnetoresistance measurements reveal that there is an interplay between the magnetic and conducting lattices since the films show a change in the conductivity at temperatures below the blocking temperature of the NPs. The magnetoresistance measurements show that at 2 K the resistivity increases by a factor above 2 at 8 T. A lot of work is planned for better understanding this kind of hybrid material, in particular to correlate these properties with the morphology and conformation of the polymer. It is noteworthy that this material constitutes one of the first examples of inorganic magnetic nanoparticles embedded in a highly conducting organic polymer in which the magnetoresistance can be studied down to very low temperatures (in the usual case the high resistivity limits these measurements to relatively high temperatures).

7.4 EXPERIMENTAL SECTION

7.4.1 Synthesis

$K_3Fe(CN)_6$, CsCl and $NiCl_2 \cdot 6H_2O$ were purchased from Aldrich and used as received. PEDOT:PSS (1 : 2.5 by weight) was purchased from Heraeus with the trade name Clevios™ PH500.

7.4.1.1 *Synthesis of $Cs_{0.46}Ni[Fe(CN)_6]_{0.94}$ nanoparticles (1 sol)*

The $Cs_{0.46}Ni[Fe(CN)_6]_{0.94}$ nanoparticles were synthesized following a slight modification of the procedure reported in literature [1]: a fast addition under vigorous stirring of solutions of $NiCl_2 \cdot 6H_2O$ (1 mM) and CsCl (2 mM) to an aqueous solution of $K_3Fe(CN)_6$ (1 mM) leads to an orange-brown solution **(1**

sol), containing the corresponding nanoparticles, that remained stable for several days. **(1 sol)** exhibited the Tyndall effect when irradiated with a laser beam, thus confirming the presence of nanoparticles.

7.4.1.2 Synthesis of $Cs_{0.46}Ni[Fe(CN)_6]_{0.94}$ nanoparticles doped with PH500

0.170 mL of PH500® (water solution of 1. 1% PEDOT:PSS = 1 : 2.5) was added to 5 mL of **(1 sol)** solution, keeping the molar ratio PEDOT:Ni $\simeq$ 1:1. The obtained solution **(2 sol)** exhibited Tyndall effect when irradiated with a laser beam, thus confirming the presence of nanoparticles. A three times volume of acetone was then added to solution **(2)** and, after some minutes, a flocculate appeared **(8)**. The flocculate was centrifuged and washed with distilled water and acetone. The flocculate was dried under vacuum at r.t.

A second experiment was carried out following the above reported procedure by adding 2.74 mL of PH500® were to 1.0 mL of **(1 sol)** solution, keeping the molar ratio monomer : Ni $\simeq$ 60 : 1, **(4 sol)**.

7.4.2 Physical Measurements

Dynamic Light Scattering (DLS) were performed with a Malvern Zetasizer apparatus on 2 mL of **(1 sol)** and **(2 sol)** particle dispersion.

High Resolution - Transmission Electronic Microscopy (HR-TEM) experiments have been carried out using TECNAI G2 F20 (FEI) with 200kV field emission (FEG) and 0.18 nm resolution. Sample of **(1 sol)** was prepared by dropping a diluite solution (1:2) fresh prepared solution of the dispersed particles over a copper grid (Lacey Formvar/Carbon, 300 mesh, copper approx. grid hole size: 63 μm). Sample of **(2 sol)** was prepared by dropping a fresh prepared H_2O/Acetone (1:3) solution of the dispersed particles over a copper grid (Lacey Formvar/Carbon, 300 mesh, copper approx. grid hole size: 63 μm). Samples were tested when they were dried. The digital analysis of the HR-TEM micrographs was done using Digital Micrograph Software.

Electron diffraction pattern and spectroscopic technique as EDS and Mapping were performed using this apparatus.

Scanning electron microscopy (SEM) experiments have been carried out using Philips SEM-XL30 equipped with an EDAX microprobe, used for determing metallic atomic composition of samples.

The magnetic susceptibility measurements were carried out in the temperature range 2-300 K with an applied magnetic field of 0.1 T on a sample of compound **(8)** with a Quantum Design MPMS-XL-5 SQUID susceptometer. The isothermal magnetization was performed on the same sample at 2 K with magnetic fields up to 8 T. The susceptibility data were corrected for the sample holder previously measured using the same conditions.

Spin coating experiments were performed by using Chemat Technologies model KW-4A apparatus. Fresh prepared solution of **(4 sol)** was spin-coated (1000 rpm, 1 minute) onto thin flexible glass (prior to deposition, the glass substrates were extensively cleaned, using chemical and UV-ozone methods) and the layers were subsequently annealed at 150°C on a hotplate for 10 min, resulting in a layer thickness of approximately 60 nm. After spin-coating, the homogenous and with a light blue color films were dried and transferred into a dry box.

D.C. conductivity measurements over the range 2–300 K were performed using the four contacts method for spin-coated sample **(4 sol)**. Contacts between the film and platinum wires (25 mm diameter) were made using graphite paste. The samples were measured in a Quantum Design PPMS-9. The cooling and warming rate was 1 K min^{-1} and the results were, within experimental error, identical in the cooling and warming sweeps.

REFERENCES

[1] DeLongchamp, D. M.; Hammond, P. T. *Chem. Mater.* **2004**, *16*, 4799–4805

[2] DeLongchamp, D. M.; Hammond, P. T. *Adv. Funct. Mater.* **2004**, *14*, 224–232

[3] Clemente-Leo´n, M.; Coronado, E.; Lopez-Munoz, A.; Repetto, D.; Brinzei, D.; Catala, L.; Mallah, T. *Chem. Mater.* **2008**, *20*, 4642 – 4652

[4] L. Catala, F. Volatron, D. Brinzei, T. Mallah, *Inorganic Chemistry*, **2009**, Vol.48 (8) 3360-3370, and references therein

[5] Catala, L.; Gacoin, T.; Boilot, J. P.; Riviere, E.; Paulsen, C.; Lhotel, E.; Mallah, T. *AdV. Mater.* **2003**, *15*, 826–829

[6] T. Uemura, M. Ohba, S. Kitagawa, *Inorganic Chemistry*, **2004**, *43*, 7339-7345

[7] Volatron, F.; Catala, L.; Riviere, E.; Gloter, A.; Stephan, O.; Mallah, T. *Inorg. Chem.* **2008**, *47*, 6584–6586

[8] Kerbellec, N.; Catala, L.; Daiguebonne, C.; Gloter, A.; Stephan, O.; Bunzli, J. C.; Guillou, O.; Mallah, T. *New J. Chem.* **2008**, *32*, 584–587

[9] Catala, L.; Mathoniere, C.; Gloter, A.; Stephan, O.; Gacoin, T.; Boilot, J. P.; Mallah, T. *Chem. Commun.* **2005**, 746–748

[10] Brinzei, D.; Catala, L.; Mathoniere, C.; Wernsdorfer, W.; Gloter,A.; Stephan, O.; Mallah, T. *J. Am. Chem. Soc.* **2007**, *129*, 3778–3779

[12] G. Torres-Gómez, P. Gómez-Romero, *Synthetic Metals*, **1998**, (*98*), 95 – 102

[13] "PEDOT, Principles and Applications of an Intrinsically Conductive Polymer", A. Elschner, S. Kirchmeyer, W. Lövenich, U. Merker, K. Reuter, **2011**, CRC Press

CHAPTER 8

Conclusions and Perspectives

A well-thought-out design of the building blocks has led to the synthesis and full characterization of new multifunctional materials (MMMs) in which conductivity and magnetism coexist or, in some cases, interact.

- [(BDH-TTP)$_6$] [Fe(croc)$_3$] ·CH$_2$Cl$_2$ **(1)**, has been prepared and fully characterized, where paramagnetism is due to isolated Fe(III) metal ions with S = 5/2 ground state of the anionic [Fe(croc)$_3$]$^{3-}$ complexes, and conductivity originates from BDH-TTP organic donor in k-type packing. At ambient pressure, this compound behaves as a semiconductor, showing high conductivity (~ 10 S/cm) at room temperature. When applying a pressure higher than 7 kbar the metal – insulator (M – I) transition is suppressed, and the compound retains the metallic state down to low temperature (2 K). At ambient pressure, the isostructural [(BDH-TTP)$_6$] [Ga(croc)$_3$] ·CH$_2$Cl$_2$ **(2)** behaves as a metal down to ~ 100 K, although no M – I suppression occur even at pressure of 15 kbar.

- In [Mn(5-MeOsaltmen)(acetone)]$_2$[Ni(dmit)$_2$]$_6$ **(3)**, single molecule magnet (SMM) behavior of the Mn(III) dimers coexists with the semiconducting behavior due to the d^8 square planar complexes of [Ni(dmit)$_2$]$^{n-}$ (n = 0 or 1). From the IR spectrum, electrical resistivity, and energy band calculations, [Ni(dmit)$_2$]$^{n-}$ is in a charge-ordered state that, under pressure, should lead to a metallic or superconducting state, however this behavior has not been observed in **(3)**. In addition, deviations of the magnetic properties from that of isolated [Mn$_2$]$^{2+}$ SMMs based, have been found in this compound: the value of χT of **(3)** at 300 K (7.60 cm^3 · K · mol^{-1}) is higher than that of the isolated Mn dimer (~6.0 cm^3 · K · mol^{-1}). This behavior may be due to interactions such as [Ni(dmit)$_2$]$^{n-}$ ··· [Ni(dmit)$_2$]$^{n-}$, [Mn$_2$]$^{2+}$ ··· [Mn$_2$]$^{2+}$, [Ni(dmit)$_2$]$^{n-}$ ··· [Mn$_2$]$^{2+}$. This demonstrates that it is possible to tune the SMM behavior by changing the combination of SMMs and conducting molecules.

Processing of these materials has been performed by embedding different magnetic carriers into a conducting polymer, poly(3,4-ethylenedioxythiophene) (PEDOT). Following this strategy, new multifunctional materials showing magnetic and conducting (carried by the polymeric matrix) properties have been obtained as thin films from solution. Different preparation methods have been designed and used depending on the chemical nature of the magnetic carrier.

- By using potentiodynamic and potentiostatic methods, two different multifunctional materials based on electrochemical polymerized PEDOT doped with magnetic polyoxometalate (POM) $[Co_4(H_2O)_2(PW_9O_{34})_2]^{10-}$ have been synthesized. In particular, it is worth mentioning that the PEDOT/POM obtained by using the potentiodynamic method **(4)** is more stable than the analogous material obtained by applying a constant potential **(5)**, when subjected to potential cycles in acetonitrile solutions of $LiClO_4$ and $TBAClO_4$. Physical properties have been investigated for (5), since thin films of this material can be easily detached from electrode surface. In particular, conductivity of ~4 S/cm at room temperature has been measured and magnetic measurements reveal the presence of isolated POM anions into the film.

- Using the *in situ* chemical oxidation, two PEDOT films doped with $[Fe^{II}Cr^{III}(ox)_3]^-$ anion have been obtained. HR-TEM measurements reveal the presence of 2D nanocrystalline structures and magnetic measurements show ferromagnetic coupling due to Fe(II)-Cr(III) ions and a superparamagnetic behavior in these magnetic polymers. The film obtained with a EDOT : anion ratio of ca. 1:1 **(6)** shows a reversible transition to insulating state at ~250 K, due to a reversible localization process in the highly charged PEDOT polymer. A semiconducting behavior has been instead observed for a material obtained with a EDOT : anion ratio of ca. 10:1, **(7)**. **(7)** shows a conductivity of $2.9 \cdot 10^{-5}$ S/cm at r.t., lower than that measured for **(6)** (0.012 S/cm). These findings confirm that the electrical properties of these materials strictly depend on the EDOT : anion ratio.

- The oxidized PEDOT, PH500™ has been also used for coating negatively charged Prussian Blue Analogs, $Cs_{0.46}Ni[Fe(CN)_6]_{0.94}$ nanoparticles (NPs). Magnetic measurements for the obtained material **(8)**, show superparamagnetic properties due to the presence of NPs. **(8)** exhibits a very high r. t. conductivity of about 114 S/cm and behaves as a semiconductor. In the opposite way respect to similar systems, this highly conducting blend of PEDOT has allowed magneto- resistance measurements at low temperature. A change in conductivity at temperatures below the blocking temperature of the NPs (at 2 K the resistivity increases by a factor above 2 at 8 T), reveals the existence of an interplay between the magnetic and conducting lattices.

These promising results highlight the versatile opportunity to use the molecular approach for synthesizing new materials. Moreover, deeper investigations are looked-for with the aim for improving the conducting and magnetic properties of the obtained materials by changing the building blocks either in crystals or in polymers. New perspectives are introducing chiral substituents in both conducting and magnetic building blocks

Since conducting polymers offer a straightforward and low-cost method to process multifunctional materials, further investigations are required to study technological applications of the most promising thin films.

Although only conductivity and magnetism have been taken into account here, multifunctional materials offer interesting perspectives in combining other building blocks showing peculiar physical properties as non-linear optics, luminescence, …

ACKNOWLEDGMENTS

Firstly, I wish to thank my supervisor, Prof. Maria Laura Mercuri, for suggesting me this interesting research, for her precious guide and encouragement. I wish also to thank very much all my research group: Prof. Paola Deplano, Prof. Emanuele Trogu, Dr. Angela Serpe, Dr. Flavia Artizzu, Dr. Davide Espa, Matteo Atzori, Dr. Luca Pilia and Mariangela Cuscusa for their constant support and valuable advice.

I am grateful to Prof. Eugenio Coronado and Prof. Carlos Giménez-Saiz who gave me the opportunity to spend a research stay in their lab at the Institute for Molecular Science, in Valencia. I would like to thank all the people from the ICMol lab.

I wish also to acknowledge Prof. Masahiro Yamashita and Dr. Kazuya Kubo for their supervision on my research stay at the Tohoku University, Sendai, Japan.
A grateful acknowledgement is addressed to all the people from the lab of the 8th floor.

Thanks are also due to Prof. Ito, from the Nagoya University, who performed the physical characterization of the $[(BDH-TTP)_6]$ $[M^{III}(croc)_3]$ · CH_2Cl_2 compounds and to Dr. Gonzalo Abellán, ICMol, Valencia, for HR-TEM analyses.

Finally, my acknowledgements go to all my colleagues, my family, my friends and to .

APPENDIX A

Experimental methods

A.1 ELECTROCHEMICAL METHOD

A.1.1 Cyclic Voltammetry and Chronocoulometry

Polymer films were grown in a small-scale (volume: 15 mL), three-electrode single compartment electrochemical cell. Each electrode was spaced by a Teflon cap. The working electrode (WE) was a platinum disk with 0.2 cm² geometric area. The WE surface was polished with 1.0, 0.3 and 0.05 μm alumina and washed with distilled water and ethanol before each experiment. The counter electrode was a platinum wire. The reference electrode (RE) was comprised of an Ag wire immersed in a solution of $AgNO_3$ (0.01 M) and $TBAClO_4$ (0.1 M) in acetonitrile (ACN). The Ag/Ag^+ RE was calibrated against ferrocene/ferrocenium redox couple (1mM) in the same solvent/electrolyte system. At scan rate between 20 and 200 mV/s, ferrocene presented $E_{1/2}$ = +0.087 V(+0.080 experimental) vs. Ag/Ag^+, with a peak separation, ΔE_p (anodic to cathodic) of 71 mV(65 experimental). Measurements were made at room temperature (ca. 25°C), within the potential window +2500 to -2000 mV using cyclic voltammetry (CV) method and 1.0 V constant potential during the chronocoulometry (Coul) method. The solutions were degassed with pure nitrogen for 5 minutes before use and blanketed with nitrogen gas during the voltammetric scans.
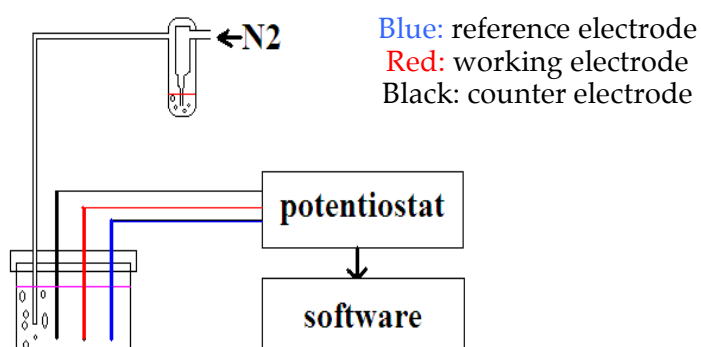

Blue: reference electrode
Red: working electrode
Black: counter electrode

Figure A.1: A schematic diagram of three-electrode single compartment electrochemical cell.

A.1.2 *in situ* spectroelectrochemistry

The WE was an indium-tin oxide (ITO) coated glass; the CE was a platinum foil and the RE was the one described previously in the A.1.1 Section. The three-electrode system was inserted in the cell and the solution was degassed with pure nitrogen for 5 minutes. The experiments were performed at room temperature.
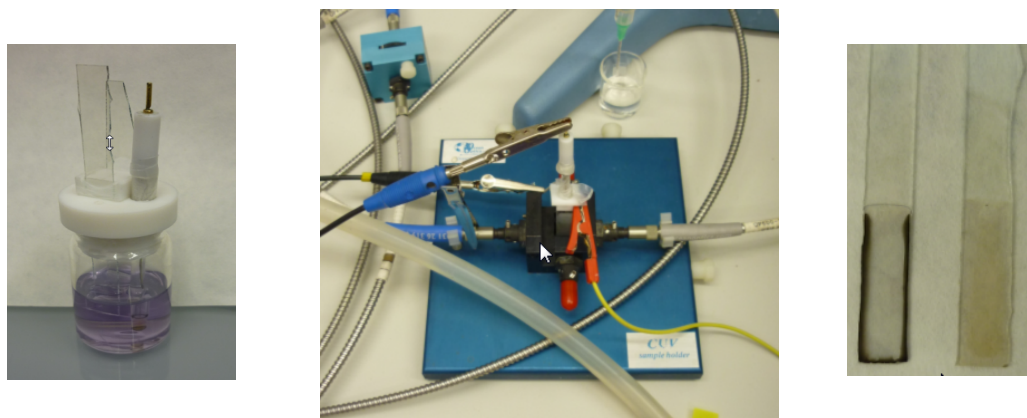

Figure A.2: A three-electrode single compartment electrochemical cell with a ITO Working Electrode (right); the real apparatus used for recording UV-Vis spectra in-situ (middle); the ITO WE and CE after electropolymerisation (left).

A.1.3 EQCM

In Electrochemical Quartz Crystal Microbalance (EQCM) experiments, a minute change in oscillation frequency of the quartz crystal, ionic or molecular transport across the interface between the polymer and an electrolyte solution can be sensitively monitored. [1]
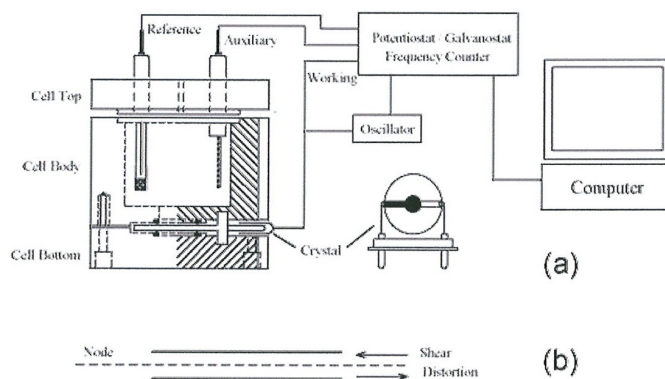

Figure A.3: A schematic diagram of EQCM experimental apparatus.

A.2

In many cases, interfacial mass changes are related in a simple manner to changes in the EQCM oscillation frequency, through the Sauerbrey Equation:

$$\Delta f = \frac{-2\Delta m\, n\, f_0^2}{A\sqrt{\mu_q \rho_q}}$$

where:

Δf :   changes in frequency;

Δm :   changes in mass per unit area;

n :   number of electrons which are exchange during the redox reaction;

f_0 :   the resonant frequency of the fundamental mode of the crystal;

A :   electrode surface area;

μ_q :   shears modulus of quartz;

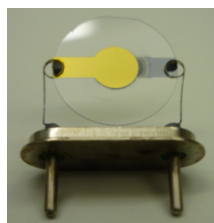ρ_q :   density of quartz;

Figure A.4: Gold electrode used for EQCM measurements.

The cell contains a crystal electrode in which one side of the crystal faces the solution and the other faces the air. The resonant frequency of the fundamental mode of our crystal is 7.995 Hz. The diameter of the quartz crystal is 13.5 mm and that of the gold electrode is 5.1 mm. A wire of platinum was used as counter electrode and Ag/Ag^+ in acetonitrile, $TBAClO_4$ 0.1 M, $AgNO_3$ 0.01 M electrode was used as reference.

A.2 ELECTROCRYSTALLIZATION

Electrocrystallization is a technological, powerful method to synthesize high quality crystals, suitable for x-rays diffraction and other physical measurements. In molecular material science, this technique is particularly useful because, since multifunctional molecular materials (MMMs) are generally insoluble, it is not always easy to obtain high quality crystal by conventional methods of recrystallization from organic solvents. With this

technique, a controlled oxidation of organic donor molecules leads to a radical cation formation. The involved driving forces are listed below:

* electrochemical properties of the counterion;
* temperature;
* concentration and purity degree of reagents;
* purity degree of the solvents;
* current density and electrical potential.

It is necessary to check carefully these parameters:

1. the electrocrystallization should be performed in a no-vibrations and constant temperature room;
2. glasses and electrodes should be carefully cleaned;
3. reagents and solvents should be anhydrous and HPLC grade;
4. the experiment should be performed under inert atmosphere.

Electrocrystallization takes place in a "H" glass cell, as shown in Figure A.4. The glass cell is constituted of two compartments, divided by a porous glassy membrane. The cell is cleaned following the procedure described in literature. [2]

Both the organic donor and its counterion are put in the anodic compartement while only the counterion is inserted in the cathodic compartement. Both compartements are half filled with pure or mixed solvent solutions are degased for about 30 minutes with a continuous argon flux. The two platinum wires, inserted in the two compartments, are connected to a potentiostat: the generated current density causes the oxidation of the donor molecule and crystals start to grow on the electrode surface. Generally, the material is a conductor and acting as electrode itself and favouring crystal growth.
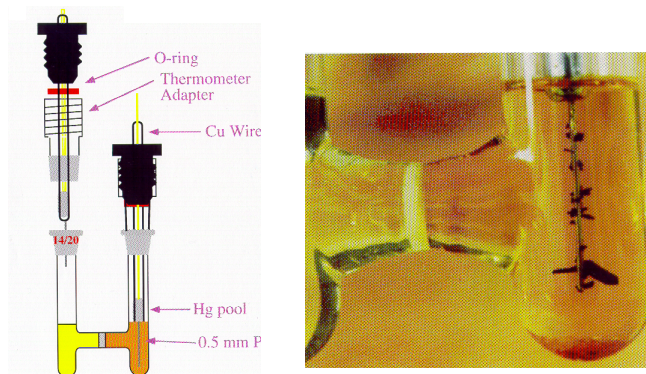

Figure A.4: scheme of an electrocrystallization cell (left); some crystals grown on the platinum electrode (right).

A.3 SPIN COATING

The spin coating process permits to obtain a uniform thin film from a homogeneous solution. Spin coating is performed over a perfectly clean surface as, for example, a glass or a Mylar sheet. During the spin coater rotation, the support is being held by a vacuum chuck. Films of different thickness can be obtained depending on spinning parameters (number of rotations per second, spin coating period) and on the chemical nature of the starting solution (percent solids, drying rate, viscosity, surface tension and so on). In Fig. Y. 5, a spin coating scheme is shown. step 4) is a heating treatment for complete solvent removal.
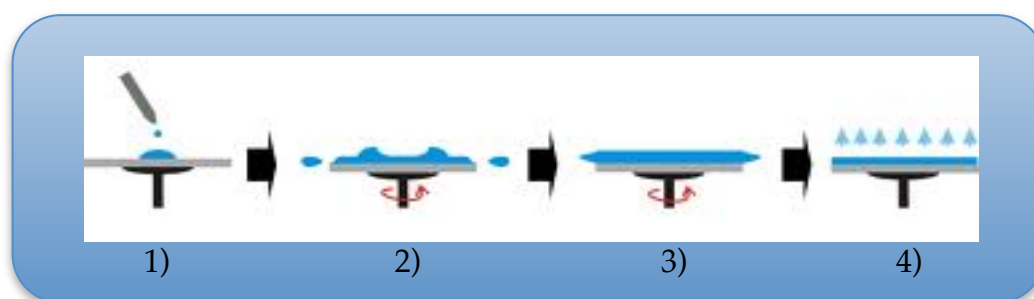
Fig. Y.5: Spin coating process scheme: 1) the solution is deposited onto the support surface; 2) the rotation starts with different speed and the excess liquid flies off; 3) because of the centripetal force, the starting solution spreads to the edge of the substrate, leaving a thin liquid layer; 4) the heating process guarantees complete solvent evaporation.

All experiments were performed in a clean room.

Figure A.6: thin glass support (left) and the spin coater (right) used in this work.

REFERENCES

[1] W. Paik, I.-H. Yeo, H. Suh, Y. Kim, E. Song, *Electrochim. Acta*, **2000**, *45*, 3833.

[2] T. J. Emge, H. H. Wang, M. A. Beno, J. M. Williams, M.-H. Whangbo, M. Evain, *J. Am. Chem. Soc.* **1986**, *108*, 8215-8223
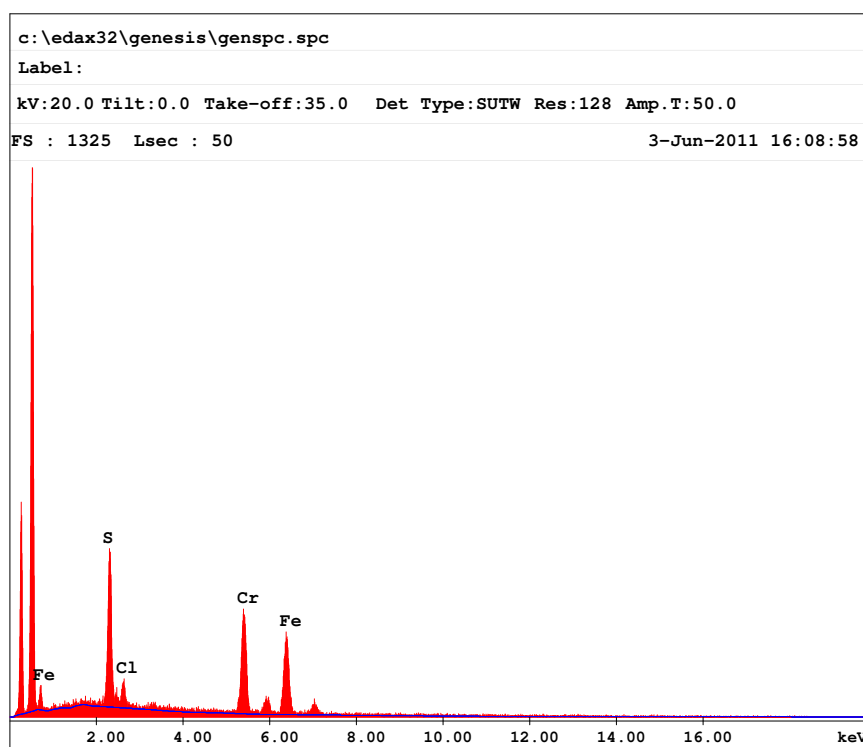
APPENDIX B
Experimental data

B.1 EDX ANALYSES

B.1.1 EDX analysis performed for (6)

```
c:\edax32\genesis\genspc.spc

Label:

kV:20.0 Tilt:0.0 Take-off:35.0   Det Type:SUTW Res:128 Amp.T:50.0

FS : 1325  Lsec : 50                          3-Jun-2011 16:08:58
```



```
EDAX ZAF Quantification (Standardless)
Element Normalized
SEC Table : Default

Element   Wt %    At %   K-Ratio    Z       A       F
  S K    22.95   32.75   0.1903   1.0878  0.7569  1.0070
  ClK     4.40    5.68   0.0320   1.0381  0.6954  1.0071
  CrK    33.35   29.36   0.3325   0.9688  0.9704  1.0604
  FeK    39.30   32.21   0.3556   0.9702  0.9327  1.0000
  Total 100.00  100.00

Element  Net Inte.    Bkgd Inte.    Inte. Error     P/B
  S K    107.64        8.64          1.47          12.46
  ClK     17.76        7.92          4.62           2.24
  CrK     95.86        3.92          1.50          24.45
  FeK     76.92        3.36          1.68          22.89
```

B.1.2 EDX analysis performed for (7)

```
c:\edax32\genesis\genspc.spc

Label:

kV:20.0 Tilt:0.0 Take-off:35.0   Det Type:SUTW Res:128 Amp.T:50.0

FS : 1204  Lsec : 50                            30-Jun-2011 18:42:27
```



```
EDAX ZAF Quantification (Standardless)
Element Normalized
SEC Table : Default

Element    Wt %    At %   K-Ratio    Z        A        F
  S K     70.79   80.29   0.6535   1.0320   0.8926   1.0021
  CrK     14.35   10.04   0.1266   0.9213   0.9368   1.0220
  FeK     14.85    9.67   0.1293   0.9217   0.9443   1.0000
 Total   100.00  100.00

Element   Net Inte.    Bkgd Inte.   Inte. Error     P/B
  S K     338.50         6.38         0.78        53.06
  CrK      33.42         3.46         2.69         9.66
  FeK      25.60         2.70         3.08         9.48
```
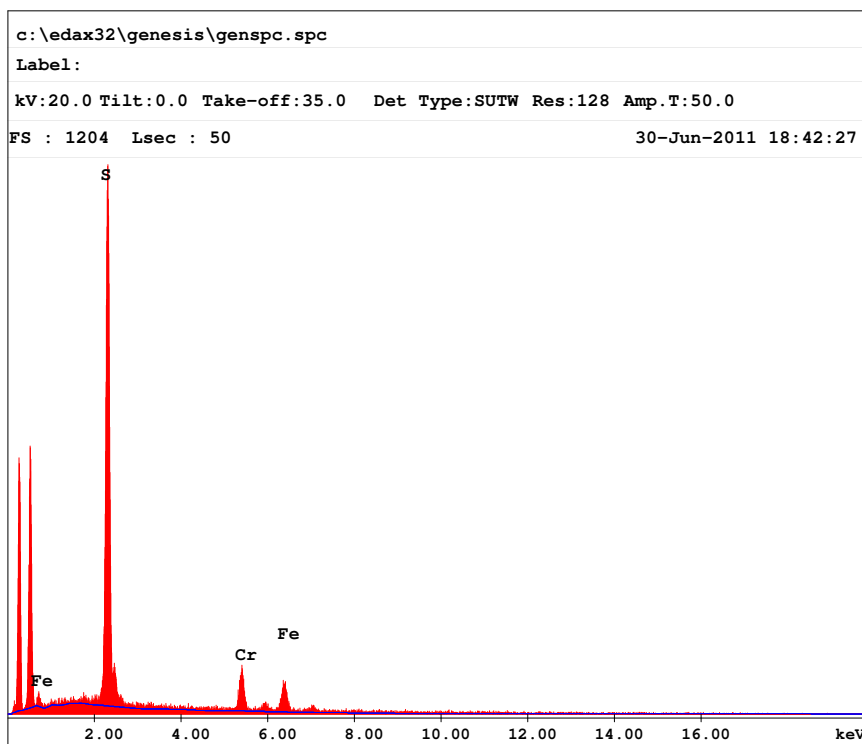
B.2 DLS ANALYSES

B.2.1 DLS FOR (1 SOL)

			Size (d.nm):	% Volume	Width (d.nm):

File Name: Elisa todas.dts
Record Number: 20
Material RI: 1.56
Material Absorbtion: 0.10

Dispersant Name: Water
Dispersant RI: 1.330
Viscosity (cP): 0.8872
Measurement Date and Time: venerdì 17 giugno 2011 11.08.35

Temperature (°C): 25.0
Count Rate (kcps): 304.6
Cell Description: Glass cuvette with round aperture

Duration Used (s): 60
Measurement Position (mm): 4.65
Attenuator: 11

			Size (d.nm):	% Volume	Width (d.nm):
Z-Average (d.nm): 99.71		Peak 1:	7.771	99.4	2.972
PdI: 0.170		Peak 2:	4920	0.6	894.0
Intercept: 0.338		Peak 3:	301.2	0.0	112.5

Result quality : Refer to quality report
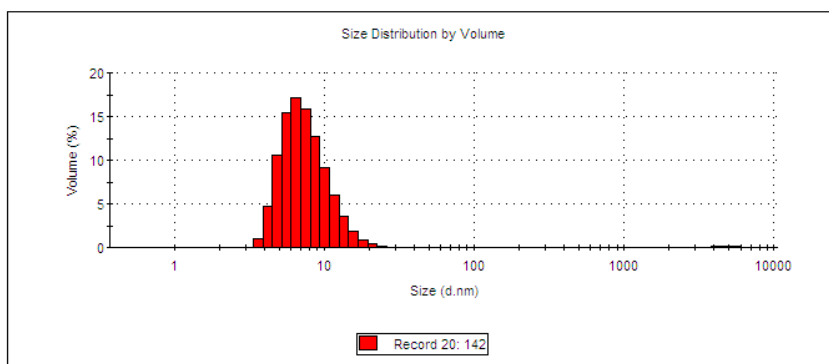
B.2.2 DLS FOR 3 DAYS AGING (1 SOL)

File Name: Elisa todas.dts
Record Number: 30
Material RI: 1.56
Material Absorbtion: 0.10

Dispersant Name: Water
Dispersant RI: 1.330
Viscosity (cP): 0.8872
Measurement Date and Time: lunedì 20 giugno 2011 12.41.38

Temperature (°C): 25.0
Count Rate (kcps): 159.9
Cell Description: Disposable sizing cuvette

Duration Used (s): 80
Measurement Position (mm): 4.65
Attenuator: 11

			Size (d.nm):	% Volume	Width (d.nm):
Z-Average (d.nm): 260.0		Peak 1:	7.853	100.0	2.378
PdI: 0.315		Peak 2:	114.4	0.0	25.14
Intercept: 0.817		Peak 3:	0.000	0.0	0.000

Result quality : Refer to quality report

B.2.3 DLS FOR (2 SOL)

			Size (d.nm):	% Volume	Width (d.nm):
File Name:	Elisa todas.dts				
Record Number:	24				
Material RI:	1.56				
Material Absorbtion:	0.10				

Dispersant Name: Water
Dispersant RI: 1.330
Viscosity (cP): 0.8872
Measurement Date and Time: venerdì 17 giugno 2011 12.18.41

Temperature (°C): 25.0
Count Rate (kcps): 74.8
Cell Description: Disposable sizing cuvette

Duration Used (s): 100
Measurement Position (mm): 4.65
Attenuator: 11

			Size (d.nm):	% Volume	Width (d.nm):
Z-Average (d.nm): 75.30		Peak 1:	5.490	99.5	2.539
PdI: 1.000		Peak 2:	64.39	0.1	23.26
Intercept: 0.778		Peak 3:	620.7	0.2	268.4

Result quality : Refer to quality report
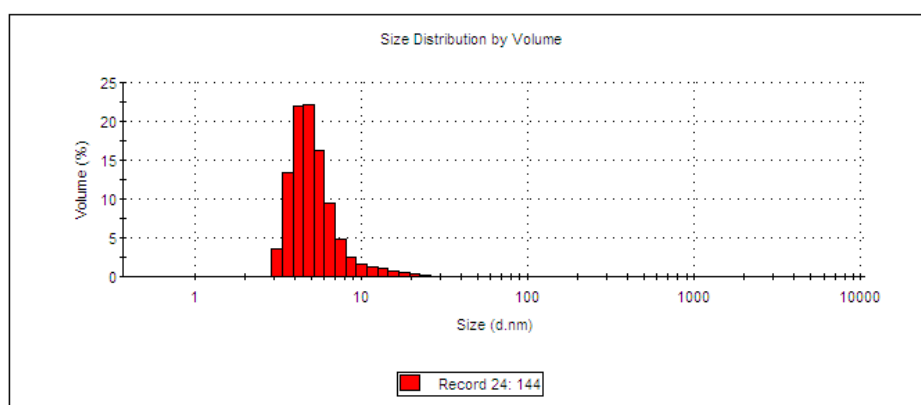
B.2.4 DLS FOR 3 DAYS AGING (2 SOL)

File Name: Elisa todas.dts
Record Number: 37
Material RI: 1.56
Material Absorbtion: 0.10

Dispersant Name: Water
Dispersant RI: 1.330
Viscosity (cP): 0.8872
Measurement Date and Time: lunedì 20 giugno 2011 13.11.53

Temperature (°C): 25.0
Count Rate (kcps): 87.3
Cell Description: Disposable sizing cuvette

Duration Used (s): 100
Measurement Position (mm): 4.65
Attenuator: 11

			Size (d.nm):	% Volume	Width (d.nm):
Z-Average (d.nm): 64.69		Peak 1:	7.451	99.1	3.701
PdI: 0.858		Peak 2:	574.3	0.3	281.2
Intercept: 0.761		Peak 3:	4982	0.6	865.5

Result quality : Refer to quality report